九州大学学術情報リポジトリ
Kyushu University Institutional Repository

Study of (p, 2p) Reactions as a Practical Probe for Nuclear Spectroscopy

吉田, 英智

https://hdl.handle.net/2324/460395

出版情報：Kyushu University, 2009, 博士（理学）, 論文博士
バージョン：
権利関係：

Study of $(p, 2p)$ Reactions as a Practical Probe for Nuclear Spectroscopy

Hidetomo P. Yoshida

Doctoral Dissertation

January 25, 2010

Abstract

The $(p, 2p)$ reaction, a quasi-free nucleon knockout reaction, provides one of the most direct means to investigate single particle properties of bound nucleons. The purpose of this study is to realize sophisticated $(p, 2p)$ measurements by using high quality polarized proton beams and high resolution spectrometers and evaluate obtained experimental results from a view point as a spectroscopic tool.

In order to realize these $(p, 2p)$ measurements with 2-arm spectrometer system at Research Center for Nuclear Physics (RCNP), Osaka University, a trigger system by using Field Programmable Gate Array (FPGA) chips was newly developed in this study and the previous system based on standard NIM/CAMAC modules was replaced by this new system. The functional gates inside the FPGA chip can be programmed by computer softwares and one FPGA chip works as tens of NIM modules. One of the pioneer work in this study is that the chip is used for a real-time triggering logic while it is usually synchronized with fixed interval clock signals. This new trigger system dose not need hardware re-wiring to change the trigger logic. Instead, only re-downloading of a suitable file is required. Therefore, this system is used not only for $(p, 2p)$ experiments with two magnetic spectrometers but also for many other experiments including those using additional detectors combined with these spectrometers. This development greatly reduced troubles arising from reconstruction of trigger logics. Now, this trigger system is used as a general-purpose trigger system for all of experiments using the magnetic spectrometers at RCNP.

By using this trigger system, differential cross sections and analyzing powers (A_y) for ^{40}Ca$(p, 2p)$, ^{12}C$(p, 2p)$ and ^{6}Li$(p, 2p)$ reactions have been measured at an incident energy of 392 MeV for four kinds of systematical kinematic conditions. In addition, for ^{6}Li target, a precise experiment with high resolution in recoil momentum was performed.

The experimental results for various kinematic series were compared with distorted-wave impulse approximation (DWIA) calculations. For ^{40}Ca and ^{12}C targets, the calculations well reproduce the data for the recoil-momentum distributions of the differential cross sections and A_y's. For the ^{12}C target, meaningful difference between $1p_{3/2}$ and $1p_{1/2}$ knockout, namely j-dependence, was observed in A_y, which is useful for determination of the total angular momentum J. Spectroscopic factors (S-factors) were deduced from

comparison of DWIA calculations and experimental results for low lying $1d_{3/2}$ and $2s_{1/2}$ proton knocked-out states from ^{40}Ca, and $1p_{3/2}$ and $1p_{1/2}$ knocked-out states from ^{12}C. Because our experimental results are obtained for various and systematical kinematic conditions, the ambiguities in deducing the S-factors were estimated quantitatively and fitting errors were determined to be $\pm 15\%$. However, the absolute values of S-factors largely depend on the calculation models used in the DWIA calculations. Typical S-factors obtained were $30-40\%$ smaller than those from $(e, e'p)$ reactions. In addition, the S-factors obtained in this study and those from previous $(p, 2p)$ studies show a systematic incident-energy dependence. This suggests that further theoretical progress of in theoretical calculation is desired in order to deduced the S-factor, quantitatively.

For the ^{6}Li target, the differential cross section and A_y of the reaction leading to the higher excited state of residual ^{5}He are reproduced by a DWIA calculation assuming $1s_{1/2}$ knockout, but those leading to the lower excited state give completely different shapes from theoretical predictions assuming a simple $1p_{1/2}$ knockout and rather similar as those for s-state knockout, namely cross section show as a peak at around zero recoil momentum $\boldsymbol{k}_3$. Then, an additional experiment for this target using narrower angle-defining slits were performed and data of this precise experiment were analyzed in detail by using software subdividing of opening angles and momentum bites of spectrometers aiming to achieve high resolution in recoil momentum. Then, a recoil-momentum distribution of the cross section gated by a narrow region of separation energy shows a dip at $\boldsymbol{k}_3 \simeq 0$ MeV/c. In this plot, the ratio of the peak cross section, at $\pm$ 45 MeV/c, to the dip cross section was about 3:2. These features are quite similar as a result of ^{6}Li$(e, e'p)^5$He reaction, which is reproduced by calculations assuming a cluster structure in target nucleus.

From the result of this study, it is concluded that $(p, 2p)$ reactions are useful for investigation of the single particle properties of target nuclei as $(e, e'p)$ reactions, though a further theoretical development or some calibration is required for quantitative extraction of the absolute value of the strength. In addition, existence of clear j-dependence in A_y for the $(p, 2p)$ reactions is a unique advantage over the $(e, e'p)$ reactions. These results are valuable, for example, in unstable nuclear structure studies, where the knockout reactions in inverse kinematics is thought to be a powerful tool.

Contents

Chapter 1

Introduction

1.1 Investigation by Using Quasi-free Scattering

Quasi-free nucleon knockout scattering gives one of most direct means for investigation of the single particle properties of bound nucleons, such as the separation energy, momentum distribution, angular momentum and spectroscopic factor (S-factor). For many years, both of proton and electron beams have been used for these studies.

Exclusive measurement of quasi-free scattering are first studied using proton beam, namely as $(p, 2p)$ reactions. In early days, $(p, 2p)$ results which indicate evidences of quasi-free process were reported by Chamberlain and Segrè [1] and Cladis, Hess and Moyer [2] at Berkeley in 1952 and this indication was verified by Wilcox and Moyer [3]. By later experiments, such as one performed by Tyrén et al. [4], summed energies of two outgoing protons were measured and the energy spectrum supported the shell structure of the single-particle separation energies. and these results were found to agree well with the shell model and it is realized that the quasi-free nucleon knockout reaction is promising for investigation of inner shell structure [5]. In 1960s and 1970s, momentum distributions of differential cross section for many stable nuclei were systematically measured using proton beams at intermediate energies (150–1000 MeV) [6, 7, 8, 9, 10, 11]. The separation energy resolutions of those experiments were not enough to separate low lying discrete states clearly but even the cross section including a few states showed features characterized by

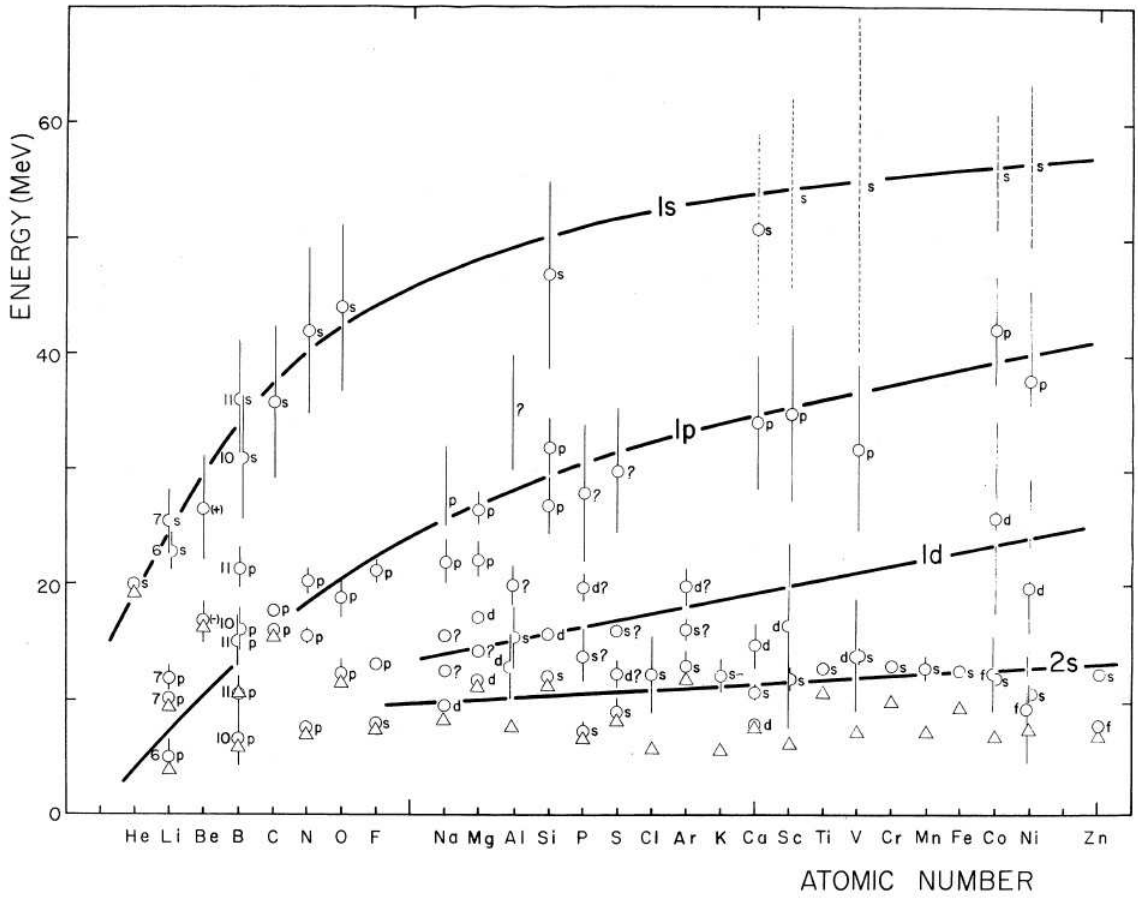

Figure 1.1: Separation energy and orbital angular momentum assignments of hole states obtained from quasi-free scatterings as functions of atomic number This figure is taken from Ref.[11].

corresponding orbital angular momenta in recoil momentum distributions. From those momentum distributions, the binding energies and the widths of hole states including deeply bound 1s states were successfully derived until about atomic number 60 of many stable nuclei. Jacob and Maris compiled these results [11, 12] as shown in Fig. 1.1. This systematic works indicated that the quasi-free scattering is very useful to investigations of nuclear structure.

1.2 Quasi-free Reactions as a Spectroscopy Tool

For studies by using $(e, e'p)$ reactions, early systematical investigations of single-particle properties of nuclei were performed at Tokyo and Saclay in the 1970s [13]. After the appearance of high duty-cycle facilities, such as NIKHEF-K and Maintz, the lepton probe for nucleon knockout reaction has been used for spectroscopic tools, intensively. At NIKHEF-K, by using the high resolution 2-arm spectrometer system, the high duty-factor beam extracted from the pulse stretcher ring has allowed precise single-nucleon knockout measurements with high resolution in separation energy, about 100keV. The precise momentum distributions of the differential cross sections for many kinds of targets have been measured systematically [14] and many results in nuclear spectroscopy have been deduced. The radii of states were derived from the momentum distributions of cross sections themselves by comparing with calculations. By normalizing calculation results to cross sections, the spectroscopic factors (S-factor) have been obtained. It was a great achievement for nuclear structure study to obtain S-factors systematically for major states of stable nuclei for mass numbers from 12 to 208. Dieperink and de Witt Huberts, and Kelly reviewed the results of high-resolution $(e, e'p)$ measurements on S-factors and momentum distributions [14, 15, 16].

On the other hands, by using $(p, 2p)$ reactions S-factors for low lying states of several nuclei have been tried to be derived since late 1970s. Experiments for example on ^{12}C [17, 18] , ^{16}O [19, 20, 21, 22] , ^{40}Ca [21, 23, 24, 25] and ^{208}Pb [26, 27] target nuclei had been performed at intermediate energies. The experimental groups themselves and other theoretical groups extracted S-factors from comparisons with distorted-wave impulse approximation (DWIA) calculations. But for many states of them, deduced S-factors were different from other groups deduced for the same state, or even quite different values were deduced depending on kinematical conditions even in a single experiments. For example, the S-factor values for $1p_{3/2}$ knockout from ^{12}C were different by factor two between the results given by the data symmetry- and asymmetry-angle kinematics, namely 2.0 and 1.0, respectively [17]. For $1d_{3/2}$ knockout from ^{40}Ca at E_p=200MeV [24], many

groups calculated using various effective NN-interactions [28], considering various effects for non-relativistic DWIA [29] or with finite-range and relativistic DWIA model [30]. The S-factor results depend on the theoretical calculation models, but, in many cases, much more differences, about 1.5∼2 times differences, are given when they use different angular set data. In addition, there are only a few experiments where the states are clearly separated each other in separation energy E_{sep} spectra, because their energy resolution ΔE_{sep} are mostly not better than a few MeV except a recent experiment by Neveling *et al.* [27]. In the work by Neveling *et al.*, ^{208}Pb($\vec{p}$,2p)^{207}Tl is experimentally studied at an incident energy of 200MeV [27] with the energy spectra resolution of 310keV, but because of narrow separation of residual states, their peak separation is only partially. In general, S-factors have not been deduced reliably or quantitatively in $(p, 2p)$ studies.

In the case of proton probe, another information quite valuable for nuclear structure studies can be obtained from spin observables. It was suggested by G.Jacob and Th.A.Maris *et al.* [31] that the analyzing power (A_y) for $(p, 2p)$ reaction shows a j-dependence, a difference between total angular momenta $J_>$ and $J_<$ of the bound proton orbits. This effect is caused by a combination of the spin-orbit coupling of bound proton, a spin-spin correlation in the nucleon-nucleon scattering and distortion effects in nuclear medium as shown in Fig. 1.2. Using a polarized proton beam, this effect was experimentally confirmed at TRIUMF by Kitching and coauthors [32]. After that, their group measured A_y for ^{16}O and ^{40}Ca targets at E_p=200MeV [19, 24, 33] and later for ^{16}O at E_p=500MeV [20]. The over all result is somewhat confusing. Some of A_y data for some experimental setting, mostly displayed in so-called shared-energy distributions, show clear j-dependence and reproduced well by DWIA calculations, but in some other cases calculations fail to predict neither experimentally observed differences of A_y for $J_>$ and $J_<$ knockout nor the A_y values themselves. Some theoretical groups modified the DWIA calculation by including some effects, such an off-shell effect, but these discrepancies was not resolved [34]. Further studies based on clear experimental data with unambiguous peak separation is desired.

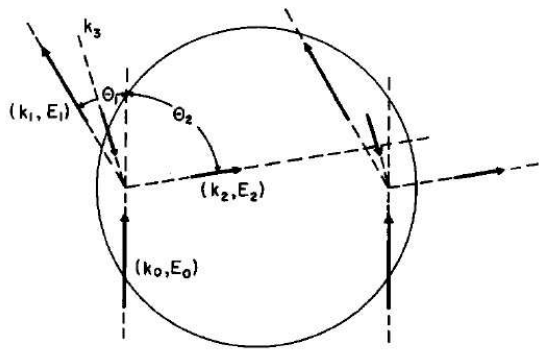

Figure 1.2: Th schematic representation of Maris effect(effective polarization): Observables depend on spin-orbit couplings and length of distortion. This figure is taken from Ref.[31].

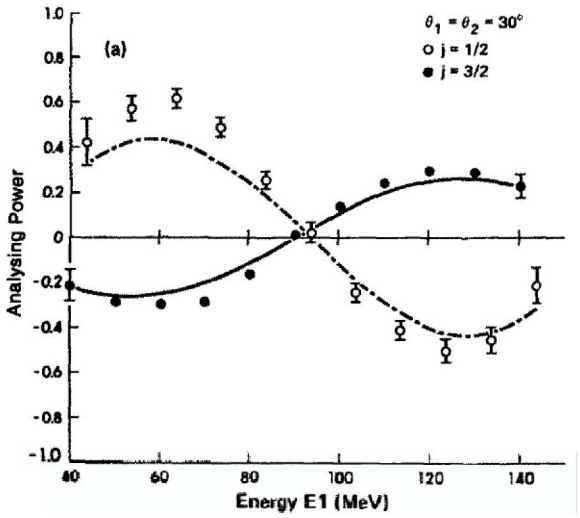

Figure 1.3: The experimental result shown Maris effect(effective polarization): The distribution of $1p_{3/2}$- and $1p_{1/2}$-knockout states from ^{16}O. This figure is taken from Ref.[33].

1.3 Aim of this Study

At the Research Center for Nuclear Physics (RCNP), Osaka University, our group has started a $(p, 2p)$ program. Advantages of RCNP are that high intensity and high quality polarized proton beams are provided and two magnetic spectrometers can be utilized in coincidence mode. Therefore, at RCNP is suitable to performed precise $(p, 2p)$ measurement with low background and high resolution [35, 36].

Even though these good conditions are satisfied at RCNP, systematic study of $(p, 2p)$ reactions for a spectroscopic purpose still requires significant efforts in experimental techniques. One of the most important factors is to construct a trigger system which handles complex detector system for two spectrometers, realizes very complicated trigger logics and controls a data acquisition system which transfers many potentially, more than two thousands, signals. In particular, for practical use in nuclear spectroscopy, it is important to realize repeatability of electronic circuits. Before this work, the time of construction for trigger circuits based on standard NIM/CAMAC modules with fixed functions was over one week, including checking and error corrections time. Then, a new trigger system

was build in this study based on flexible IC chips, which are programmed by computer software. This development greatly increased the reproducibility and reliability of the trigger logic when it is reconstructed.

The purpose of this study is to realize systematic experimental studies of $(p, 2p)$ reactions at RCNP and to examine the reliability of this reactions as a spectroscopic tool. In order to achieve this goal, we first constructed the trigger system mentioned above. Next, we actually performed experiments of $(p, 2p)$ measurements using ^{40}Ca, ^{12}C and ^{6}Li targets. In order to examine the validity of the DWIA calculations in this reaction, measurements were performed in various kinematic conditions, systematically. Then, the experimental results are compared with DWIA calculations and momentum distributions, j-dependence and S-factors are examined.

In the next Chapter, the development of trigger system is described in detail. In Chapter 3, the experimental details including kinematic conditions are presented. In Chapter 4, the analysis was explained and experimental results are shown. In Chapter 5, the result are compared with the DWIA calculation. In Chapter 6, additional precise experiment with ^{6}Li target are shown and its result is described. Finally, summary and conclusion are given in Chapter 7.

Chapter 2

Development of FPGA Trigger System

2.1 Trigger System for Spectrometer Experiments

Recently, trigger logic for experiments in nuclear physics is being complicated because sophisticated detectors or many detectors are used even if relatively simple experiments. Even if one magnetic spectrometer is used, two type of detectors, many channel wire drift chambers for detection for particle tracking and plastic scintillators for particle identification and triggering are usually used simultaneously. When standard NIM or CAMAC modules are used, the number of the modules must be increased according to increase of number of detectors and increase of complexity the trigger logic. Then, the construction of trigger circuits requires long time because of not only hard wiring for many modules but also the necessity to test the complicated circuits. In addition, electric modules are expensive. It may be a solution to prepare a dedicated trigger circuits and simple connections between the trigger circuit and detectors are changed before each experiment, but it is not cost effective.

At the Research Center for Nuclear Physics (RCNP), Osaka University, which is a national nuclear physics laboratory with the Ring cyclotron and the AVF cyclotron, many measurements for studying nuclear physics is performed in packed beam schedule. At the west experimental hall of RCNP, two magnetic spectrometers were installed and

many people use these machines either in separate mode or in combination with other detectors (such as Si detectors or NaI and liquid scintillation detectors). In the case of $(p, 2p)$ measurements, which concern the present work, no other type of detections are employed, but two spectrometers are used in coincidence mode. In addition, various kinds of events, true coincidence events, chance coincidence events, even single events are preferable to be taken simultaneously in a single run in order to reduce ambiguities. Therefore, required trigger logic is quite complicated. Accordingly, in the case of our previous $(p, 2p)$ measurements using standard NIM/CAMAC modules, it required about one week to construct the trigger circuit system, and at least a few days to check the circuits using actual beam, and even during data-taking run time after those setting process was finished, additional modification of the circuits system was sometimes required because of unexpected trouble in triggering. Such time consumption is hard to accept for the packed west-hall experiments and it has not been realistic to perform systematic studies with $(p, 2p)$ measurements.

In order to cope with these difficulties and realize systematic $(p, 2p)$ measurements, new trigger system by using Field Programmable Gate Array(FPGA) chips are newly developed and actually used in this work. The core of this system was made using LeCroy 2366 universal logic modules(ULMs) with FPGA chips. The logic circuits were designed by a CAD program on a personal computer and down-loaded to the FPGA chips.

The condition described above necessarily requires the trigger system to be usable in other combination of spectrometers and other detectors and the new system satisfies the requirement with minor modifications. In this chapter, the feature, advantages and disadvantages of FPGA are described. Overview of logic for the $(p, 2p)$ reaction are explained as well. Ideas utilized in, and the layout of the trigger system are detailed in the appendix B.

2.2 Field Programmable Gate Array(FPGA)

A Field Programmable Gate Array (FPGA) chip is an integrated logic circuit chip which is programmable and rewritable over and over again. In this section, the feature of FPGA chips, advantages and disadvantages in introducing FPGA chips for a trigger system are described.

2.2.1 Feature of FPGA

A FPGA chip is a flexible IC in response to down-loaded files complied by a personal computer. The feature of a FPGA chip as follows:

- Logic functions of a FPGA chip is programmable using a computer software.
- All common logic function such as ANDs, ORs and flip-flops in a FPGA are usable to in any combination.
- By using the software simulation, it is possible to test the designed circuits including propagation delay time in the chip, practically.
- One chip, with 5000 gates, of a typical grade includes as many complex logic functions as about 20-30 NIM modules.
- There are no functions which determine fixed time delays in the chip itself. Fixed time-interval can be handled only by synchronized to outside clock signals.

2.2.2 Advantages and Disadvantages Using FPGA for Trigger circuits

At RCNP, the trigger circuits have been constructed near detectors in the experimental room, because there are a enormous number of signals from several detectors. If there are enough number of of NIM/CAMAC modules, we can prepare another set of trigger circuits outside the experimental room when a preceding experiments is ongoing and

replace the trigger circuit with the prepared set for a next experiment. But it is impractical to move the set because the whole trigger system is too big and the movement may cause many troubles. In employing FPGA chips into trigger modules, there are several advantages:

- We can prepare practical trigger logic circuits on a PC, outside the experimental room.
  - During other experiment, we can create next trigger logic.
  - By a computer simulation, we can check the performance of trigger system beforehand.
  - It is relatively easy to redesign circuits and to repeat checking circuits on the application program because it is not necessary to rewire actually.
  - Likewise, it is comparatively easy to design very complex logic circuits using cut and paste.
- We make less mistakes because a FPGA chip occupy a central and major part and there are fewer connectors and wiring.
- Only by down-loading, we can reliably reconstruct a trigger logic circuit that was used previously.

But, there are some disadvantages in comparison with a conventional NIM/CAMAC system:

- In order to delay a signal, the signal must be synchronized to a clock timing. Therefore it is impossible to make delayed signals with arbitrary time lengths in principle.
- A full steps of preparing processes are required even for a minor modification of trigger logic. Even if a system test process is skipped for such minor modifications designing new logic, compiling the file, sending the file and down-loading the file on the FPGA chip are necessary.

  - In the case of conventional NIM/CAMAC system, contrarily, it requires only a several seconds to make a easy improvement using spare outputs of electronics.

- A circuit using a FPGA chip tends to be a black box for other people who didn't program the loaded file.

2.3 Trigger Circuit for $(p, 2p)$ Reactions

In this section, the trigger circuit is describe especially for the $(p, 2p)$ reaction . For measurements of the $(p, 2p)$ reaction, we use two spectrometers. We acquire coincidence event date and also single event data of each.

2.3.1 Requirement for $(p, 2p)$ reactions

It is important to take not only coincidence event data but also simples event data in such correlation measurements. The reason is as follows.

The event count of "singles" is proportional to a beam current and a thickness of the target. On the other hand, that of "coincidence" isn't proportional to those because of accidental coincidence. At the same run, that is at the same background, at the same setting of angles and magnetic fields, and same DAQ system, the effective region and efficiencies of detectors are same and dead time is also same. Therefore, at the same condition, the measurement of two different quantities give redundancies in the date. Comparing two quantities, we can check the consistency of the measurement and if the detection ratio change, we can decide whether the change is responded to from conditions of detectors or distribution of quantities. For example, in one series measurement, where the one detector is fixed at a angle and a magnetic field and another detector is at some points of conditions, the differential cross section of the former singles does not change, but that of the coincidence events changes. The coincidence data can be normalized by that of the former.

As described above, the "singles" is important at a coincidence measurement but we can

not take all of "singles" data because the event rate of singles are too high, about several hundreds times of the coincidence events on each side. So, we want to get "singles" data at the slow down rate. Therefore, our requirement of trigger events is that all coincidence events of two spectrometers and sampling event of "singles" at each side spectrometer. This requirement is difficult and cause trigger logic circuits to be complicated and be large. But it is necessary for us to take coincidence data with consistency in a limited beam time.

2.3.2 Logic for Trigger Conditions

In the experiments for the $(p, 2p)$ reaction, we used the spectrometers GR and LAS. Signals of each scintillator array behind each spectrometer were used for trigger input signals. These signals were split and were also used for ADC and TDC input signals. In this subsection, signals are described only concerning the trigger logic.

Figure 2.1 shows overview of logic diagram for this system and Figure 2.2 shows schematic logic diagram for "Front-GR" in Fig. B.2. We acquired a coincidence event with a "GR event" and a "LAS event", called as "GR&LAS COIN", and single event for each, called as "GR Single Sample" and "LAS Single Sample" as a mention above the subsection 2.3.1.

At first, "GR events" and "LAS events" are defined by scintillator signals. We call as "GR events" for the condition satisfied signals from scintillators on the GR. The logic diagram of "GR event" condition and the schematic diagram is shown in Fig.2.3. The signals from left and right PMT(PhotoMultiplier Tube)s of scintillators are discriminated by constant fraction discriminator(CFD)s. By using a Mean-Timer module, which generates average signal in terms of time from two signals, the coincidence signal is generated from the both side outputs of the CFDs from each scintillator. On the GR, there are two scintillators front and rear and outputs of two Mean-Timer from these scintillators are called as PS1 and PS2, respectively. After two signals PS1 and PS2 are inputted into a LC 2366 ULM, the "GR event" is generated by the coincidence of these two signals. The

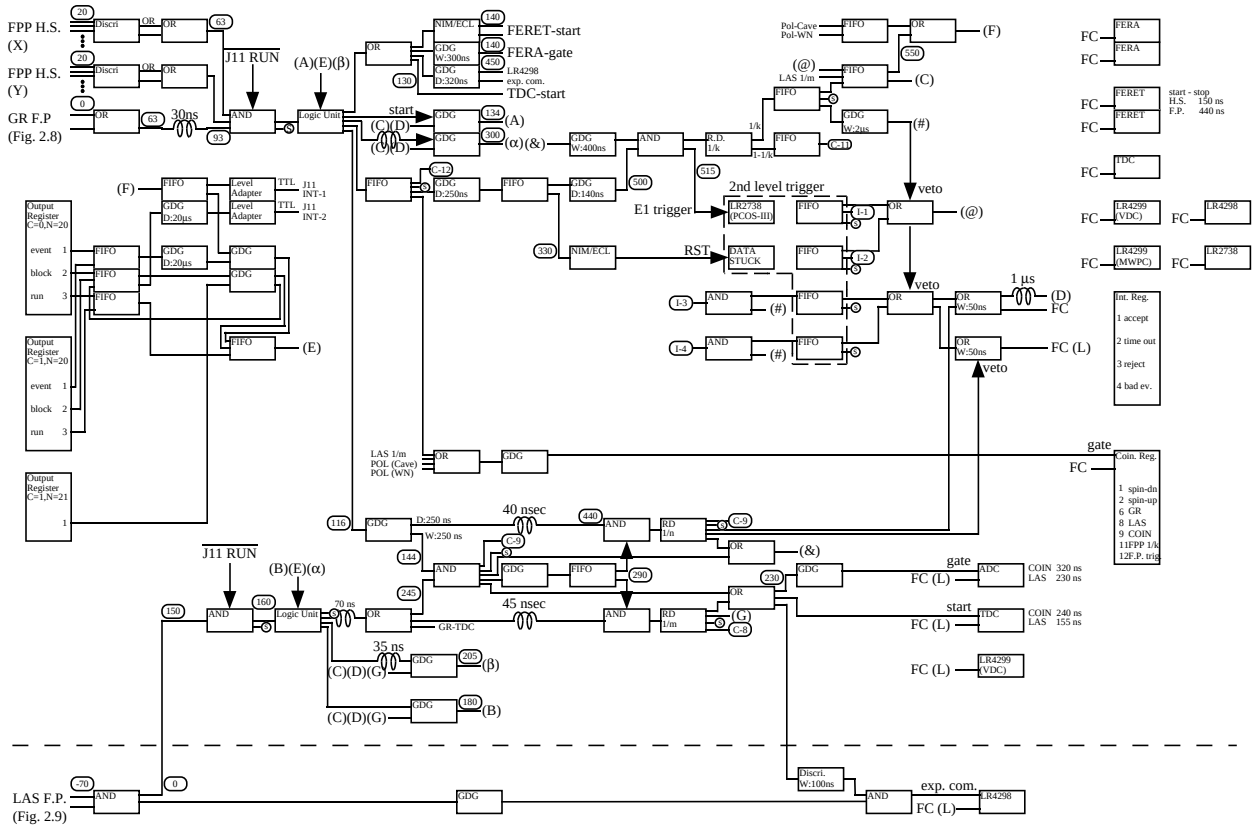

Figure 2.1: The circuit diagram of trigger logic for $(p, 2p)$ reactions. This figure is described for previous trigger circuits in Ref [43] based on standard NIM/CAMAC modules, where the functions of these circuits is basically included by the new trigger system.

timing and width between PS1 and PS2 are tuned before inputting the LC 2366 ULM.

We also call as "LAS events" for the condition satisfied signals from scintillators on the LAS. The logic diagram of "LAS event" condition and the schematic diagram is shown in Fig.2.4. For the "LAS event", the condition and logic is similar to the "GR event", but there are three scintillators on each plane, front and rear. For "LAS events", one LC 2366 ULM is used so that we can use other condition or additional coincidence signal or veto signal for example the RF signal and Hodoscope scintillator.

Next, each event, which is the "GR event" or the "LAS event", is identified as "GR&LAS COIN" or "GR Single" or "LAS Single". Figure 2.5 shows logic diagram for trigger events and Fig. 2.6 shows the circuit of the coincidence unit in FPGA, where the design was

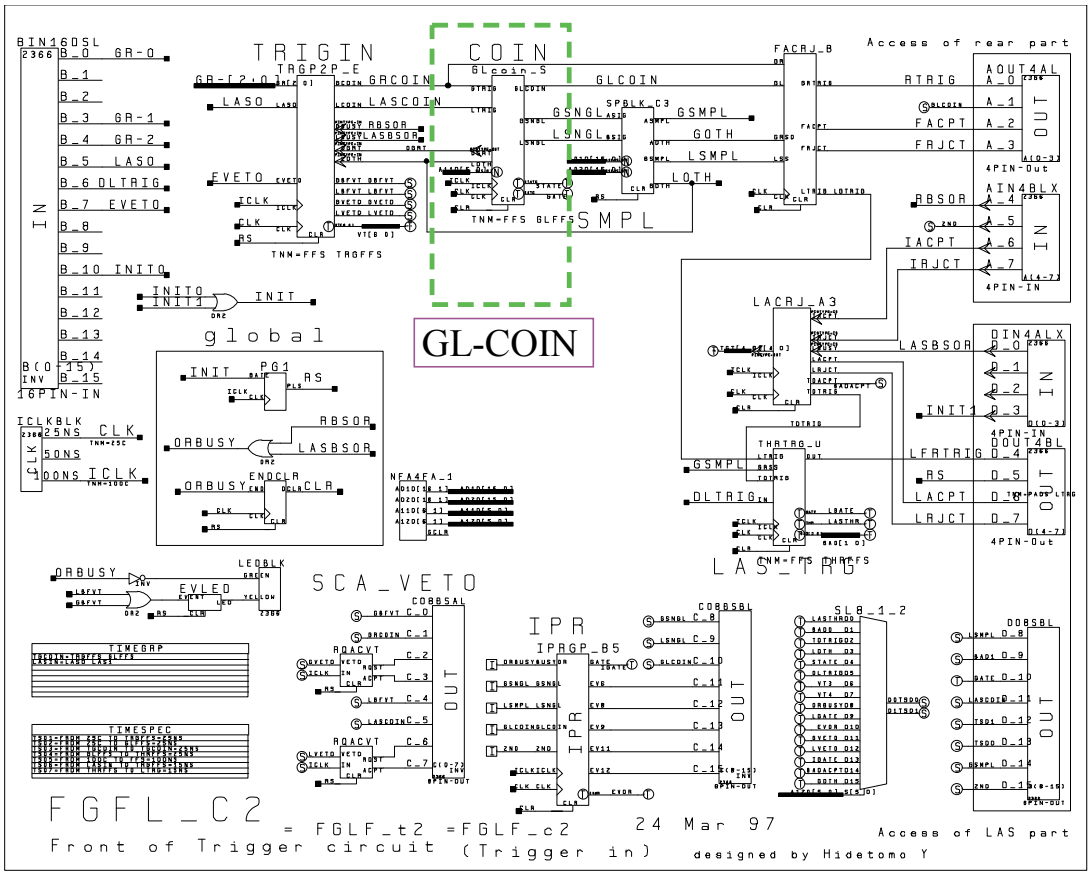

Figure 2.2: Schematic diagram of the trigger system for "Front-GR". This figure is top floor of the hierarchy of design programmed in CAD.

programmed by using CAD. The coincidence gate is generated from the "GR event" and the leading edge opened on fixed time from "GR event", on the other hand, jitter of the tailing edge is caused by the 40MHz clock synchronized in a FPGA chip. The coincidence gate time width is flexible between about 50nsec and 1.6 μsec and changed by using CAMAC function. In the experiments, typical gate time width was set about 450 nsec.

The "GR&LAS COIN" event is generated by coincidence of the "LAS event" and the coincidence gate. The "GR Single" event is determined when no "LAS event" arrives in the time when the coincidence gate closes. And the "LAS Single event" is determined when "LAS event" arrives in the trigger circuit with no coincidence gate, except during

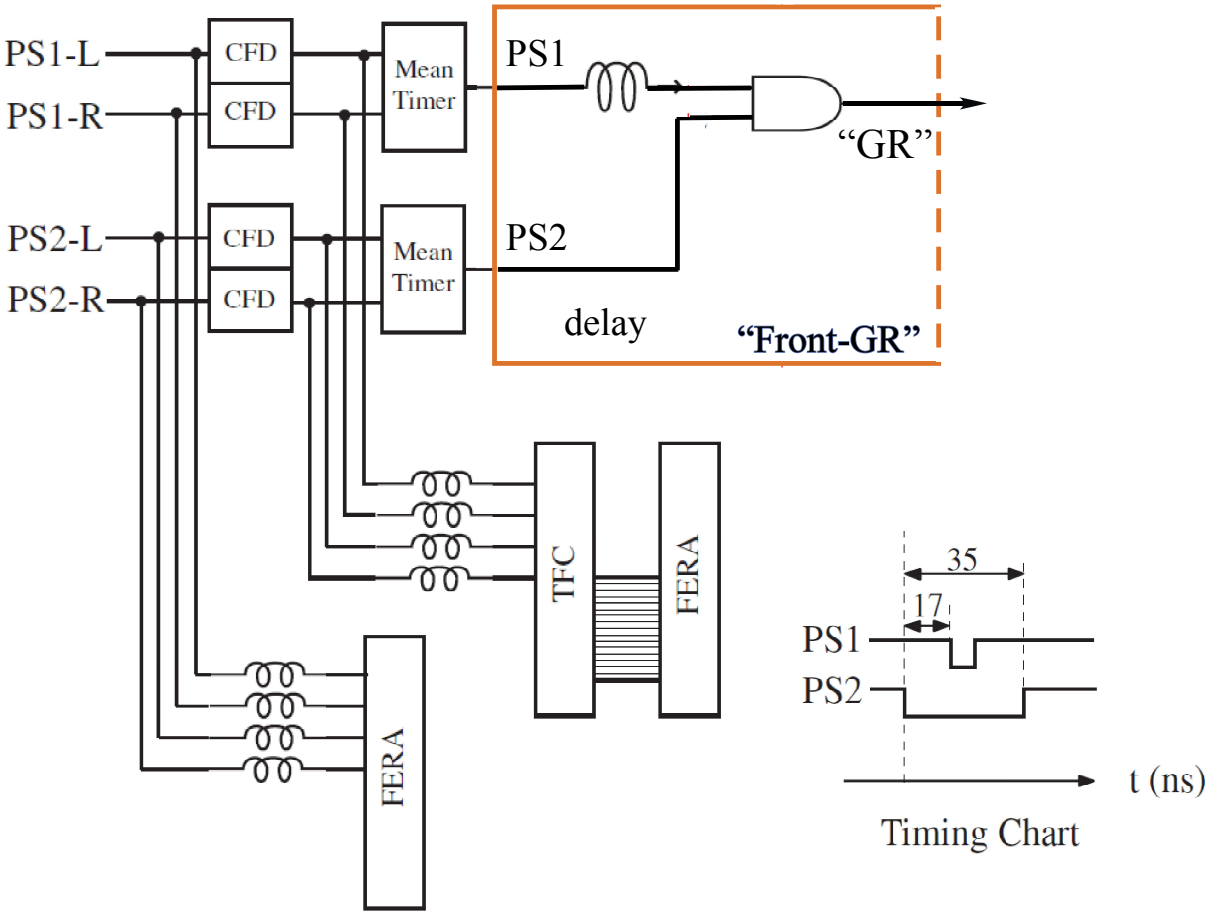

Figure 2.3: The circuit diagram for GR focal plane detector. The region in the square show a part of "Front-GR", which is one of FPGA modules for the trigger system.

data taking of earlier event accepted.

Each single event, "GR Single" or "LAS Single" are counted in the trigger circuits, respectively. And "n"-th or "m"-th event were distinguished from other events. The data of the "n"-th "GR Single"event called as "GR Single Sample" and the data of the "m"-th "LAS Single" event as "LAS Single Sample" are acquired and each counter in the circuits is cleared during the acquisition. The numbers, "n" and "m" can be set by CAMAC functions and be chosen from 0 to 65535. When the number is set "0", it means that the data of single event isn't acquired at all. For the experiments, those sampling number were 30–1000 chosen for the event rate and the dead time of the DAQ.

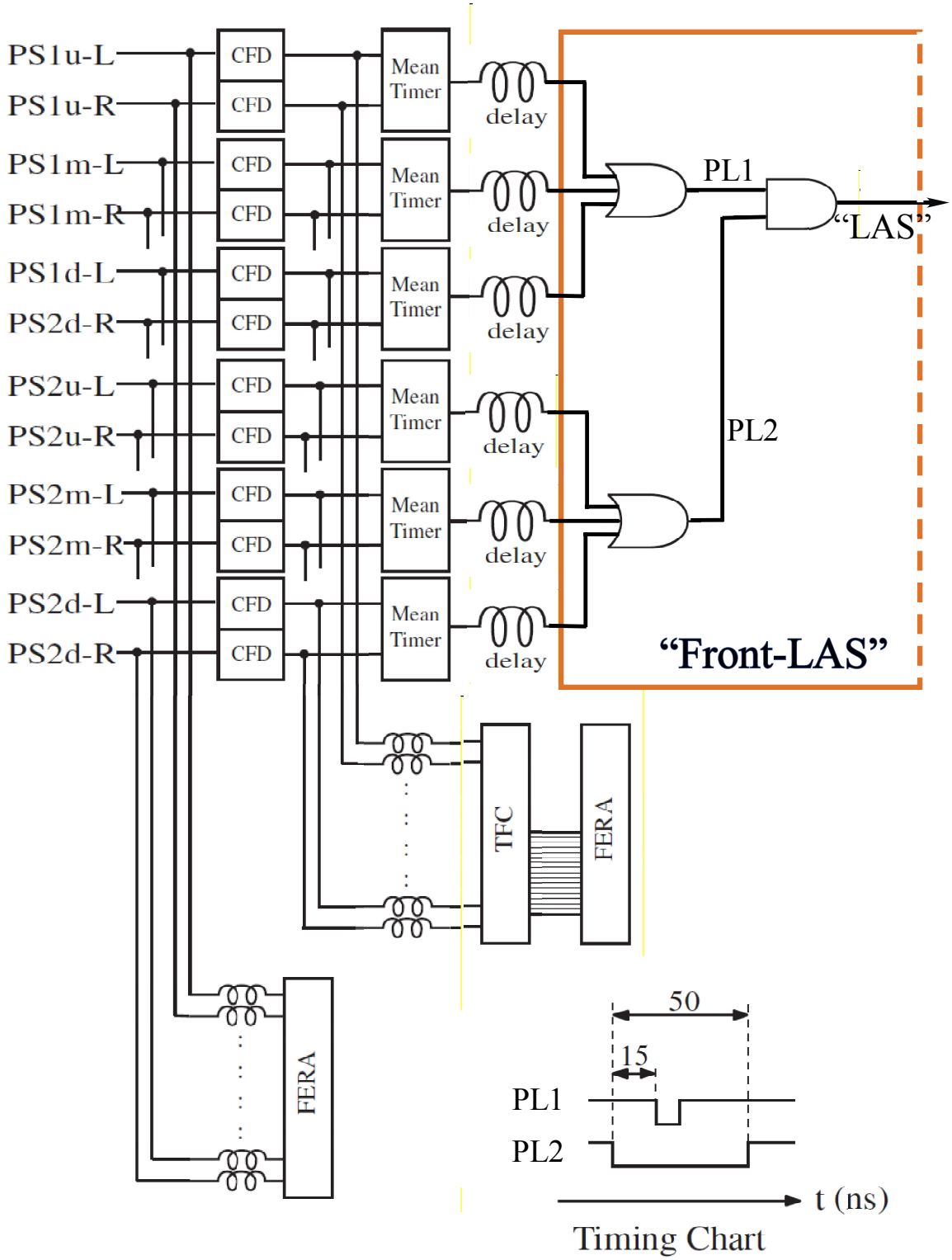

Figure 2.4: The circuit diagram for LAS focal plane detector. The region in the square show a part of "Front-LAS", which is one of FPGA modules for the trigger system.

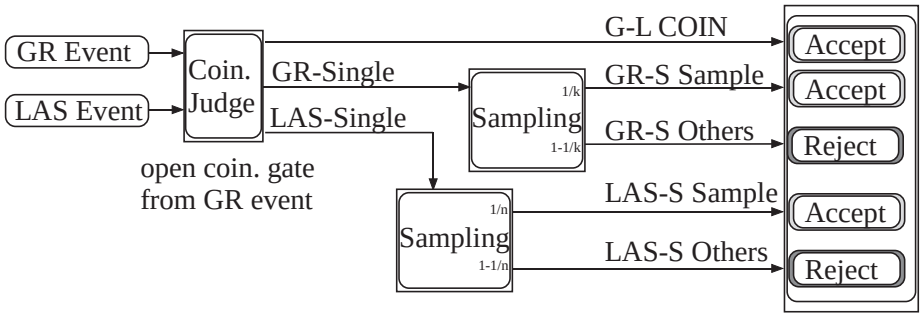

Figure 2.5: The logic diagram for a judgment for accept or reject events:

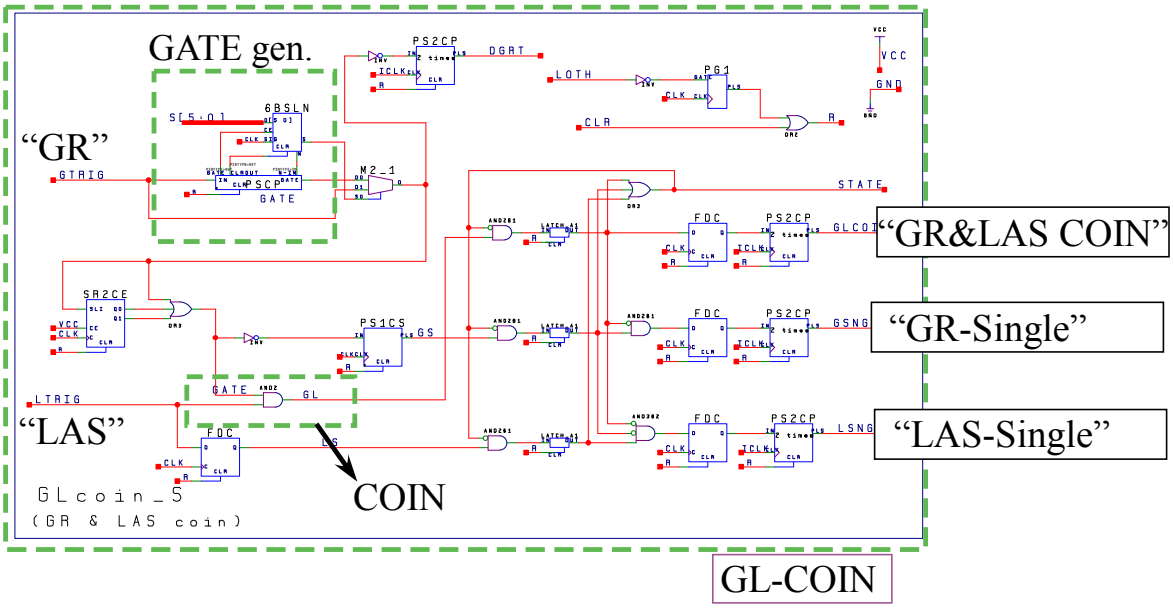

Figure 2.6: The design of a coincidence unit in FPGA. This figure corresponds to the "GL-COIN" unit which is the part of "Front-GR" in Fig. 2.2 and the "Coin. Judge" part of logic diagram in Fig. 2.5.

To acquire data, the trigger circuits access control modules those treat ADC's and TDC's modules, continuously. After getting the signals for data transfer end, the circuits clear ADC's and TDC's modules. The circuits can access the control modules in parallel. So, for each event acquired, the data taking time is typically 20–30 μsec.

2.4 Results of the Development

By using modules, LC 2366 ULMs, equipped with FPGA chips, a trigger system which can be shared for many kinds of experiments using the spectrometer GR and other detectors in combination. In the program for the FPGA chips, both of synchronous and asynchronous timing controls are used so as to keep real time information and to realized complex trigger logic.

The results of the development for trigger system is as follows:

- The system is adaptable to various experiments even if the combination of detectors is different, because the appropriate files can be down-loaded into FPGA chips and it is not necessary to rewire actually.
- When we change from the experiment one to another, a required time to change the trigger circuit becomes much shorter. For example, it takes only a few hours to check and to change to the experiment of set of two spectrometers for $(p, 2p)$ reactions.
- Reconstructing the trigger system for a new combination of detectors takes much less time then before because the new logic circuits can be designed in computer so that modification is easy.
- We can eliminate almost wiring and logical mistakes because it is little necessary to rewire in the system. So the system is very reproducible.
- At one experiment, we can change minor setting by computer commands for same combination of detectors.

Now, this system is employed as a standard trigger system for all of experiments using the spectrometer GR which is most frequently used equipment at RCNP. Owing to the efficiency of the spectrometer experiments at RCNP are improved very much.

A similar trigger system is also used as a data taking system for beam line polarimeters (BLPs). In appendix C, a brief description of the system is given.

Chapter 3

Experimental Detail

3.1 Overview

The measurement was performed at the Research Center for Nuclear Physics (RCNP), Osaka University. Layout of the experimental facility at RCNP is shown in Figs. 3.1 and 3.2. Most of the measurements were carried out on July, 1998 using the old WN course, and a precise measurement for ^{6}Li target was performed on April, 2004 using the new WS course. In this section, the kinematical conditions and experimental details are described.

3.2 Kinematics

For $(p, 2p)$ reactions, the energy and the momentum conservations give the following equations,

$$\boldsymbol{k}_0 = \boldsymbol{k}_1 + \boldsymbol{k}_2 + \boldsymbol{k}_3,$$

$$T_0 = T_1 + T_2 + T_3 + (E_x - Q),$$

and separation energy is defined by

$$E_{\rm sep} \equiv E_x - Q.$$

Then,

$$\boldsymbol{k}_3 = \boldsymbol{k}_0 - \boldsymbol{k}_1 - \boldsymbol{k}_2, \tag{3.1}$$

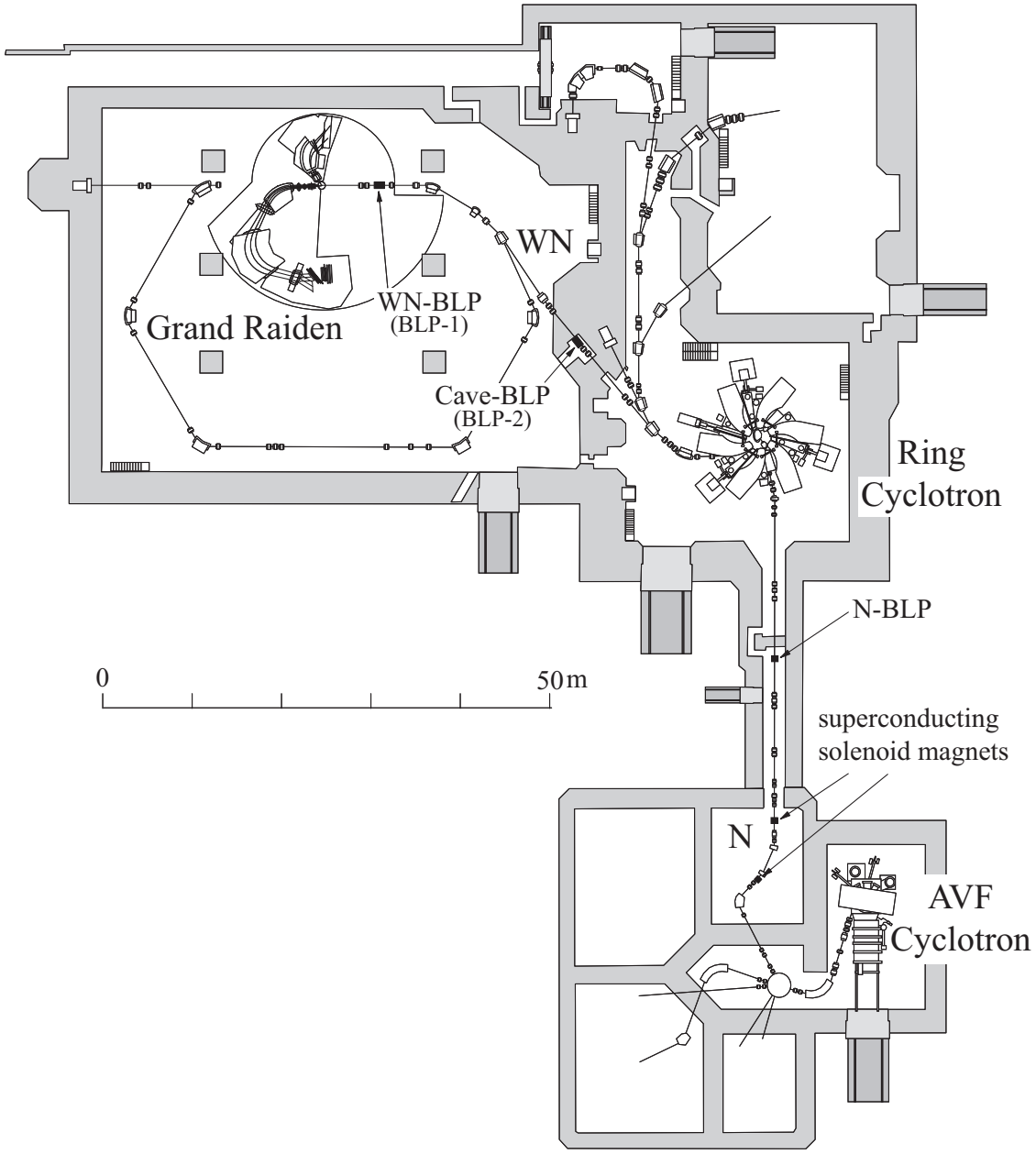

Figure 3.1: A layout of the experimental facility at RCNP. with the old WN course.

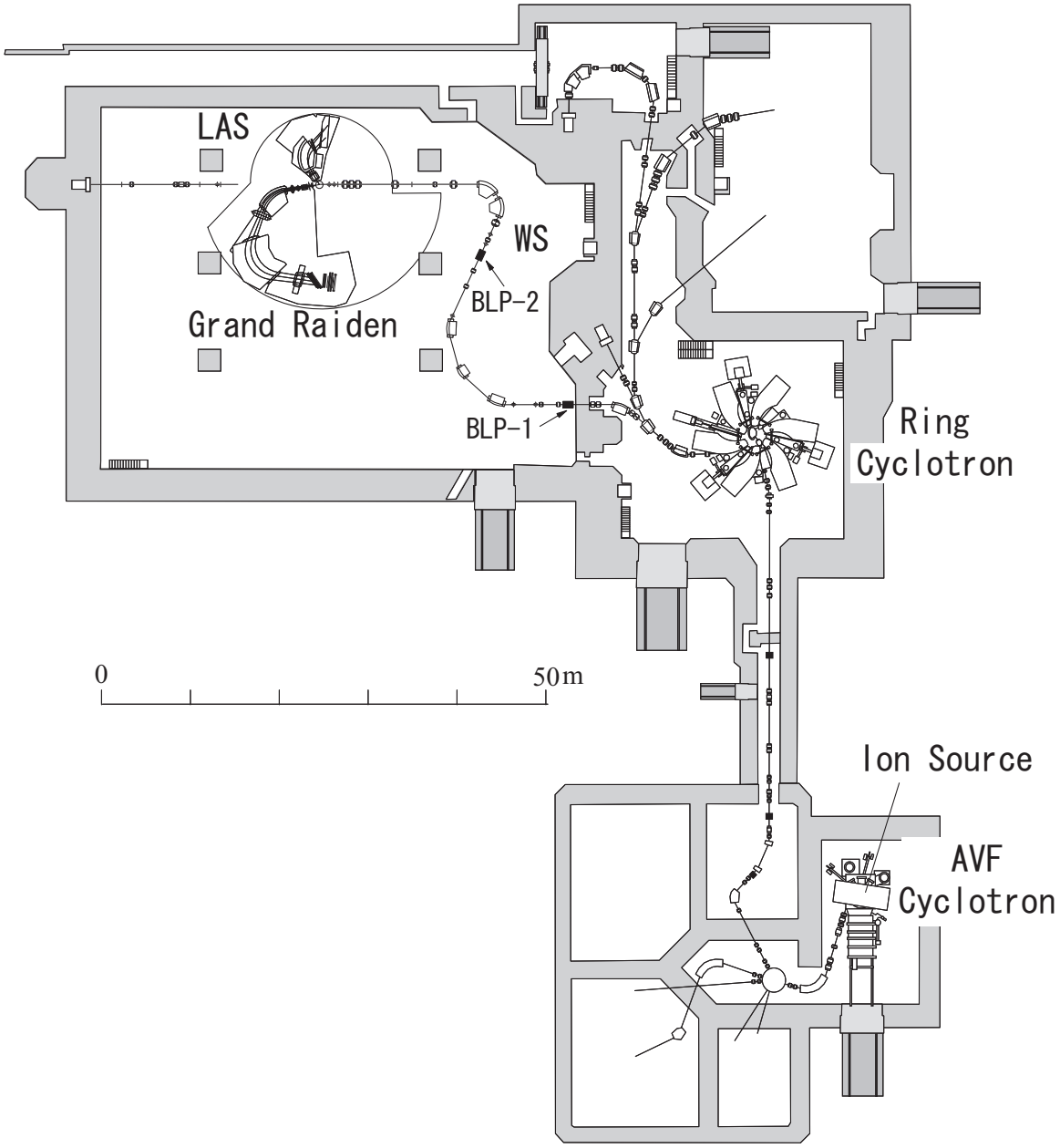

Figure 3.2: A layout of the experimental facility at RCNP with the new WS course.

$$E_{\rm sep} = T_0 - (T_1 + T_2 + T_3). \tag{3.2}$$

Here, $\boldsymbol{k}_i$ and T_i are the momentum and the kinematical energy, respectively, for the incident (i=0) proton, two outgoing (i=1,2) protons and the recoil (i=3) nucleus. Figure 3.3 illustrates these quantities. When the incident proton energy is known, the recoil momentum $\boldsymbol{k}_3$and separation energy $E_{\rm sep}$ can be determined with Eqs. (3.1) and (3.2), respectively.

As mentioned in Sec. 1.3, one of the purposes of this experiment is to examine the reliability of DWIA calculations for various kinematical conditions of $(p, 2p)$ reactions. In order to reduce ambiguities in optical potential parameters used in DWIA calculations, we mainly measured the recoil momentum distributions of differential cross section and A_y by keeping the energies of outgoing protons. In addition, we also performed measurements under another kinematical condition,

Figure 3.4 is a contour plot of recoil momentum $\boldsymbol{k}_3$ when $E_{\rm sep}$ and T_1 are fixed, consequently T_2 is almost constant. The horizontal and vertical axes are the emission angles of two protons, θ_1 and θ_2, which correspond to the setting angles of the GR and the LAS, respectively. At the center of the contour, displayed by ④, the recoil momentum $\boldsymbol{k}_3$ is zero and the kinematical conditions for constant $|\boldsymbol{k}_3|$ values are plotted by solid lines in 50 MeV/c steps. In the figure, the kinematical conditions of the present measurement are also shown by dashed lines with circled numbers. The condition ① is a series of the settings where the angle and the energy of one outgoing proton were fixed and the angle of another outgoing proton was changed. The conditions ② and ③ correspond to the settings where the scattering angle and the energy of two body scattering system are fixed, respectively. In addition, we also performed a so-called energy-sharing measurement, namely the measurement by changing the ratio of the two outgoing energies, T_1/T_2, keeping the angles fixed at ④. For ^{40}Ca and ^{12}C, the measurements along all of those four conditions were carried out, whereas the measurement along the condition ① was performed for ^{6}Li.

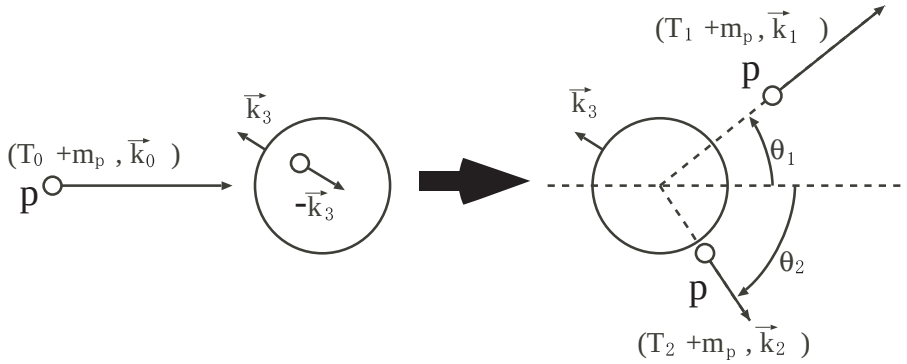

Figure 3.3: The $(p, 2p)$ reaction in the laboratory coordinate system for a coplanar (ϕ_1=ϕ_2=0) condition. Four-momenta are indicated as (T_i+m_p , $\boldsymbol{k}_i$) for incident (i=0) and two outgoing (i=1,2) protons. $\boldsymbol{k}_3$ represents the recoil momentum.

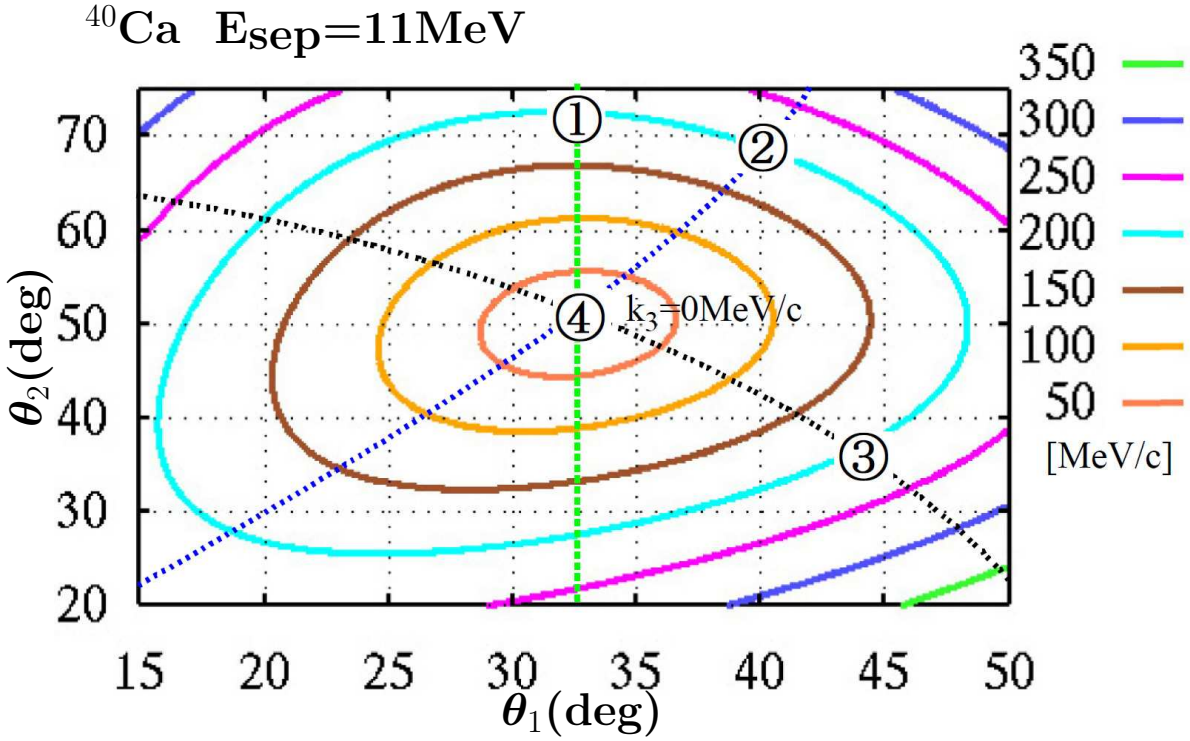

Figure 3.4: A contour plot of the recoil momentum as a function of the detection angles, θ_1 and θ_2. The calculation is made for the E_{sep}=11MeV knockout from ^{40}Ca$(p, 2p)^{39}$K for T_1=250MeV. The lines ①, ②, and ③ represent the three kinds of conditions employed for the present study. We also measured at ④ where θ_1 and θ_2 are fixed but T_1 and T_2 are changed. See text for details.

3.3 Polarized Proton Beam and Beam Line Polarimeter

Polarized protons from an atomic-beam type polarized ion source [44] were injected into the $K = 120$ MeV AVF (Azimuthally Varying Field) cyclotron and accelerated to 64.2 MeV. The protons were then transfered to the $K = 400$ MeV ring cyclotron [45] and accelerated to 392 MeV. The beam was transported to the center of the scattering chamber through the WN or WS beam line, and stopped at a Faraday cup placed in the wall about 25m downstream. The beam charge collected by the Faraday cup was integrated and monitored by using a current digitizer. The beam current was in the range of 50−300 nA.

There were two beam-line polarimeter systems (BLPs) in the beam line. The beam polarization was monitored using the left-right asymmetry of proton-proton scattering off a polyethylene target using a coincidence method. The detection angle of forward scattered protons was 17.0° and the effective analyzing power used was 0.45±0.01 [46]. The typical beam polarization was about 65%. The polarization direction was reversed every 1s in order to reduce possible instrumental asymmetries. The difference of polarizations for spin-up and spin-down modes was less then 5%. In the measurements, the BLP1 was used for polarization monitoring, and the BLP2 with an aramid target was used as a beam-current monitor for a consistency check.

3.4 Targets

Self-supporting $^{\mathrm{nat}}$Ca,$^{\mathrm{nat}}$C and ^{6}Li targets listed in Table 3.1 were used in this experiment. The thicknesses of the targets were determined by a weighting method and the uncertainties were estimated to be about 4%.

Table 3.1: Target enrichmentx and thicknesses

Nucleus	Enrichment(%)	Thickness(mg/cm^2)
^{40}Ca	96.94(natural)	37.0
^{12}C	98.89(natural)	33.9
^{6}Li	95.64	26.1
^{6}Li	95.64	37.6*

*) For the precise measurement described in Chap. 6.

3.5 Two–arm Spectrometer and Counter System

Two ejected protons in the (p,2p) reaction were detected with the two–arm spectrometer system which consists of the high resolution spectrometer Grand Raiden (GR) and the Large Acceptance Spectrometer (LAS). A schematic view of the system is shown in Fig. 3.5.

The angular acceptances of the GR and the LAS were limited by the entrance slits of the spectrometers. The opening angle of the GR slit was $\pm 20^W \times \pm 30^H$ (mr^2) and that of the LAS slit was $\pm 50^W \times \pm 45^H$ (mr^2), respectively. The momentum of the GR was $\pm$ 2.2 % and that of LAS was wide enough to accept all of the protons relevant acceptance to the $(p, 2p)$ reactions.

3.5.1 Spectrometer Grand Raiden

The left side spectrometer in Fig. 3.5 is the high resolution spectrometer Grand Raiden (GR) [47, 48], which consists of three dipole (D1, D2, and DSR), two quadrupole(Q1 and Q2), a sextupole (SX), and a multipole (MP) magnets. It provides a large momentum resolving power $p/\Delta p$ of $37,000$ with a 5% acceptance. The design specifications of Grand Raiden are summarized in Table 3.2. In the present experiments, the DSR and MP magnets were not used. The magnetic fields of the Dipole magnets (D1,D2) were monitored by an NMR method during the experiments.

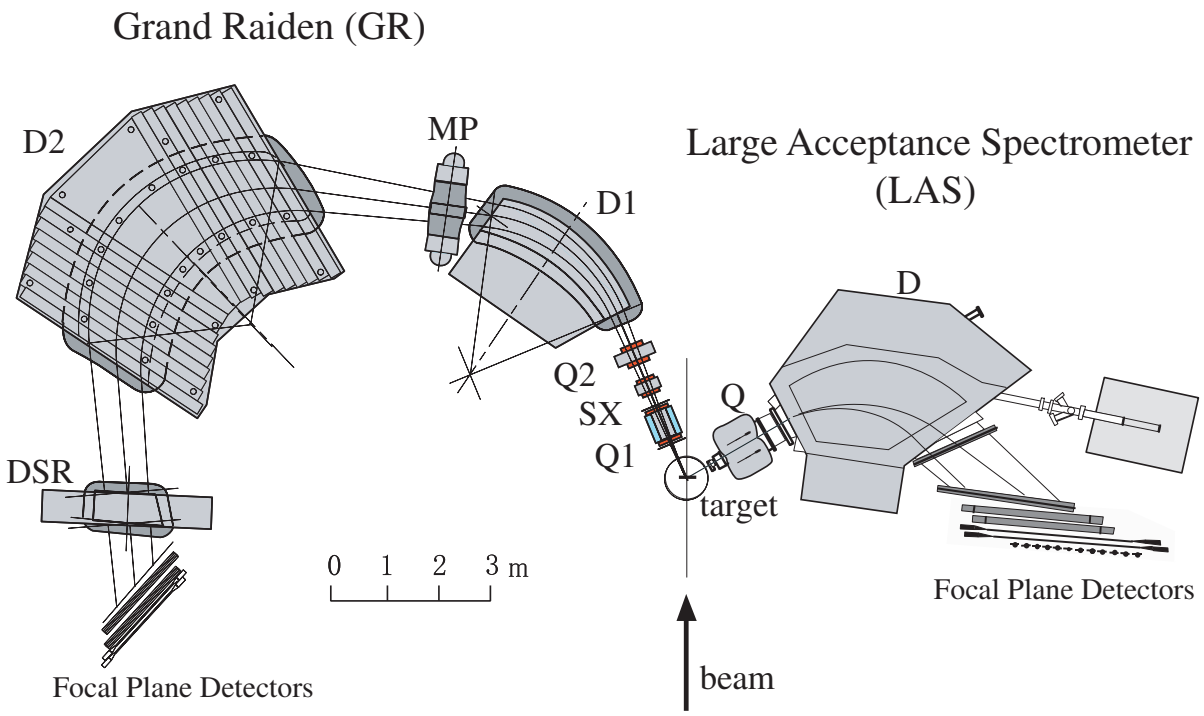

Figure 3.5: Schematic view of the two-arm spectrometer system at RCNP. The high resolution spectrometer Grand Raiden (GR) is placed on the left side of the beam line and the Large Acceptance Spectrometer (LAS) is on the right side.

Table 3.2: Design specifications of the two spectrometers at RCNP[48, 49].

	Grand Raiden (GR)	Large Acceptance Spectrometer (LAS)
Configuration	QSQDMD(+D)	QD
Radius of the central orbit	3 m	1.75 m
Total bending angle	162°	70°
Tilting angle of focal plane	45°	57°
Maximum magnet rigidity	5.4 T·m	3.2 T·m
Horizontal magnification $(x\|x)$	6.0	−7.3
Vertical magnification $(y\|y)$	−0.42	−0.4
Momentum range	±5 %	±15 %
Momentum resolution	37,076	4,980
Acceptance of horizontal angle	±20 mr	±60 mr
Acceptance of vertical angle	±70 mr	±100 mr

3.5.2 Large Acceptance Spectrometer - LAS

The spectrometer LAS [49, 50] has relatively wide momentum and angular range compared with the GR. A designed value of the momentum bite is about ± 15% and a solid angle is about 20msr. The LAS consists of one quadrupole (Q) and one dipole (D) magnets as shown in Fig.3.5. The design specifications are summarized in Table 3.2.

3.5.3 Focal Plane Detector System

The focal plane counter system for each spectrometer consists of two sets of multi-wire vertical drift chambers (MWDCs) and two layers of ΔE plastic scintillators behind the MWDCs. Two MWDCs determine positions and angles of incident particles [51].

Specifications of the MWDCs for the GR and the LAS are listed in Tables 3.3 and 3.4, respectively. The GR drift chamber consists of two sets of anode wire planes and the LAS one consists of three sets of anode planes though two of them, X and U, were used in these experiments.

The ΔE's signals from the scintillators were used for particle identification. The event trigger signals for $(p, 2p)$ reactions were generated as coincidence signals of the GR and the LAS scintillator signals.

The time difference of these GR and LAS signals was used to identify true and accidental coincidence events, and typical ratio of true to accidental events was 4:1. During the measurement, the MWDC efficiencies of the GR and the LAS were 91–94% and 78–88%, respectively, and the dead time of the data acquisition system was about 5%.

3.6 Data Acquisition System

Details about the trigger system was already described in Chap. 2. A schematic view of the data acquisition (DAQ) system of the WS course at RCNP [52, 53] is illustrated in Fig. 3.8. In $(p, 2p)$ measurements, each event was constructed of the drift-time data

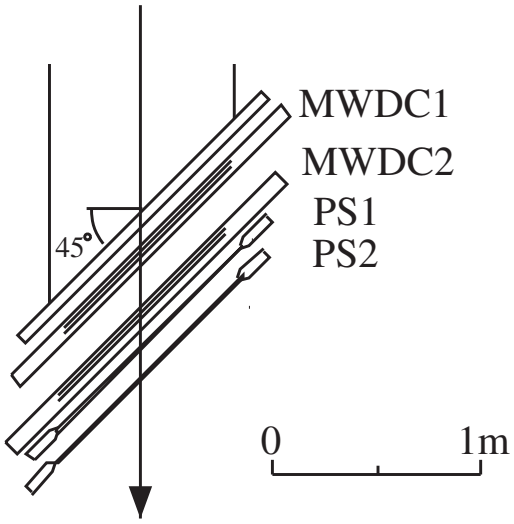

Figure 3.6: Focal plane detectors for Grand Raiden.

Table 3.3: Specifications of the MWDC's for Grand Raiden.

Wire configuration	X (0°=vertical), U (-48.2°)
Active area	1150^{W} mm × 120^{H} mm
Number of sense wires	192 (X), 208 (U)
Cathode-anode gap	10 mm
Anode wire spacing	2 mm
Sense wire spacing	6 mm (X), 4 mm (U)
Sense wires	20 μmϕ gold-plated tungsten wire
Potential wires	50 μmϕ gold-plated beryllium copper wire
Cathode	10 μm-thick carbon aramid film
Applied voltage	-5.6 kV (cathode)
	-350 V (X), -500 V (U) (potential wire)
Gas mixture	Argon (71.4%) + Iso-butane (28.6%) + Iso-propyl-alcohol (2° v.p.)
Gas seal	12.5 μm Aramid film
Pre-amplifier	LeCroy 2735DC
TDC	LeCroy 3377

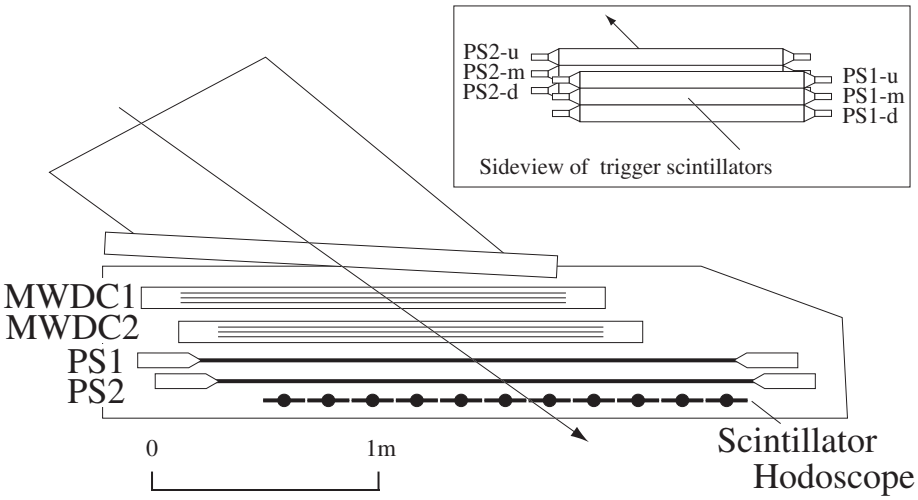

Figure 3.7: Focal plane detectors for LAS.

Table 3.4: Specifications of the MWDC's for the LAS.

Wire configuration	X (0°=vertical), U (-31°), V (+31°)
Active area	1700^{W} mm $\times$ 350^{H} mm
Number of sense wires	272 (X), 256 (U, V)
Cathode-anode gap	10 mm
Anode wire spacing	2 mm
Sense wire spacing	6 mm
Sense wires	20 μmϕ gold-plated tungsten wire
Potential wires	50 μmϕ gold-plated beryllium copper wire
Cathode	10 μm-thick carbon aramid film
Applied voltage	-5.5 kV (cathode), -300 V (potential wire)
Gas mixture	Argon (71.4%) + Iso-butane (28.6%) + Iso-propyl-alcohol (2° v.p.)
Gas seal	25 μm Aramid film
Pre-amplifier	LeCroy 2735DC
TDC	LeCroy 3377

from the MWDC's digitized by LeCroy3377 TDC, the charge and timing signals from the trigger scintillators encoded with LeCroy430x FERA and FERET system, where two sets of MWDC's and scintillators were used for two focal plane detector systems at GR and LAS, and the input register. In order to check the consistency of data flow, the event header, event number, and input register words were attached to every event by the Flow Controlling Event Tagger (FCET) [54].

The digitized data were transferred into memory buffers in a VME system (LeCroy 1191 Dual Port Memory) via the EC-Line bus. Since the memory buffers were operated in the double-buffer mode and the timing of the buffer change was controlled by Buffer Changer, which is the LeCroy2366 ULM included a FPGA chip and whose circuits were programmed by me, the dead time resulting from software management or data transfer via the CAMAC bus was effectively reduced. It is the characteristics of this DAQ system that software actions for data transfer modules were excluded.

During trigger system development, this DAQ system, called as TamiDAQ, was developed by A. Tamii at the same time. For a substitution of new computers, Work stations and board computer for VME modules, M. Uchida improvement the DAQ system, called as UchiDAQ. At the same time, I improved FPGA logic circuits for only BLP trigger system to adapt UchiDAQ. For trigger system of GR/LAS mentioned in Chap. 2 and Buffer Changer, I didn't need improve logic circuits, which were completed and operate independently of the computer system. For experiments of main parts in present work in Chap. 5, TamiDAQ system was used and for precise measurement in Chap. 6 UchiDAQ system was used.

The typical dead time for encoding events was about 20 –30μs/event. In the present measurements, the typical trigger rate, where the trigger events consisted of the GR+LAS coincidence trigger events, sampling events of the GR single events and sampling events of the LAS single events, was usually less than 800 Hz and, then, the live time ratio of the DAQ system was more than 90 %.

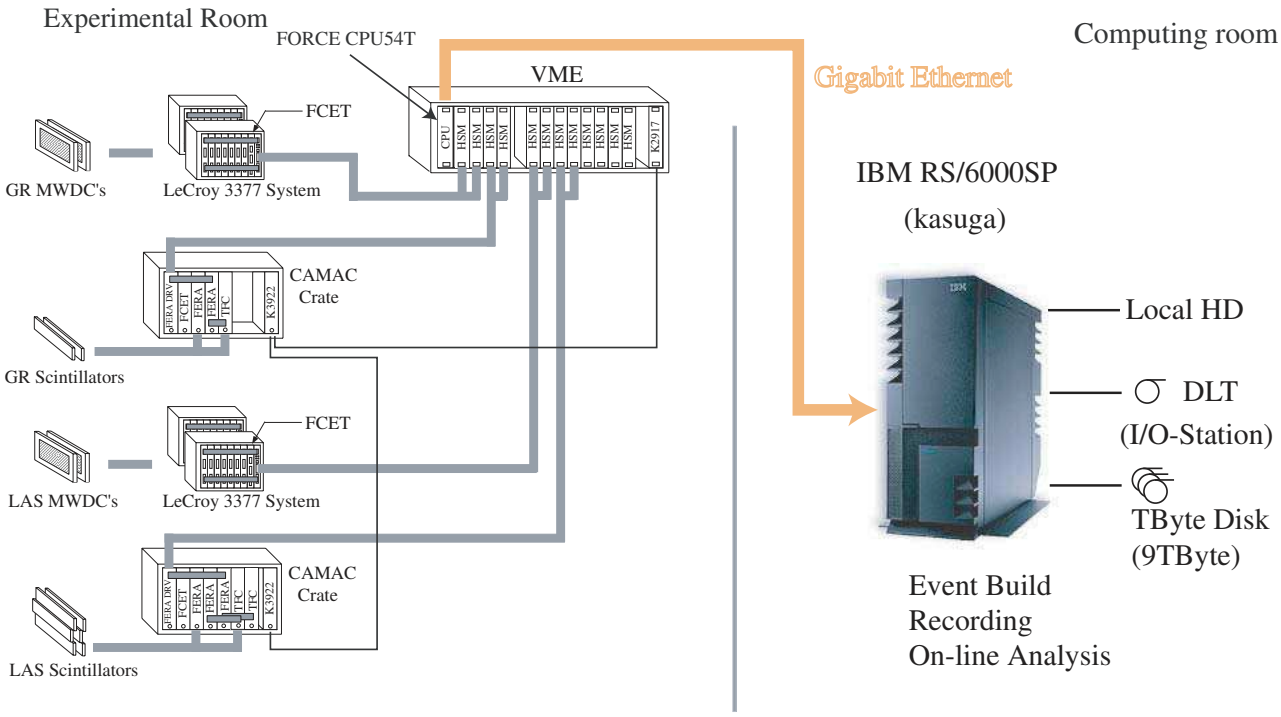

Figure 3.8: Schematic view of the data acquisition system (UchiDAQ) for the WS course at RCNP.

Chapter 4

Data Analysis and Experimental Result

4.1 Differential Cross Sections and Analyzing Power

The differential cross section of the $(p, 2p)$ reaction in the laboratory system is written as

$$\frac{d^3\sigma}{d\Omega_{\rm GR} d\Omega_{\rm LAS} dE_{\rm GR}} = \frac{Y}{Qa\epsilon l \Delta\Omega_{\rm GR} \Delta\Omega_{\rm LAS} \Delta E_{\rm GR}}, \tag{4.1}$$

where

$$\begin{aligned}
Y &: \text{number of } (p, 2p) \text{ coincidence events,} \\
Q &: \text{number of incident protons,} \\
\Delta\Omega &: \text{solid angle of each spectrometer,} \\
a &: \text{number of target particles,} \\
\epsilon &: \text{detection efficiency of GR and LAS,} \\
l &: \text{live time ratio of DAQ} \\
\Delta E_{\rm GR} &: \text{integrated region of } E_{\rm GR}.
\end{aligned}$$

The number of events for spin-up ($\uparrow$) (spin-down ($\downarrow$)) mode is given as

$$Y_\uparrow = \frac{d^3\sigma}{d\Omega_{\rm GR} d\Omega_{\rm LAS} dE_{\rm GR}} (1 + P_\uparrow A_y) Q_\uparrow a \epsilon_\uparrow l_\uparrow \Delta\Omega_{\rm GR} \Delta\Omega_{\rm LAS} \Delta E_{\rm GR}, \tag{4.2}$$

$$Y_\downarrow = \frac{d^3\sigma}{d\Omega_{\rm GR} d\Omega_{\rm LAS} dE_{\rm GR}} (1 + P_\downarrow A_y) Q_\downarrow a \epsilon_\downarrow l_\downarrow \Delta\Omega_{\rm GR} \Delta\Omega_{\rm LAS} \Delta E_{\rm GR}. \tag{4.3}$$

where $P_\uparrow$ ($P_\downarrow$) and A_y represent the beam polarization for spin-up (spin-down) mode and the analyzing power, respectively.

From Eqs. 4.2 and 4.3, the analyzing power is obtain as

$$A_y = \frac{1-\alpha}{P_\downarrow - P_\uparrow \alpha}, \tag{4.4}$$

with

$$\alpha \equiv \frac{Y_\downarrow Q_\uparrow l_\uparrow \epsilon_\uparrow}{Y_\uparrow Q_\downarrow l_\downarrow \epsilon_\downarrow}. \tag{4.5}$$

4.2 Beam Polarization

The beam polarization was continuously monitored using the BLP system. The event numbers of the left (L) and the right (R) BLP counters for spin-up ($\uparrow$) and spin-down ($\downarrow$) modes are given as

$$L_\uparrow = \sigma_0 N_0 Q_\uparrow \epsilon_L \Omega_L (1 + P_{y\uparrow} A_y^{\text{eff}}) \tag{4.6}$$

$$R_\uparrow = \sigma_0 N_0 Q_\uparrow \epsilon_R \Omega_R (1 - P_{y\uparrow} A_y^{\text{eff}}) \tag{4.7}$$

$$L_\downarrow = \sigma_0 N_0 Q_\downarrow \epsilon_L \Omega_L (1 + P_{y\downarrow} A_y^{\text{eff}}) \tag{4.8}$$

$$R_\downarrow = \sigma_0 N_0 Q_\downarrow \epsilon_R \Omega_R (1 - P_{y\downarrow} A_y^{\text{eff}}), \tag{4.9}$$

where each symbol means[1]:

$A_y^{\rm eff}$: the effective analyzing power of the system

σ_0 : cross section for p-p elastic scattering,

N_0 : the number of target particles,

Q : the number of incident protons,

P_y : beam polarization,

ϵ : detection efficiency,

Ω : solid angle.

Now, from Eqs. 4.6-4.9, effective acceptance $\epsilon_L\Omega_L$ and $\epsilon_L\Omega_L$ are obtained by

$$\epsilon_L\Omega_L = \frac{1}{2\sigma_0 N_0}\frac{L_\uparrow R_\downarrow - L_\downarrow R_\uparrow}{Q_\uparrow R_\downarrow - Q_\downarrow R_\uparrow}$$
$$\epsilon_R\Omega_R = \frac{1}{2\sigma_0 N_0}\frac{R_\uparrow L_\downarrow - R_\downarrow L_\uparrow}{Q_\uparrow L_\downarrow - Q_\downarrow L_\uparrow}.$$

Then, the ratio $\epsilon_L\Omega_L/\epsilon_L\Omega_L$ is obtained by

$$\lambda \equiv \frac{\epsilon_L\Omega_L}{\epsilon_R\Omega_R} = \frac{Q_\downarrow L_\uparrow - Q_\uparrow L_\downarrow}{Q_\uparrow R_\downarrow - Q_\downarrow R_\uparrow}. \tag{4.10}$$

Practically, the ratio of the solid angles does not vary throughout the measurement under constant beam transportation. And differences of detection efficiencies are expected to be negligible. λ were derived by using the total events of all data runs. The values of λ are 1.01 and 1.00 of the experiment in Chap. 5 and that in Chap. 6, respectively.

Therefore, as the beam polarizations, the following equation was used.

$$P_{y\uparrow(\downarrow)} = \frac{1}{A_y^{\rm eff}}\frac{L_\uparrow(\downarrow)/R_\uparrow(\downarrow) - \lambda}{L_\uparrow(\downarrow)/R_\uparrow(\downarrow) + \lambda} \tag{4.11}$$

[1]Actually, $A_y^{\rm eff}$ is slightly modified from A_y value for p-p scattering because of contribution from the quasifree scattering off the carbon nuclei in the target. We used 0.45±0.01 for $A_y^{\rm eff}$.

Since the statistical error of λ is negligibly smaller than the systematic error of the effective analyzing power, $A_y^{\rm eff}$, the estimated statistical error of the beam polarization is written as follows.

$$\Delta p = \frac{1}{{A_y^{\rm eff}}^2(L+\lambda R)}\sqrt{(L^2-\lambda^2R^2)^2\Delta {A_y^{\rm eff}}^2 + 4{A_y^{\rm eff}}^2\lambda^2(R^2\Delta Y^2 + L^2\Delta R^2)} \qquad (4.12)$$

In this study, the ranges of the beam polarization were between 0.60 and 0.66 during the experiment in Chap. 5 and between 0.63 and 0.68 during that in Chap. 6.

4.3 Particle Identification

Signals from the scintillation counters in each focal plane of GR and LAS were used not only for event trigger signals but also for particle identifications. Energy-loss of a particle passing through the scintillation counter depends on the charge, the mass and the energy of the particle. We detected the energy-loss by photo multipliers (PMT's) attached on both sides of each scintillator.

The light intensity at a PMT can be written as

$$H(x) = H_0 \exp(-x/\lambda), \qquad (4.13)$$

where H_0 is the light intensity at the position where it is emitted, H is the light intensity after it has traveled a distance of x and λ is the attenuation length which is a characteristic value of the material propagating.

When the total length of the plastic scintillator is L_0 and the length from the light source to one of PMT's as L_1, the intensities at both ends are $H(L_1)$ and $H(-L_1)$, respectively. Geometrical average ΔE of the light intensity of from PMT's on both sides can be defined as

$$\begin{aligned} \Delta E &= \sqrt{H_0\exp(-L_1/\lambda)\cdot H_0\exp(-(L_0-L_1)/\lambda)} && (4.14)\\ &= H_0\sqrt{exp(-L_0/\lambda)} && (4.15)\\ &= H_0\exp\left(-L_0/2\lambda\right). && (4.16) \end{aligned}$$

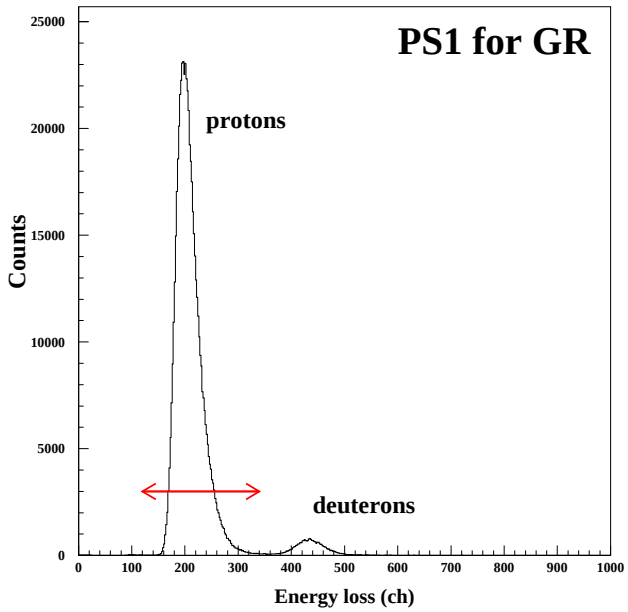

Figure 4.1: Energy loss spectrum at the PS1 of the GR. In the analysis for the measurements with the GR, the events corresponding to protons are obtained by putting a gate between 120 and 340 channels.

Therefore, the ΔE is independent on the scintillation position L_1 and proportional to initial intensity H_0. Since the energy loss of the charged particles in the scintillator material is described by the well-known Bethe-Bloch formula, the ΔE spectra are useful for the particle identification as shown in Fig. 4.1. In this figure, the scintillator is the front plane scintillator of GR and the events in the channel region from 120 to 340 channels were selected as protons.

4.4 Multi-wire Drift Chambers

Two MWDCs were used to determine the positions and the angles of particle trajectories in horizontal and vertical focal planes of the Grand Raiden spectrometer. Figure 4.2 shows the geometry of one MWDC and a particle passing through it. The electrons produced by the ionization of the counting gas along the trajectory drift toward the sense wires by the distances d_i. The drift time was measured as the time difference

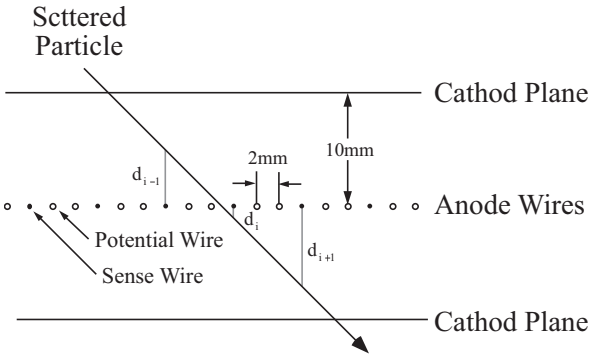

Figure 4.2: Geometry of the MWDCs. The figure shows the case of an event in which 3 wires were fired.

between the signal from the anode wire and that from the scintillator. Due to the non-uniformity of the electric field near the anode wires, the drift velocity is not a constant but depends on the distance d.

Figure 4.2 shows an event where 3 adjacent sense wires were fired. Depending on the angle of the track through the wire chamber, one particle generally fired adjacent n- wires. In this experiment we analyzed events with n- wire hits in each plane where $n = 1 \cdots 10$. The drift distances d and the positions of the wires hit were used to reconstruct the precise position of the track in the wire plane.

This method did not set very strict conditions in reconstructing trajectories. The cross-checking was performed by another procedure. We used the events with only one group of adjacent wires hit in each plane restricting the drift distance in the group to have only one minimum.

4.5 Detected Efficiency

As described in Sec. 3.5, we used two kinds of detectors, plastic scintillators and VDCs. The detection efficiencies of all VDCs are estimated assuming that the efficiencies of plastic scintillators are 100%. The position spectrum obtained by a plastic scintillator, which is given by left-right time differences, is shown in Fig. 4.3. Ideally, if a charged

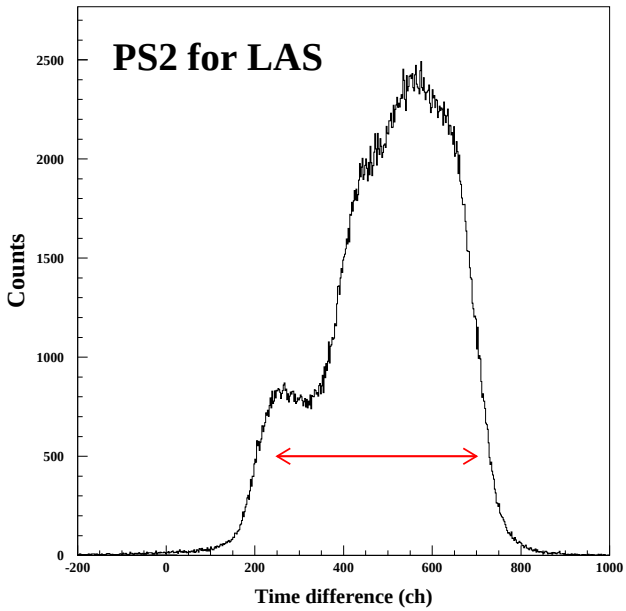

Figure 4.3: Time difference spectrum of the scintillator PS2 which are middle row of the front plane scintillators of LAS. The red arrow region is using to gate events for estimation of the MWDC efficiency.

particle passes, both the scintillator and the VDC give meaningful signals. Actually, however, there are the cases that some VDCs give no signal though scintillators give. By comparing the integrated numbers of events observed by scintillators with either the conditions that a VDC also gives signals or does not give, the efficiency of the VDC can be estimated. The typical efficiencies were estimated to be 92% and 80% for total MVDC's of GR and LAS, respectively.

4.6 Background Subtraction

The beam from the cyclotron has a bunch structure with almost 60 nsec periods for beam energy 392 MeV. A TDC spectrum for the time difference between the trigger signals of GR and LAS is shown in Fig. 4.4. Each peak corresponds to one beam bunch. The prompt peak includes the events that independent single events of GR and LAS coincidence accidentally. Such events called "chance" or "accidental" coincident events

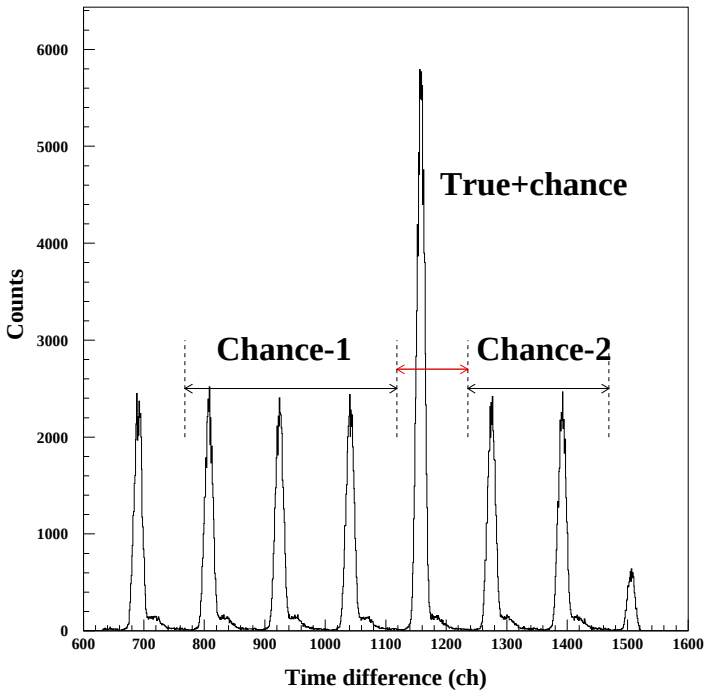

Figure 4.4: Time difference between trigger signals from GR and LAS. The prompt peak includes both of true and accidental coincidence events though others only include the accidental events. for the reaction ^{40}Ca(p,2p)^{39}K.

due to inelastic scattering are also detected. In Fig. 4.4, a prompt peak includes both the true and accidental coincidence events, while other peaks only include the accidental coincidence events As accidental events occur in randomly, the amount of accidental events contained in the highest peak is expected to be the same with a number of coincident events with a different beam bunch and can be estimated from those in other peaks. In order not to worsen statistical error as possible, one fifth of accumulated number of five smaller peaks is considered as the number of accidental events and then it is subtracted from the most highest peak. The spectrum of separation energy before and after background subtraction by this method is represented in Fig. 4.6 The left panel in this figure shows the spectrum before background subtraction with the spectrum for accidental events. The right panel also shows that this experiment performed with low background condition.

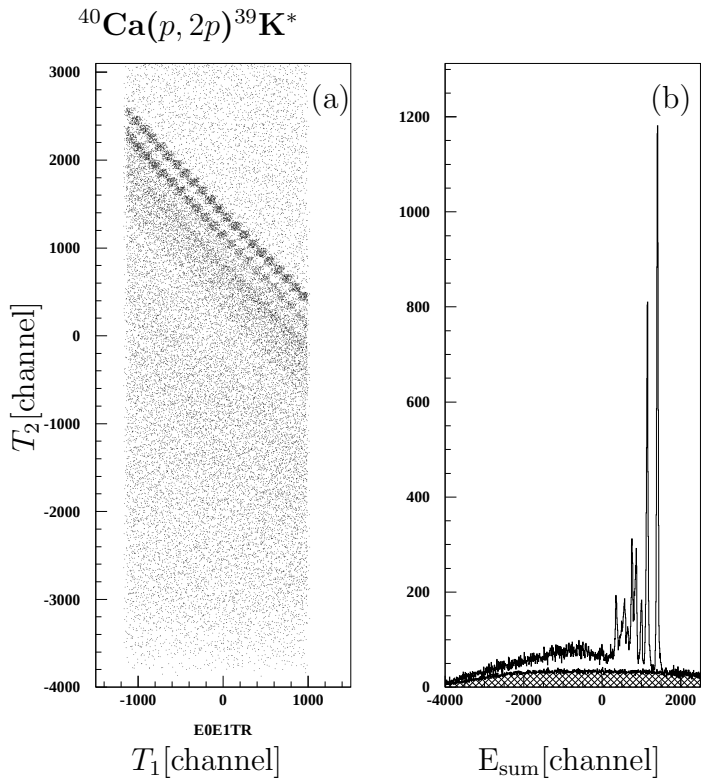

Figure 4.5: (a) Two-dimensional scatter plot of the energies, T_1(GR) and T_2(LAS), of coincidence two protons measured with GR and LAS in ^{40}Ca$(p, 2p)$ reactions. The locus lines correspond to the states of ^{39}K. (b) Summed energy spectrum of T_1 and T_2, which corresponded to separation energy spectrum of ^{40}Ca$(p, 2p)$ reactions. The hatched region is background of accidental coincidence events.

4.7 Experimental Result

4.7.1 Energy Spectra

Figure 4.5 shows a typical two–dimensional plot of yields as a function of T_1(GR) and T_2(LAS). Each locus corresponds to a final discrete state of the residual nucleus where the separation energy $E_{\rm sep}$ is kept constant. In Figs. 4.6 – 4.8, typical separation-energy spectra for ^{nat}Ca,^{nat}C and ^{6}Li targets are shown. The energy resolution of a FWHM was about 350(500) keV. In this article, we analyze well-separated peaks in the separation-energy spectra, namely $3/2^+$ and $1/2^+$ states of residual ^{39}K nucleus, $3/2^-$ and $1/2^+$ states of ^{11}B, and two levels of ^{5}He. In the case of $1/2^+$ peak for ^{39}K, an adjacent $7/2^-$ state is not separated but contributions from this level are estimated to be negligibly

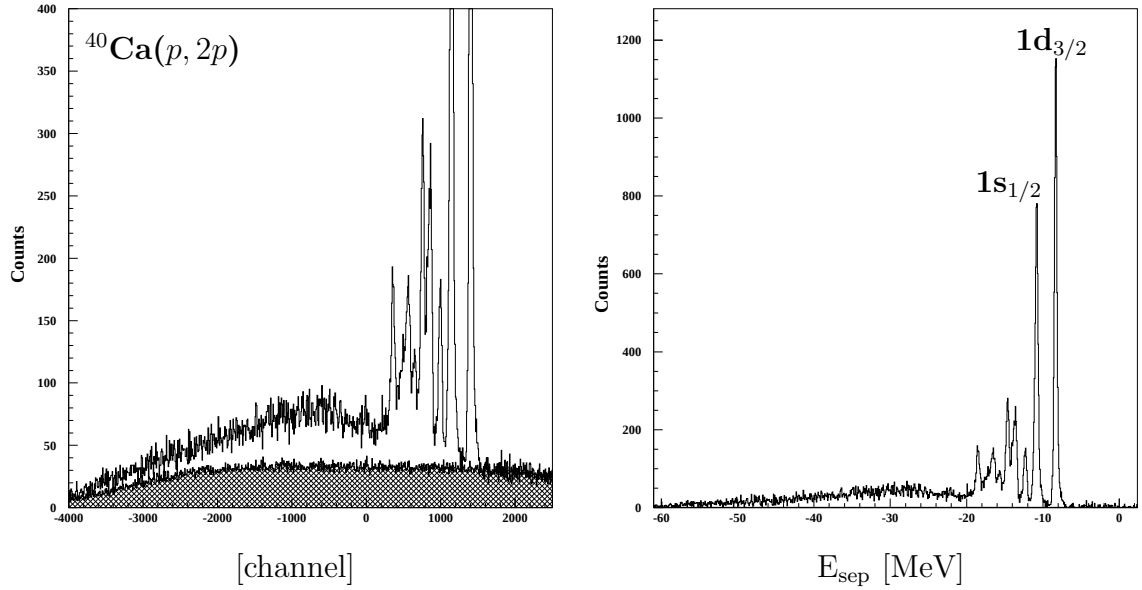

Figure 4.6: The separation energy spectrum for the reaction ^{40}Ca(p,2p)^{39}K.

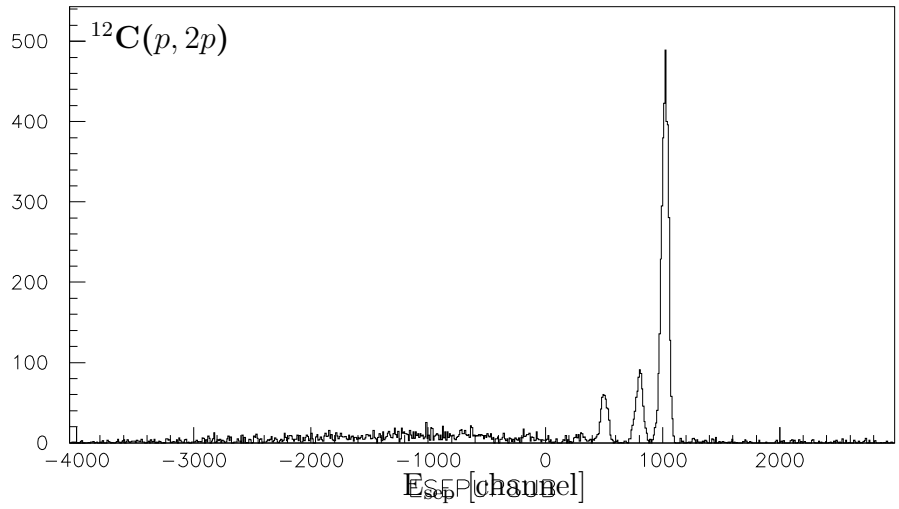

Figure 4.7: The separation energy spectrum for the reaction ^{12}C(p,2p)^{11}B.

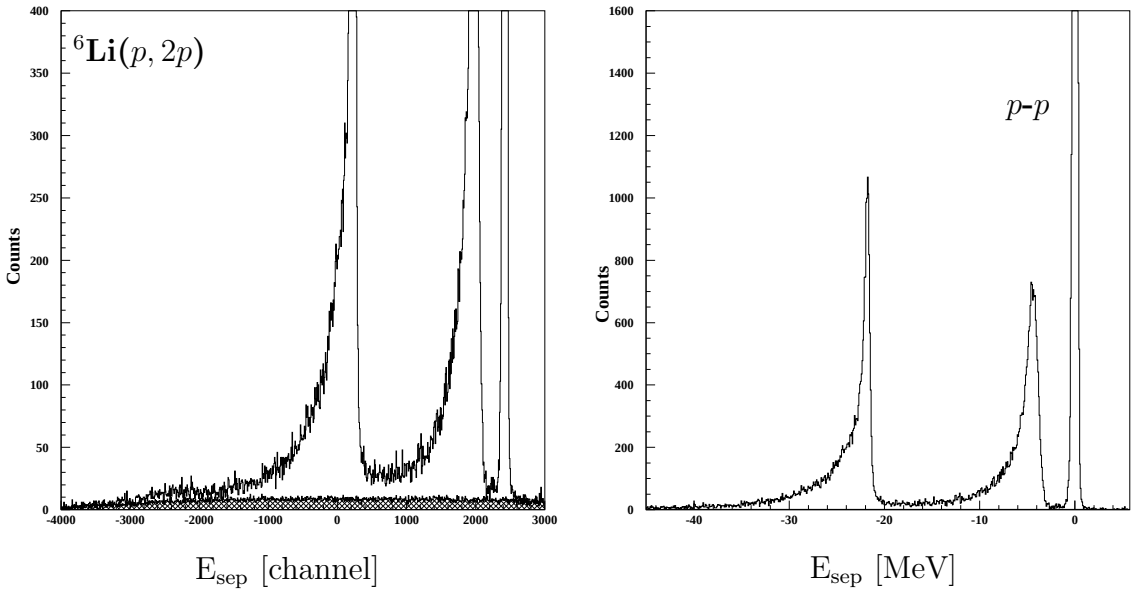

Figure 4.8: The separation energy spectrum for the reaction ^{6}Li(p,2p)^{5}He.

small using a DWIA calculation with a known spectroscopic factor.

4.7.2 Experimental Result

All of the data, differential cross-sections and analyzing powers are listed in App. A, as well as the setting conditions discussed above. Histogram plots of these data are given in Figs. 4.9 –4.11. In each figure, the horizontal axis is taken as the setting angle of LAS and the scale of the recoil momentum $\boldsymbol{k}_3$, which corresponds to the Fermi-motion momentum of the nucleon to be knocked out, is given on the top of the figure. The error bars listed and plotted are statistic ones. The overall errors of absolute cross-sections were about 6% mainly caused by uncertainties in target thicknesses and integral values of beam-current integration. And the overall errors of Ay's were about 2% canceled by an asymmetry measurement.

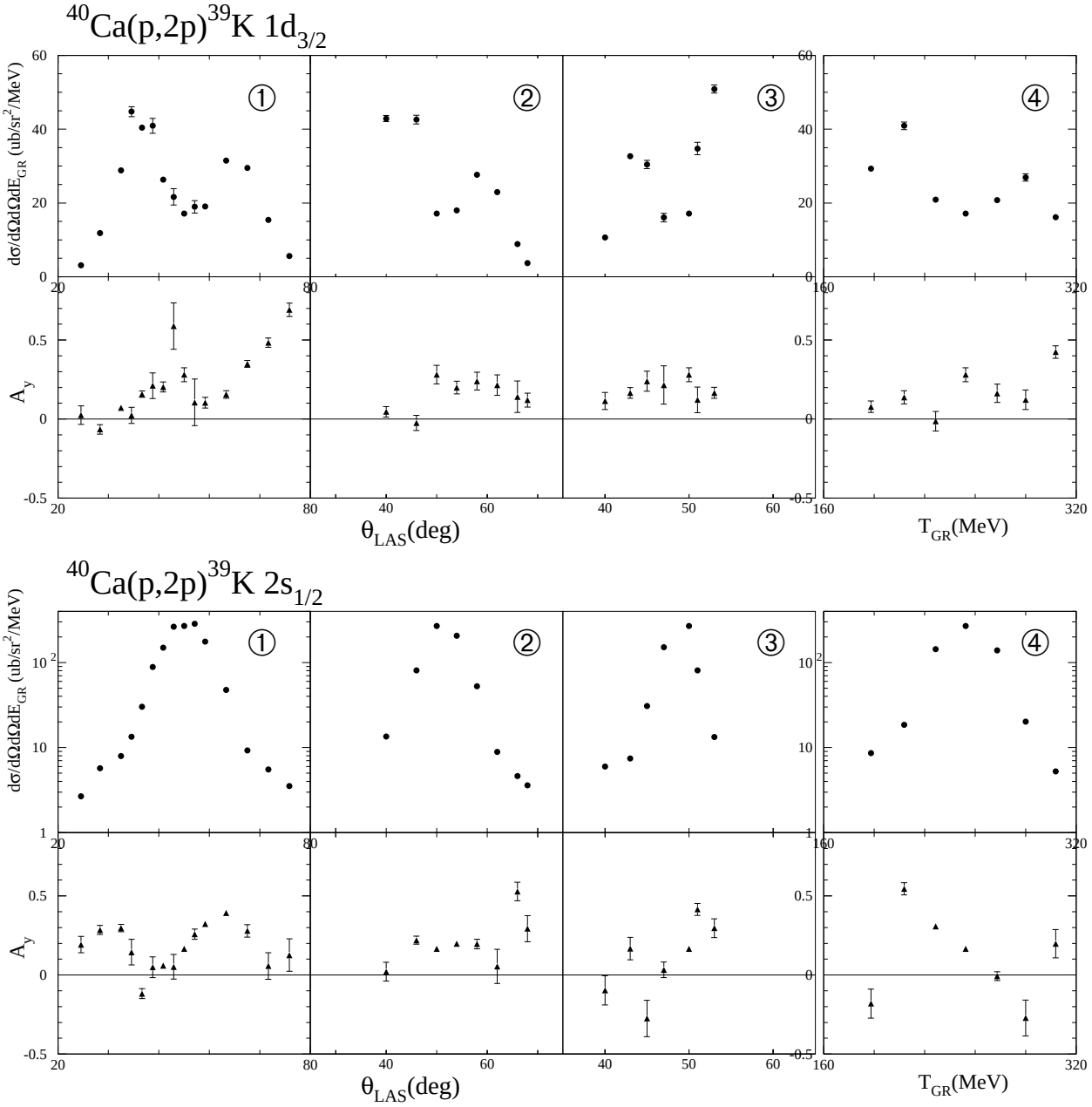

Figure 4.9: The differential cross sections and analyzing powers for $^{40}\mathrm{Ca}(p, 2p)$ reaction leading to the $1d_{3/2}$- and $2s_{1/2}$-hole states. The measurement was performed for four kinds of kinematical conditions indicated by encircled numbers. See the text for the details of the kinematics.

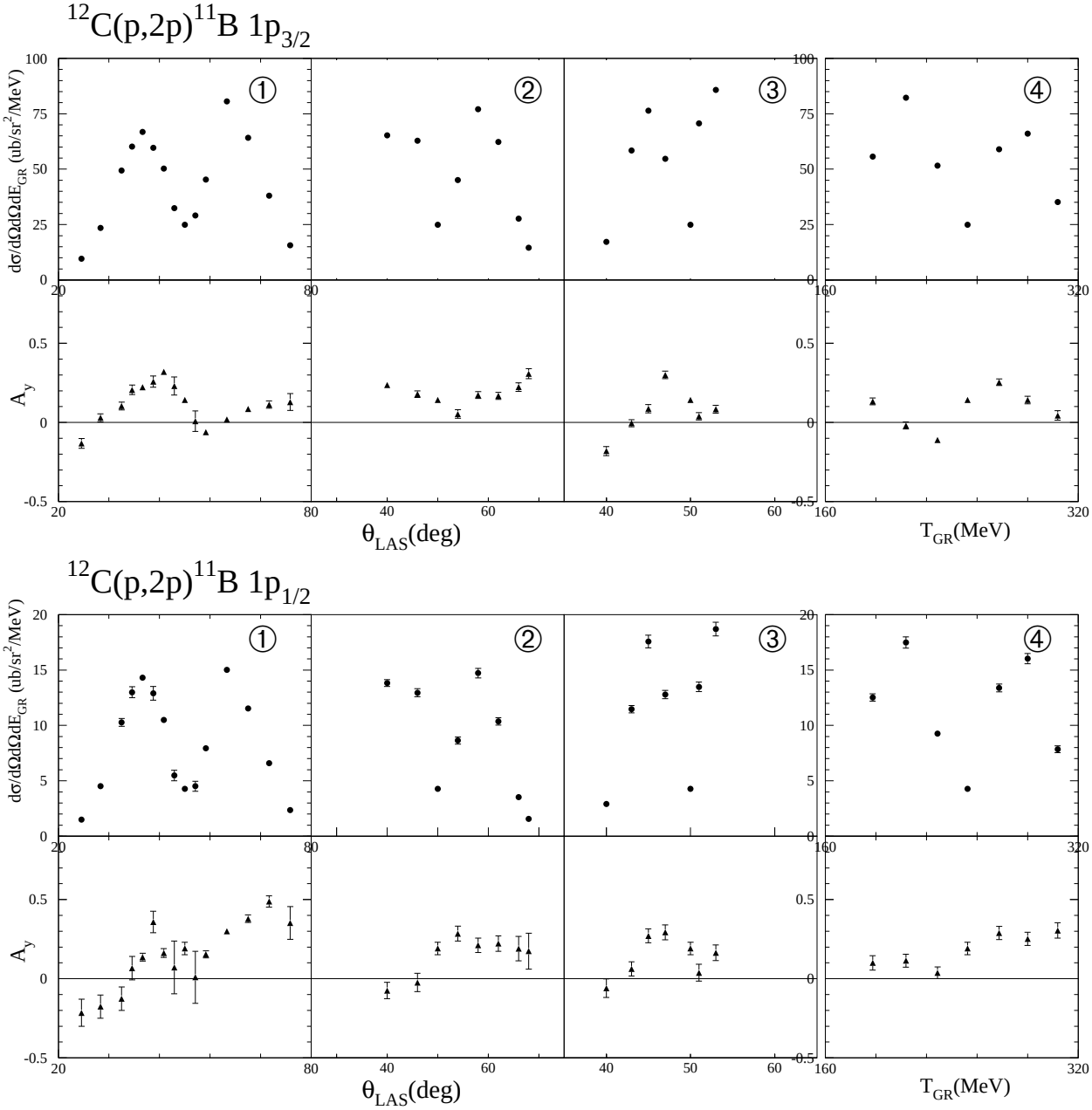

Figure 4.10: Experimental data for for ^{12}C$(p, 2p)$ reactions leading to the $1p_{3/2}$- and $1p_{1/2}$-hole states. The measurement was performed for four kinds of kinematical conditions indicated by encircled numbers. See the text for the details of the kinematics.

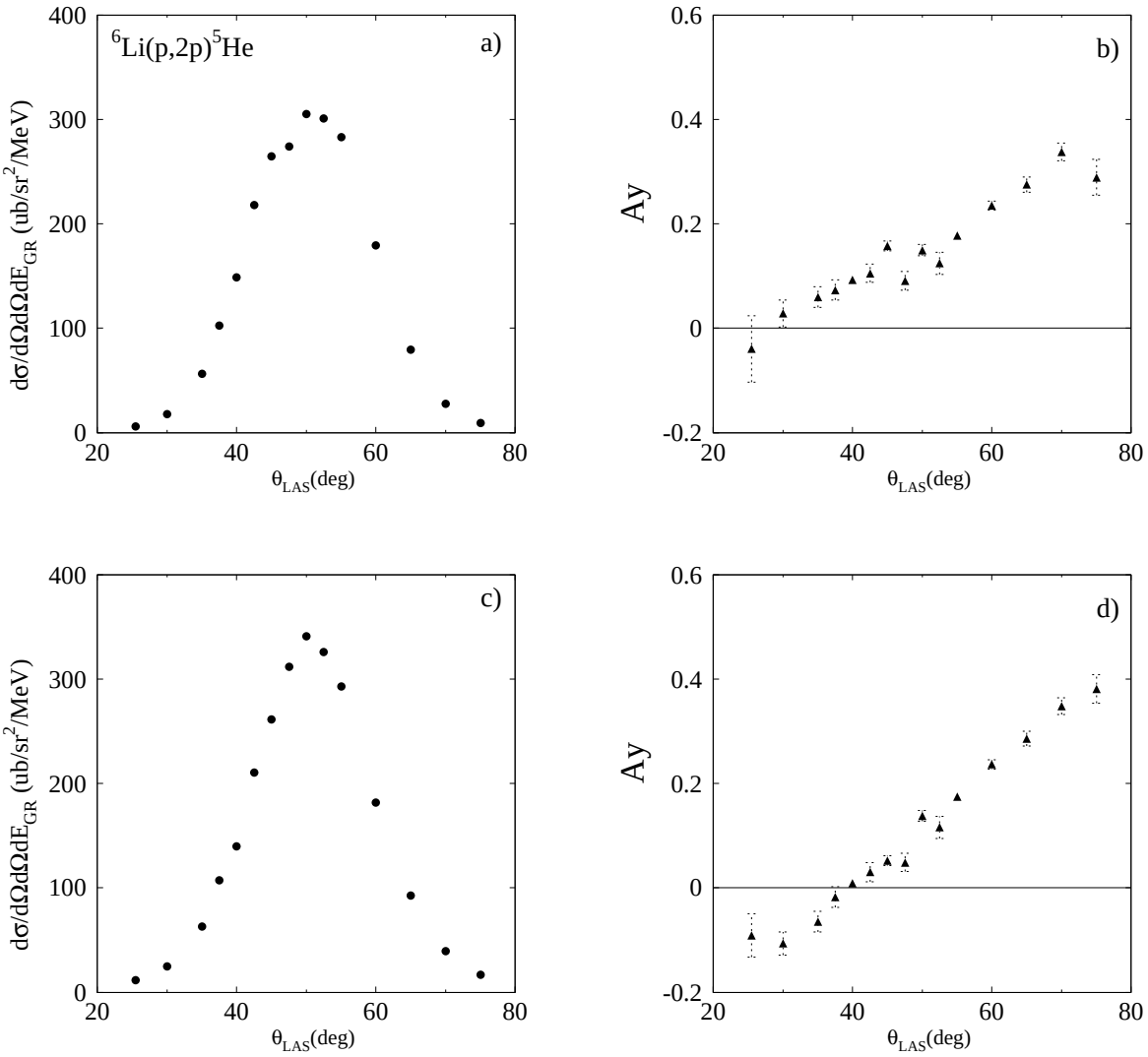

Figure 4.11: Triple differential cross section for $1p_{3/2}$ $1s_{1/2}$ knock-out ^{6}Li(p,2p) reaction at E_p=392 MeV.

Chapter 5

Comparisons with Theoretical Calculations

In this chapter, first the theoretical calculation formulations is presented. Next, the experimental results for three target nuclei are compared with theoretical calculations and, the S-factors and j-dependences are discussed.

5.1 Theoretical Calculations

The Distorted Wave Impulse Approximation (DWIA) has been used to describe the quasi-free knockout reactions at intermediate energies. In this work, theoretical calculations were performed by using a DWIA code THREEDEE, programmed by Chant and Roos [57, 58], in which a factorized approximations is employed. In the following, a theoretical framework used in the code is briefly described.

5.1.1 Kinematics of Quasi-free Knockout

We consider a quasi-free knockout reaction with the kinematics in the laboratory shown in Fig. 5.1. Here some symbols are different from those used in Sec. 3.2. The reaction is represented by $A(a, cd)B$ where $A = b + B$ namely, it is assumed that the two body elementary process is assumed to be $b(a, c)d$. In the case of $(p, 2p)$ reaction, both of a and b, accordingly c and d are protons. The four momenta of the projectile proton a and

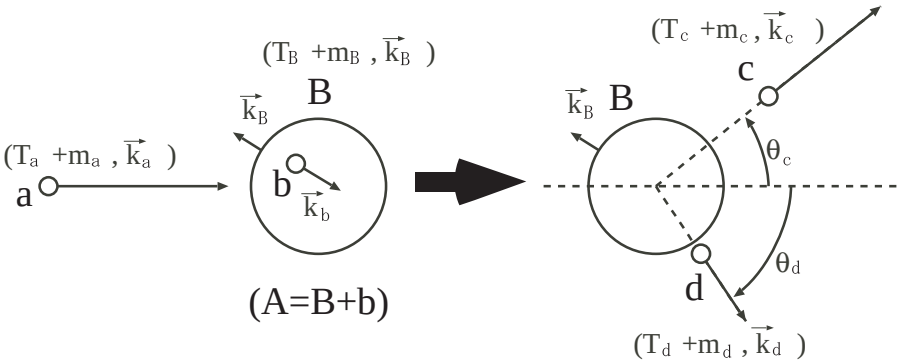

Figure 5.1: $(p, 2p)$ reaction in the laboratory coordinate system. Four-momenta are indicated as $(T_i{+}m_i\ ,\ \boldsymbol{k}_i)$ for incident (i=a,b,c,d,B) and two outgoing(i=c,d) protons, respectively. (notation wrong) $\boldsymbol{k}_B$ is called the recoil momentum.

the target nucleus A in the initial state, outgoing two protons c, d and the residual target B in the final state are $(T_a + m_a, \boldsymbol{k}_a)$, $(T_A + m_A, \boldsymbol{k}_A)$, $(T_c + m_c, \boldsymbol{k}_c)$, $(T_d + m_d, \boldsymbol{k}_d)$ and $(T_B + m_B, \boldsymbol{k}_B)$, respectively.

Because the target nucleus A is stationary in the laboratory system, energy and momentum conservation requires that

$$(T_a + m_a) + m_A = (T_c + m_c) + (T_d + m_d) + (T_B + m_B) + Q + E_x \tag{5.1}$$

$$\boldsymbol{k}_a = \boldsymbol{k}_c + \boldsymbol{k}_d + \boldsymbol{k}_B, \tag{5.2}$$

where Q is the Q-value of the reaction and E_x is the excitation energy of the residual nucleus B.

5.1.2 The DWIA

The differential cross section for the knockout reaction $A(a, cd)B$ is given by

$$\sigma_{fi} = \frac{2\pi\omega_f}{v} |T_{fi}| \tag{5.3}$$

where v is the relative velocity of a and A in the initial channel and ω_f is the energy density of final states. The transition amplitude $|T_{fi}|$ is given by

$$T_{fi} = \langle \Phi^{(-)}(B,c,d) \left| \hat{V} \right| \Psi^{(+)}(A,a) \rangle \tag{5.4}$$

where $\Psi^{(+)}$ is the exact wave function for the system and $\Phi^{(-)}$ is the solution (with ingoing wave boundary conditions) obtained. The unpolarized differential cross section of quasi-free knockout reaction is given by

$$\frac{d^3\sigma}{d\Omega_c d\Omega_d dE_c} = \frac{F_{kin}}{(2s_a+1)(2J_A+1)} \sum_{\mu_a,\mu_c,\mu_d,M_A,M_B} |T_{fi}|^2, \tag{5.5}$$

$$A_y = \frac{Tr(T_{fi}\hat{\sigma}_{ay}T_{fi}^{\dagger})}{Tr(T_{fi}T_{fi}^{\dagger})}. \tag{5.6}$$

where F_{kin} is a kinematic factor, μ_i is the projection quantum number of spin s_i for particle $i\,(i = a,c,d)$ and J_j is the total angular momentum quantum number of nucleus $j\,(j = A,B)$ with corresponding projection quantum number M_j, and $\hat{\sigma}_{ay}$ is the y-component of Pauli spin operator acting on the incident proton. Defining the transition operator $\hat{t}$ as

$$\hat{V}|\Psi^{(+)}(A,a)\rangle = \hat{t}|\Phi^{(+)}(A,a)\rangle, \tag{5.7}$$

the transition amplitude can be written as

$$T_{fi} = \langle \Phi^{(-)}(B,c,d) \left| \hat{t} \right| \Phi^{(+)}(A,a) \rangle \tag{5.8}$$

$$= n_A^{-1/2} C \sum_{LJM} \theta_{LJ}(B,b|A) \langle J_B M_B JM | J_A M_A \rangle T_{LJM}, \tag{5.9}$$

with T_{LJM} given by [59]

$$T_{LJM}(\mu_a,\mu_c,\mu_d) = \int\int d\vec{r}d\vec{r}' [\chi^{*(-)}_{\mu_c}(\vec{k}_{cB},\vec{r})\chi^{*(-)}_{\mu_d}(\vec{k}_{dB},\vec{r}')(1-\hat{P^{\dagger}_{ex}})t_{NN}(|\vec{r}-\vec{r}'|) \times \chi^{(+)}_{\mu_a}(\vec{k}_{aA},\vec{r})\phi^B_{LJM}(\vec{r}'), \tag{5.10}$$

where $C = \langle t_b \nu_b T_B N_B | T_A N_A \rangle$ is a Clebsch Gordan coefficient for isospin and the quantities T_j and N_j are the isospin and isospin projection quantum numbers for $j = A,B$. The quantum numbers L, J and M are the orbital angular momentum, the total angular momentum and the projection of the total angular momentum of the bound nucleon,

respectively. The quantity n_A is mass number of nucleus A. The coefficient $\theta_{LJ}(B,b|A)$ is the fractional parentage coefficient described the decomposition of the target nucleus $A \rightarrow B + b$. For the target nucleus and the bound state with the specified values of L and J, the unpolarized differential cross section is written as

$$\frac{d^3\sigma^{LJ}}{d\Omega_c d\Omega_d dE_c} = \frac{F_{kin} S_{LJ}}{(2s_a+1)(2J_A+1)} \tag{5.11}$$

$$\times \sum_{s_a,s_c,s_d,M} \left| \sum_{\Lambda} \langle L\Lambda s_d \mu_d | JM \rangle T_{LJM}(\mu_a, \mu_c, \mu_d) \right|^2 \tag{5.12}$$

where the quantity $S_{LJ} = |C\theta_{LJ}(B,b|A)|^2 = |\langle t_b \nu_b T_b N_b | T_A N_A \rangle \theta_{LJ}(B,b|A)|^2$ is the spectroscopic factor and Λ is the projection quantum number of L. The differential cross section for an incident beam of spin-up or spin-down polarized protons whose spin are $1/2$ is

$$\sigma^{\uparrow(\downarrow)} \equiv \frac{d^3\sigma^{\uparrow(\downarrow)}}{d\Omega_c d\Omega_d dE_c} \tag{5.13}$$

$$= \frac{F_{kin}}{(2s_a+1)(2J_A+1)} \sum_{\mu_a,\mu_c,\mu_d,M} \left| \sum_{\Lambda} \langle L\Lambda \frac{1}{2} \mu_d | JM \rangle T^{\uparrow(\downarrow)}_{LJM} \right|^2 \tag{5.14}$$

$$\tag{5.15}$$

and the analyzing power A_y is defined by

$$A_y = \frac{1}{p} \frac{\sigma^{\uparrow} - \sigma^{\downarrow}}{\sigma^{\uparrow} + \sigma^{\downarrow}}. \tag{5.16}$$

$$\tag{5.17}$$

where p is the polarization of the incident proton beam.

5.1.3 The Factorized DWIA

As mentioned above, the calculation code used for this work is THREEDEE [58] where the factorized DWIA is applied. From the general form of the DWIA, the expression is transformed into a factorized formula. It is advantage not only to calculate effectively also to extract the significance of physics. The framework of the DWIA is non-relativistic but the kinematics is treated relativistically.

The transition amplitude in the factorized DWIA can be written as

$$T_{fi} = n_A^{-1/2} C \sum_{LJM} \theta_{LJ}(B,b|A) \langle J_B M_B JM | J_A M_A \rangle \langle \vec{k_f} \mu_c \mu_d | \hat{t}_{NN} | \mu_a \mu_b \vec{k_i} \rangle T^{fac}_{LJM}(\mu_a, \mu_c, \mu_d) \tag{5.18}$$

where $\vec{k_i}$ and $\vec{k_f}$ are the initial and final relative momenta of two interacting particles and $\langle \vec{k_f} \mu_c \mu_d | \hat{t}_{NN} | \mu_a \mu_b \vec{k_i} \rangle$ is the anti-symmetrized nucleon-nucleon(NN) scattering amplitude. $T^{fac}_{LJM}(\mu_a, \mu_c, \mu_d)$, which is called as the distorted momentum distribution, is given by

$$T^{fac}_{LJM}(\mu_a, \mu_c, \mu_d) = \int d\vec{r} \chi^{*(-)}_{\mu_c}(\vec{k}_{cB}, \vec{r}) \chi^{*(-)}_{\mu_d}(\vec{k}_{dB}, \vec{r}) \chi^{(+)}_{\mu_a}(\vec{k}_{aA}, \frac{B}{A}\vec{r}) \phi^B_{LJM}(\vec{r}), \tag{5.19}$$

where $\chi^{*(\pm)}_i$ are the distorted waves in spin space, $\phi^B_{LJM}(\vec{r})$ is the bound-state wave function for $b + B$. The t-matrix is replaced by a two-body t-matrix evaluated at asymptotic kinematics.

5.1.4 Parameters for DWIA

For calculations using THREEDEE, we used the following input parameters.

Optical Potential

For optical potentials of incident and outgoing protons, two types of potentials were used in calculations. One was known as Global potentials and another way was calculations in the framework of the relativistic impulse approximation (RIA) using bound state wave functions based on the relativistic Hartree approximation.

OPT1: Global Potentials

We used the global Dirac optical potentials phenomenologically determined by Cooper *et al.* [60] to fit elastic scattering data in an intermediate energy of 20∼1050 MeV. These global potentials were applied to ^{40}Ca and ^{12}C targets but not to ^{6}Li target because this global potential parameter set is not applicable for such a light nucleus less than a mass number of 12.

Table 5.1: Scaler meson mass and R.M.S. radius for TIMORA

Nuclide	M_{sm}(MeV)	r_{RMS}(fm)	r_{ch}[1](fm)	$r_{density}$[2](fm)
^{5}He	520	2.046		
^{6}Li	516.3	2.429	2.56(5)	2.43
^{11}B	518.5	2.283	2.42(12)	2.28
^{12}C	517.5	2.314	2.47(16)	2.34
^{39}K	520	3.347	3.408(27)	3.31
^{40}Ca	520	3.389	3.479(3)	3.39

1) r_{ch}: R.M.S. of charge distribution in Ref. [62]
2) radius $r_{density} = \sqrt{< r_{ch} >^2 - < r_{ch:p} >^2}$: R.M.S. of proton distribution
$< r_{ch:p} >$ =0.80 fm: R.M.S. of single proton charge distribution

OPT2: Potentials in the framework of RIA

In the framework of the relativistic impulse approximation (RIA), to optical potentials are calculated using a Horowitz's code [63] in the following procedure:

- The density distributions of the target and the residual nuclei are calculated in a frame work the Dirac-Hartree approximation by using the computer code TIMORA [61]. The scalar meson mass, an input parameter for the code, optimized in order to reproduce the charge radius deduced from electron scattering for each target. These parameter and R.M.S. radii are shown in Table 5.1.
- By folding these nuclear densities with the nucleon-nucleon interaction, that is the Horowitz-Love-Franey Interaction, the relativistic scalar and vector optical potential are obtained using the code FOLDER [61].
- Schrödinger equivalent optical potentials are deduced from these relativistic scaler and vector potentials.

By this method, a proton optical potential can be obtained for any target nucleus at an arbitrary energy. Then, for a $A(a, cd)B$ reaction, we can obtain optical potentials which determine the scattering wave functions for $a+A$, $c+B$ and $d+B$ systems.

The Bound State Wave Function

For bound state wave functions, two types were used in the calculations. One was calculations from a phenomenological potential, which type is the Wood-Saxon well, and another was a self consistent method based on the relativistic Hartree model.

WFN1: Well Depth method

The wave function of the bound proton was generated in a standard way, called the well depth method, where the depth of the Woods-Saxon well was adjusted to reproduce the proton binding energy. In the present study, because the absolute values of S-factors are discussed and compared with results of $(e, e'p)$ reactions, the same geometrical parameters of the Woods-Saxon potential as those deduced from $(e, e'p)$ reactions, which are consistent with or electron scattering data. In Table 5.2, the radius parameter r_0, diffuseness parameter a_0 and calculated results of the potential depth V_0 and the proton root mean square radius r_{RMS} are shown.

WFN2: Potentials in the framework of Dirac-Hartree

The bound state wave function of a proton is calculated from a relativistic mean field produced by the Dirac-Hartree model by using the computer code TIMORA[61] which is same code mentioned above for **POT2**. Since the coordinate system used in the code TIMORA is the center of mass system of the target nucleus A and the system used in the code THREEDEE is the relative coordinate system of b and B, a necessary transformation was made. Concerning the proton root mean square radius, the scalar meson mass were optimized as mentioned for optical potential **OPT2**. For the knockout reaction from $1p_{1/2}$ state of the ^{12}C target, this self consistent method was not applicable, because the code TIMORA give no solution for this state.

NN t-Matrix

In the calculation using THREEDEE, the NN t-matrix $\hat{t}_{NN}$ was taken from the WI99 solution of the phase shift analysis by Arndt *et al.* [64] This NN t-matrix is based on

Table 5.2: Well parameters for bound state

Nuclide	state	V_0(MeV)	r_0(fm)	a_0(fm)	r_{RMS}(fm)
^{40}Ca	$1d_{3/2}$				
	NON-L	50.83	1.30	0.65	3.73
	LOCAL	50.83	1.30	0.65	3.63
($(e,e'p)$ [69]		51.6	1.30	0.65	3.69)
^{40}Ca	$2s_{1/2}$				
	NON-L	55.27	1.30	0.65	3.75
	LOCAL	55.27	1.30	0.65	3.57
($(e,e'p)$ [69]		55.5	1.30	0.65	3.72)
^{12}C	$1p_{3/2}$				
	NON-L	58.43	1.35	0.65	2.80
	LOCAL	58.43	1.35	0.65	2.69
($(e,e'p)$ [70]			1.35	0.65	2.78)
^{12}C	$1p_{1/2}$				
	NON-L	52.98	1.65	0.65	2.97
	LOCAL	52.98	1.65	0.65	2.88
($(e,e'p)$ [70]			1.65	0.65	2.95)

NON-L : with non-locality correction

LOCAL : without non-locality correction

Spin-orbit potential V_{so}= 6 MeV for all states

Non-locality correction : Perey factor β=0.85 fm

Coulomb radius r_c=1.30 fm for ^{40}Ca [69] and r_c=1.20 fm for ^{12}C [70]

the NN scattering in free space, namely on energy shell. But, Actually, the quasi-free knockout reaction is off energy shell reaction because of spending knockout energy and the final energy is different from the initial energy in the two-body kinematics. In the present calculation, the NN t-matrix in the final energy prescription (FEP) was used.

Non-locality

DWIA calculations were performed with and without non-locality correction. Non-locality correction was applied to both the scattering and bound state wave functions by multiplying Perey factors with a range parameter, $\beta = 0.85$ fm [65] Non-locality effects

caused significantly different results for absolute values of differential cross sections but the momentum distributions of differential cross sections and analyzing powers were not practically affected by this correction.

5.2 Calculations for the Comparison

After this section, the differential cross sections and analyzing powers A_y's for ^{40}Ca,^{12}C and ^{6}Li targets are plotted as functions of the recoil momenta $\boldsymbol{k}_3$, which corresponds to the Fermi-motion momentum of the protons to be knocked out in the target nucleus. And the results of the plane wave impulse approximation (PWIA) which is one of outputs from the code THREEDEE are plotted with experimental results, as well. In the PWIA, with an assumption that the wave functions are not distorted by the target nucleus, the wave function represents the momentum distribution of the bound proton in the nucleus, namely the Fourier transform of the bound state wave function.

5.2.1 Notation of the Recoil Momentum $\boldsymbol{k}_3$

For the momentum distribution, we define the positive sign of the recoil momentum k_3 as the direction when the angle θ_{GR} is bigger than the zero recoil point ($\boldsymbol{k}_3$= $0MeV/c$) for the cases of kinematics ② and ③ In the case of ①, on the other hand, positive sign of k_3 is defined as the direction when the angle θ_{LAS} is bigger than the zero recoil point. For the case of kinematics ④ where two angles were fixed, positive sign of k_3 is means that the energy E_{GR} is bigger than that of the zero recoil point. All the experimental data, at the points corresponding to the recoil momenta calculated from the central values of angles and energies of the spectrometers. The finite acceptance effect are estimated by a Monte Carlo method and theoretical results are corrected.

5.2.2 Angular Momentum Dependence

Calculated results of cross sections for several knockout states from ^{40}Ca are shown in Fig. 5.2. The condition and parameters for these calculations are Global optical potential [**OPT1**] for scattering and the Wood-Saxon well [**WFN1**] for the bound state wave functions, and non-locality corrections are adopted. This figure shows that the difference in recoil momentum distributions between various states are easily distinguishable. This means that the momentum dependence reflects the characteristic of momentum-space wave function of each orbit. These feature is robust and is not sensitively depend on input parameters, like a radius of a optical potential, if the values are within appropriate ranges.

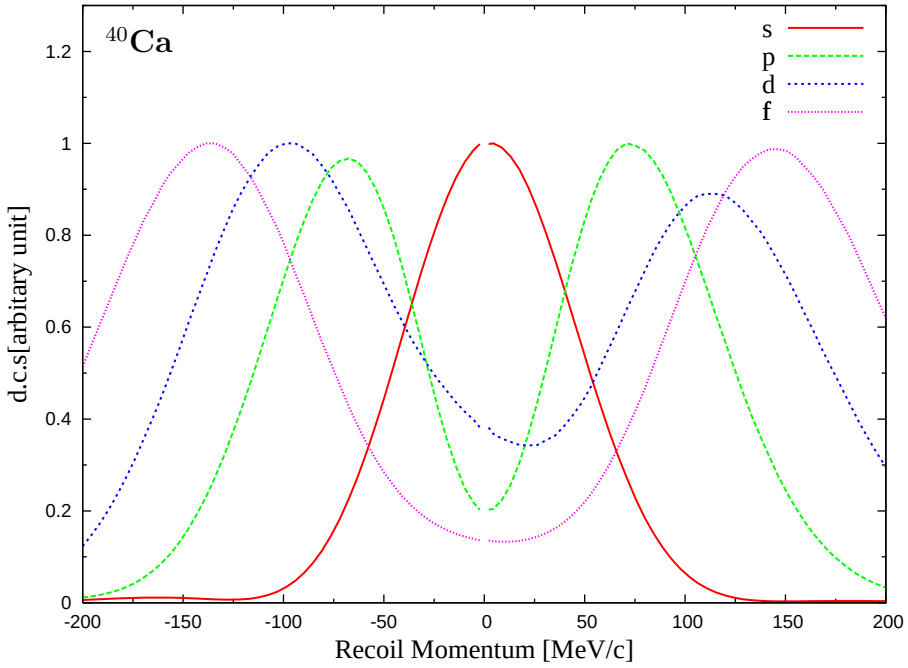

Figure 5.2: The recoil momentum distributions of differential cross sections for various L from ^{40}Ca$(\vec{p}, 2p)$. See the text for the theoretical lines. kinematics series- ①. For the vertical axis, the cross sections are normalized by maximum value of them.

5.2.3 Combination of Parameters

For comparisons with experimental results, three combinations of types for optical potentials in Sec. 5.1.4 and the bound state wave functions in Sec. 5.1.4 were calculated. One

of them uses Global optical potential [**OPT1**] and the Wood-Saxon potential [**WFN1**], and is called "GLOBAL" hereafter. Next one uses calculations by the RIA [**OPT2**] code TIMORA and FOLDER, and the Wood-Saxon potential [**WFN1**], and is called "FOLDER". The last uses calculations by the RIA code TIMORA for both of optical potential [**OPT2**] and the bound state wave function [**WFN2**], and is called "TIMORA". "GLOBAL" and "TIMORA" are entirely different in frameworks and the comparison of "GLOBAL" and "FOLDER" is focused on the effect of different optical potentials.

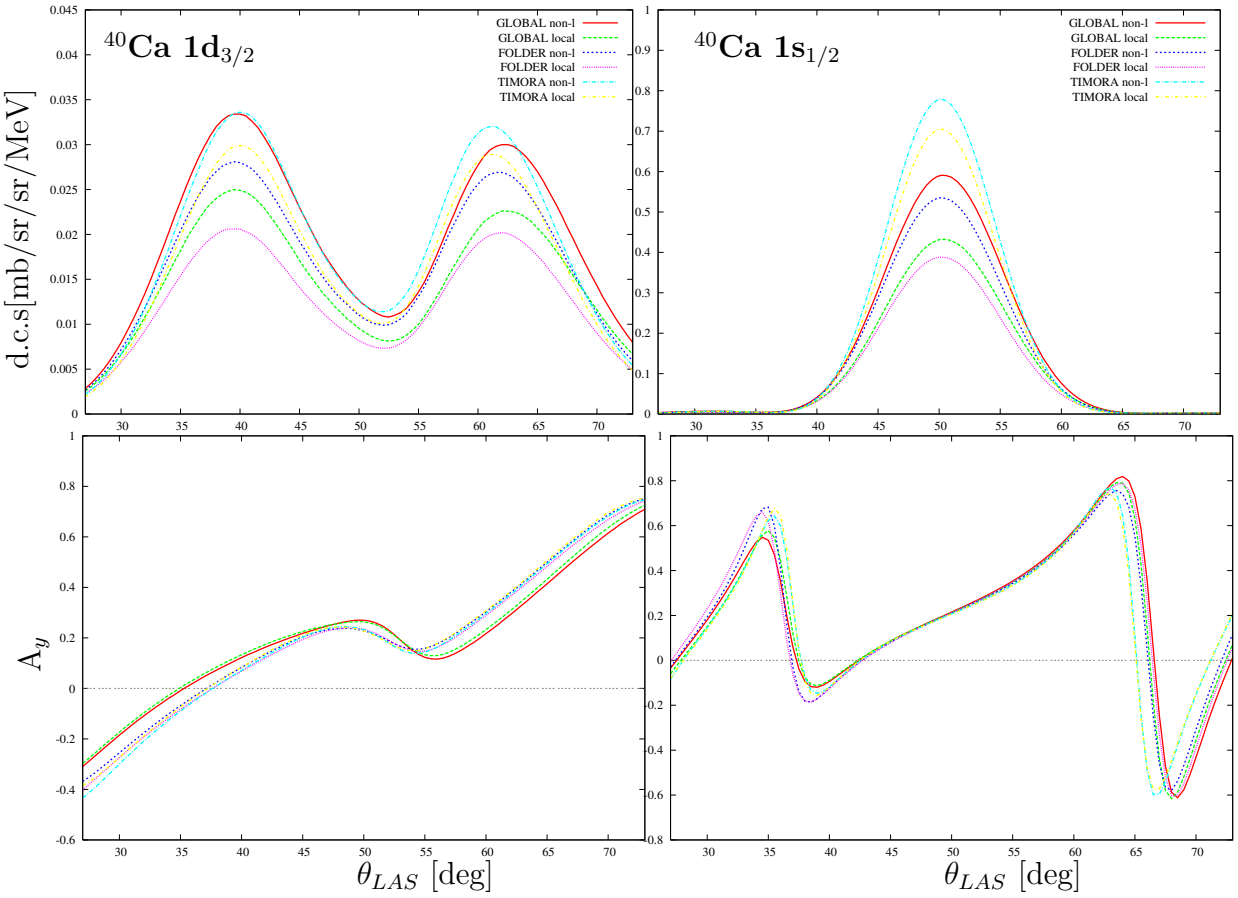

Figure 5.3: Comparison between calculations: The differential cross sections and analyzing powers for ^{40}Ca$(\vec{p}, 2p)$ in kinematics series-①.

In Fig. 5.3 and 5.4, the sample results of six types of calculations for these three combinations with and without non-locality correction are described for ^{40}Ca and ^{12}C targets, respectively. Though these results show that the absolute value of cross section depend on calculation parameters so much, all distributions both of cross section and

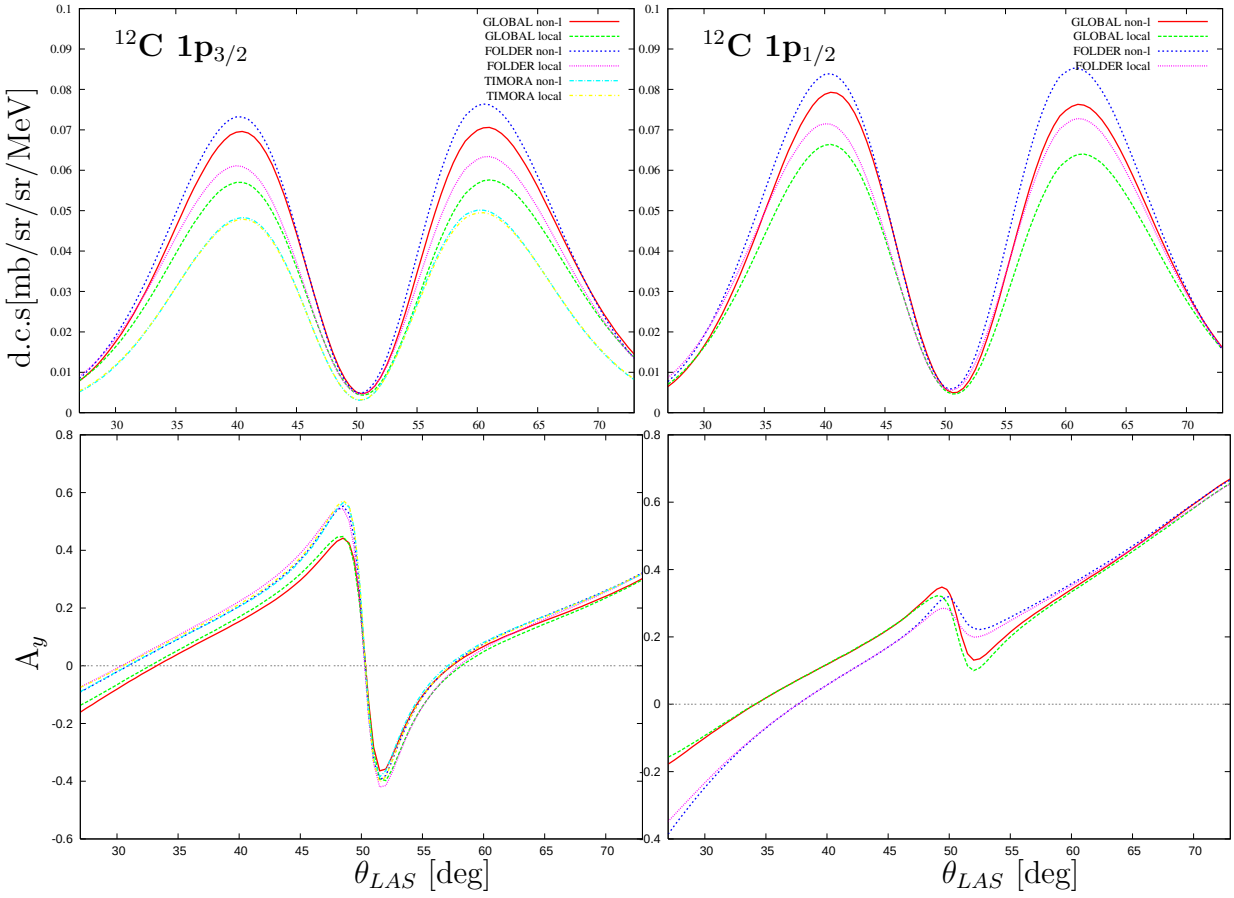

Figure 5.4: Comparison between calculations: The differential cross sections and analyzing powers for ^{12}C$(\vec{p}, 2p)$ in kinematics series-①.

analyzing power are quite similar.

5.2.4 Corrections for Finite Angles and Energies

For the comparison of the experimental data with the theoretical calculations, we performed the correction for finite angle and momentum bite with actual detectors. The code THREEDEE of the DWIA is calculated for an infinitesimal acceptance and a point energy at a time. But the each spectrometer has finite solid angle and momentum acceptance. Then, to compare the experimental data with the theoretical values, we calculated the theoretical values with the Monte-Carlo method using 500 calculation points for a single setting. For a THREEDEE calculation, we can set finite azimuthal angle only for particle d, of $A(a, cd)B$ reactions. Then, to simulate the condition when both of az-

imuthal angles,[3] ϕ_c and ϕ_d, are finite, we set the angle for d to be $\phi_c + \phi_d$, and calculated analyzing power was reduced by factor $cos\phi$.

As shown in the figure 5.5, the finite acceptance effect is significantly large only at around θ_{LAS}=50°, which corresponds th the zero-recoil condition.

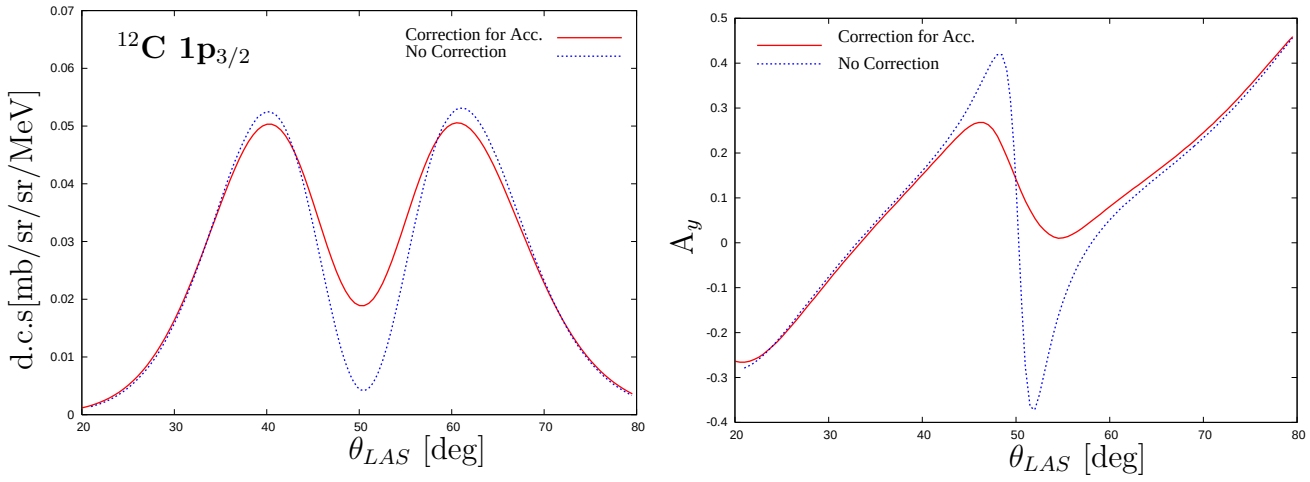

Figure 5.5: Finite acceptance effect for the differential cross section and A_y for ^{12}C$(\vec{p}, 2p)^{11}$B leading to 1p$_{3/2}$. The solid lines are calculated results including finite solid angles and finite momentum acceptance corrections. The dashed lines are calculation results without these corrections. Both of solid and dashed lines were calculated with the "GLOBAL" combination referred in Sec. 5.2.3 with non-locality correction.

[3]Here, ϕ's are defined as azimuthal angles around the incident beam axis,which is different from the definition used in THREEDEE.

5.3 Differential cross sections for ^{40}Ca and ^{12}C Targets

In this section, the recoil momentum distributions of differential cross section for ^{40}Ca and ^{12}C targets were compared with DWIA calculations. For each set of calculations, absolute value of the cross section is normalized to experimental data using a single normalization factor for all of four kinematics series concerning the same target and the same orbit.

5.3.1 ^{40}Ca$(\vec{p}, 2p)^{39}$K Reaction

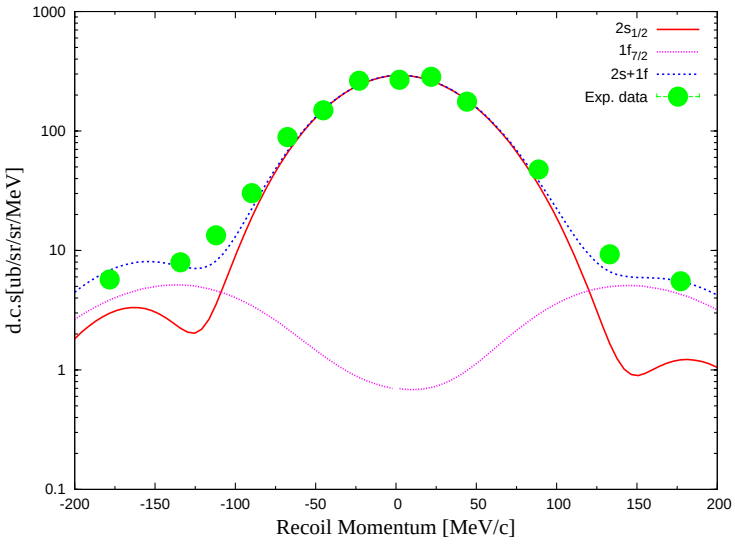

Figure 5.6: The distribution of differential cross sections for ^{40}Ca$(\vec{p}, 2p)$ reactions leading to the $2s_{1/2}$-hole state are compared with DWIA calculations assuming $2s_{1/2}$-hole and $1f_{7/2}$-hole states. This shows the influence of $1f_{7/2}$-hole state are less one percent near the maximum region.

For the $2s_{1/2}$ knockout reaction, whose separation energy is 10.9 MeV, this state is not separated from other $1f_{7/2}$ (E_{sep}=11.1 MeV) and $2p_{3/2}$ (E_{sep}=11.4 MeV) states, clearly. Then, experimental data are fitted as an incoherent sum of two kinds of knockout $2s_{1/2}$ and $1f_{7/2}$. The result is shown in Fig. 5.6 and it is found that the $1f_{7/2}$ contribution is less than 1% around the zero-recoil region. This is consistent with results derived from $(e, e'p)$

and (d,^{3}He) reactions. Since it is known from those reactions that the contribution from $2p_{3/2}$ states is much less than that from $1f_{7/2}$ state, we ignore such contribution here.

Figs. 5.7 and 5.8 show the recoil momentum $\boldsymbol{k}_3$ distributions of differential cross sections for $1d_{3/2}$-knockout and $2s_{1/2}$-knockout from the ^{40}Ca target, respectively. The calculation results from combinations "GLOBAL", "FOLDER" and "TIMORA" are plotted in the upper, middle and lower rows of figures, respectively. In these figures, dotted lines are the results of PWIA calculations, solid and dashed dotted lines are the results without non-locality correction for two different normalization factors determined from the left side peak and the right side peak and dashed lines are the results from each combination with non-locality correction. In these cases, normalization factors were roughly estimated and common values for whole four kinematic series.

In Fig. 5.8, there is the deviation from the data in the region of $|\boldsymbol{k}_3| > 120$MeV/c. This deviation is mainly caused by the mixture of contribution from $1f_{7/2}$ state as mentioned above. Except this minor yield region, the distributions of DWIA calculations for both states are well reproduced for all of the four kinematic series regardless of combinations of optical potentials and bound state wave functions. In the case of the series ④, although it seems that the ambiguity in selecting the optical potential might cause deviation from others, calculations are reproduced fairly well. On the other hand, the distributions of PWIA calculations are different from experimental results for peak positions.

5.3.2 ^{12}C$(\vec{p}, 2p)^{11}$B Reaction

The Fig. 5.9 and 5.10 show the results of $1p_{3/2}$- and $1p_{1/2}$-knockout from ^{12}C, respectively. For the $1p_{3/2}$-knockout, the calculated results for "GLOBAL", "FOLDER" and "TIMORA" are shown in these figure. For the $1p_{1/2}$-knockout, "TIMORA" calculations are missing because of the reason mentioned in Sec. 5.2.3 The lines of calculations in the figures are defined as same as in Sec. 5.3.1. For these ^{12}C$(\vec{p}, 2p)^{11}$B reaction, the distributions of PWIA calculations are not so different from experimental results and DWIA calculations. DWIA calculations give good prediction for distributions of cross sections

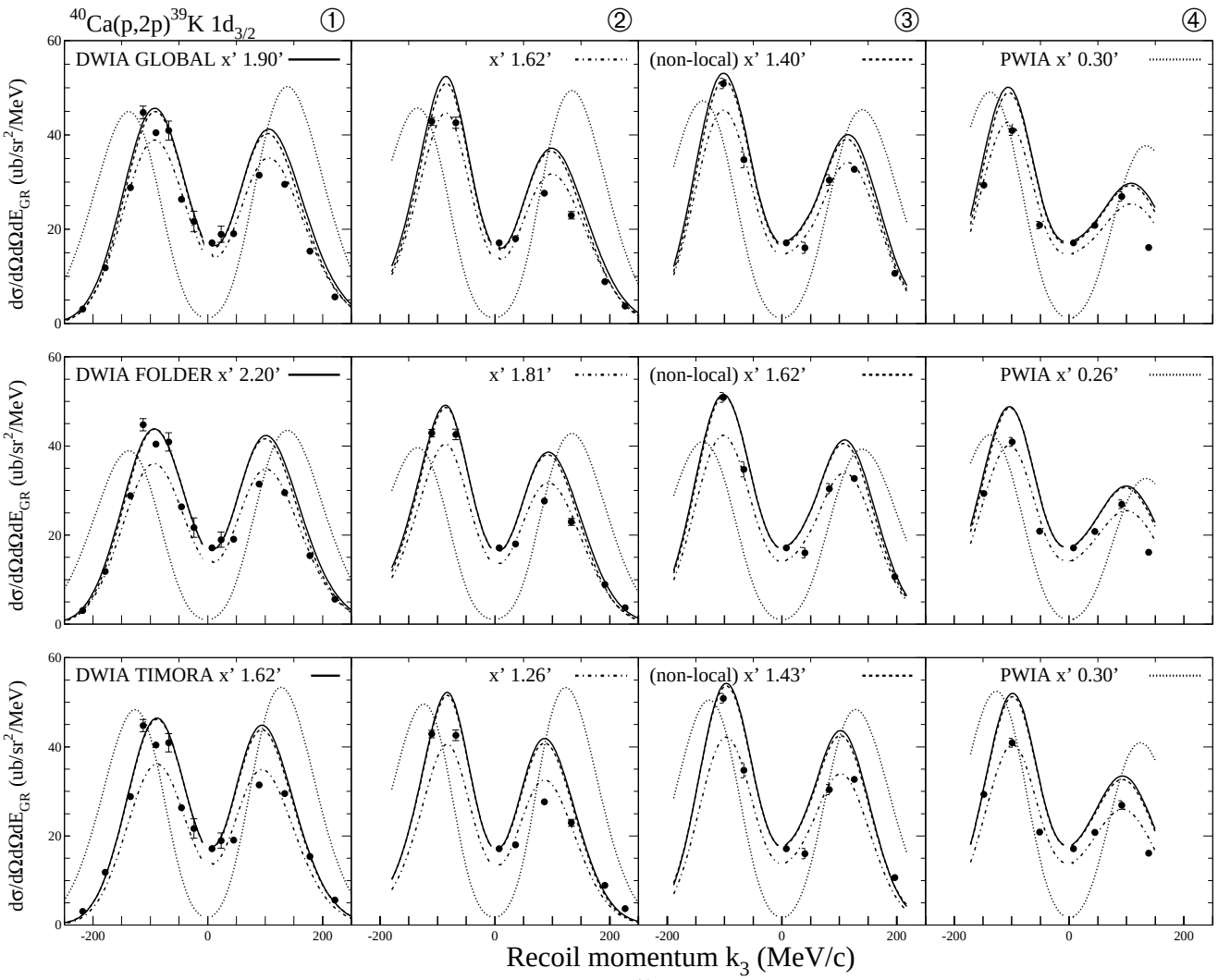

Figure 5.7: The differential cross sections for $^{40}\mathrm{Ca}(\vec{p}, 2p)$ reaction corresponding to proton knockout from the $1\mathrm{d}_{3/2}$ orbit are compared with DWIA calculations. The four kinds of kinematic conditions are indicated by encircled numbers. See the text for the theoretical lines.

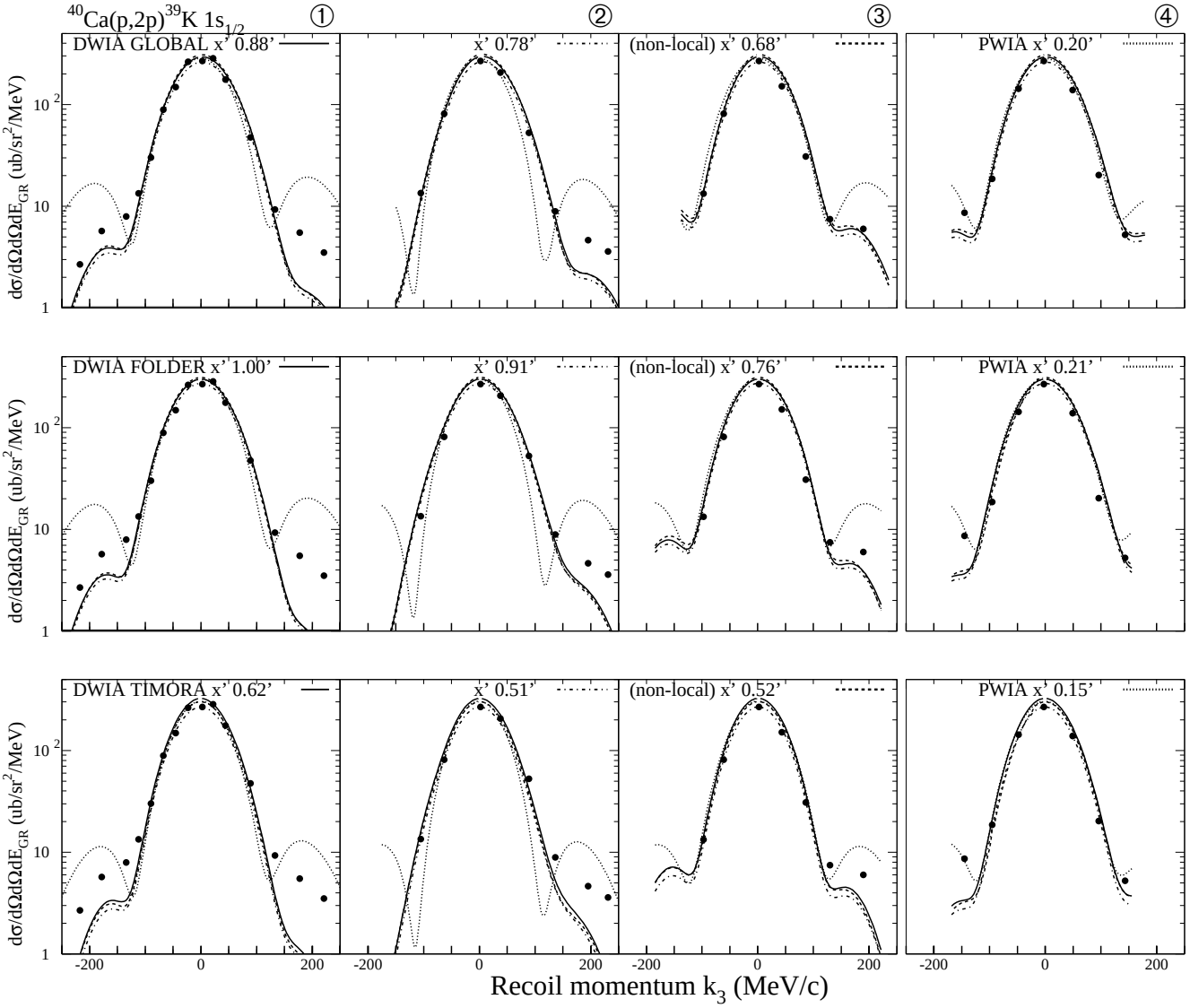

Figure 5.8: The differential cross sections for $^{40}\mathrm{Ca}(\vec{p}, 2p)$ reaction corresponding to proton knockout from the $2s_{1/2}$ orbit are compared with DWIA calculations. The four kinds of kinematic conditions are indicated by encircled numbers. See the text for the theoretical lines.

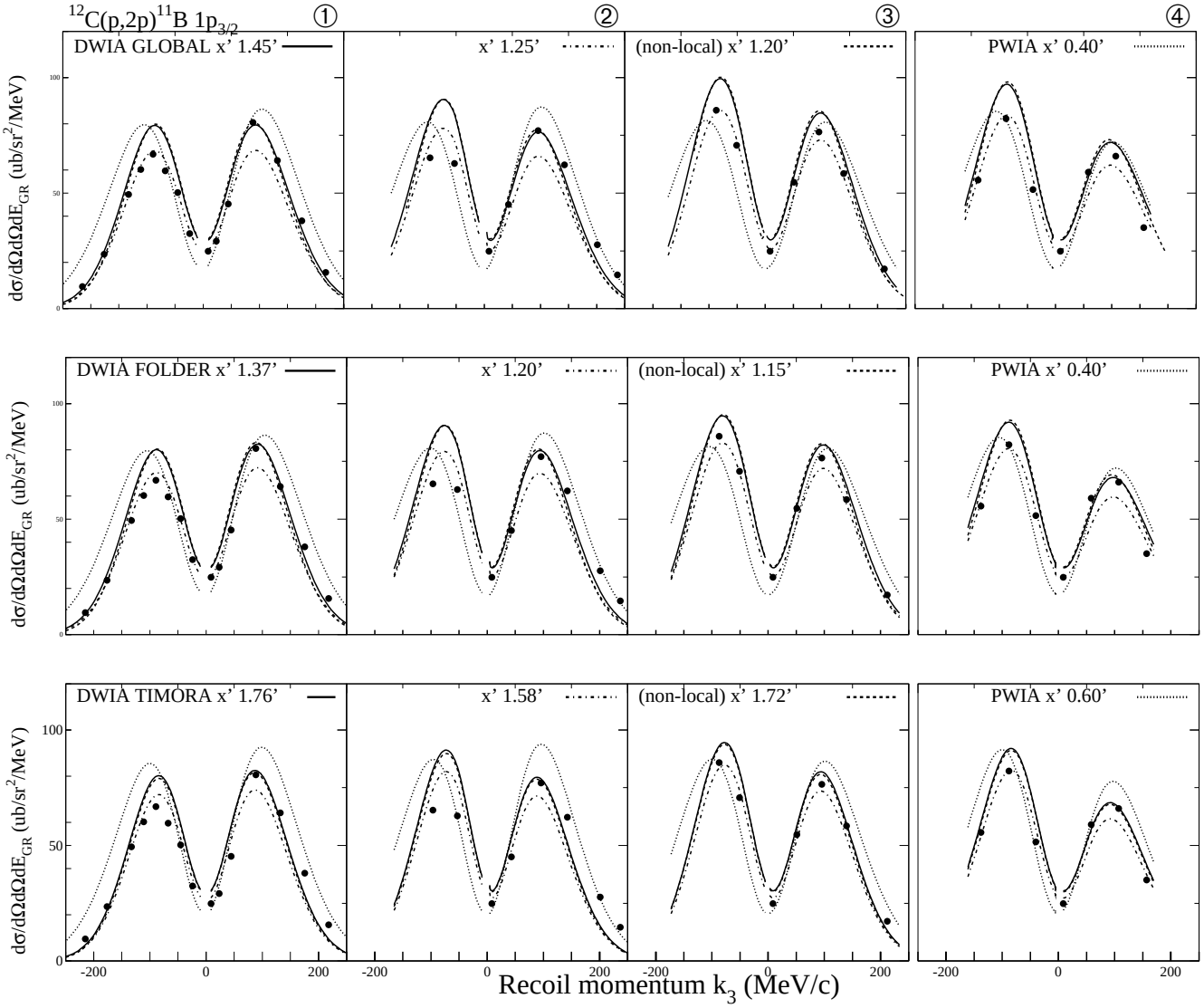

Figure 5.9: The differential cross sections for $^{12}\mathrm{C}(\vec{p}, 2p)$ reactions leading to the $1\mathrm{p}_{3/2}$-hole states are compared with DWIA calculations. The four kinds of kinematic conditions are indicated by encircled numbers. See the text for the theoretical lines.

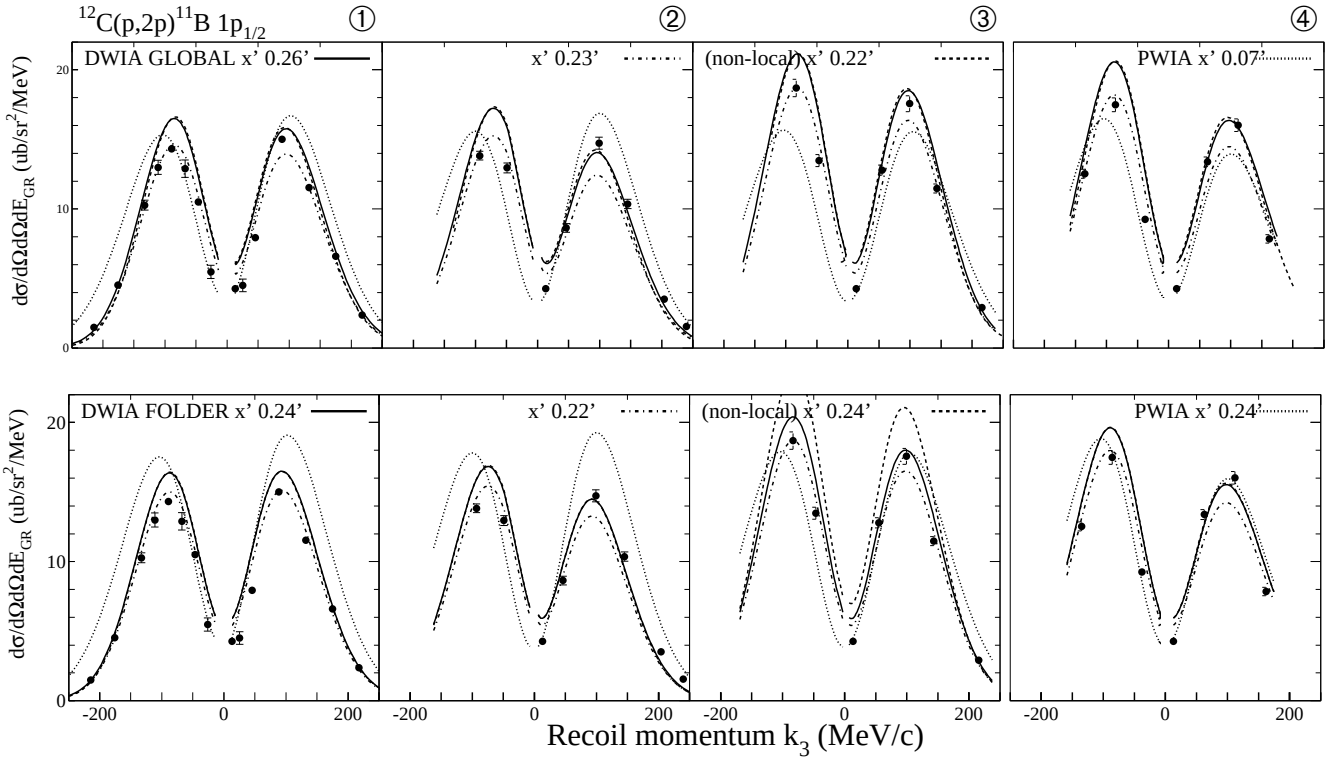

Figure 5.10: The differential cross sections for ^{12}C$(\vec{p}, 2p)$ reactions leading to the 1p$_{1/2}$-hole states are compared with DWIA calculations. The four kinds of kinematic conditions are indicated by encircled numbers. See the text for the theoretical lines.

for both states, again, for all of the four kinematic series.

5.3.3 Derivation of Spectroscopic Factors

For extraction of spectroscopic factors (S-factor) from comparison with DWIA calculation, the method of least squares were used. The procedures were different between the 2s$_{1/2}$-knockout from ^{40}Ca and $L \neq 0$ states knockout from ^{40}Ca and ^{12}C targets.

For the L=0 state, the procedure to determine S-factors is as follows:

- The results of the DWIA cross section $\sigma(\boldsymbol{k}_3)$ for three kinds of kinematic series ① – ③ described in Chap.3.2, were used to extract the S-factor.
- The experimental cross section data Y_i where values are more than one tenth of the maximum value were used for fitting. These data are within the region of $|\boldsymbol{k}_3| <$

90MeV/c, corresponding to the $2s_{1/2}$ state dominant region mentioned above. For the $2s_{1/2}$-knockout from ^{40}Ca in this work, the number N of experimental data for the fitting is 14.

- Only one parameter S-factor was used for fitting and the optimum value is obtained by least square fitting using the data described above.

- The error bar for the S-factor is determined from the values where the chi-square (χ^2/N) became twice of its minimum value.

For each set of calculations, "GLOBAL" with non-locality, "GLOBAL" without non-locality, "FOLDER" with non-locality or "FOLDER" without non-locality, the S-factors were determined by this procedure.

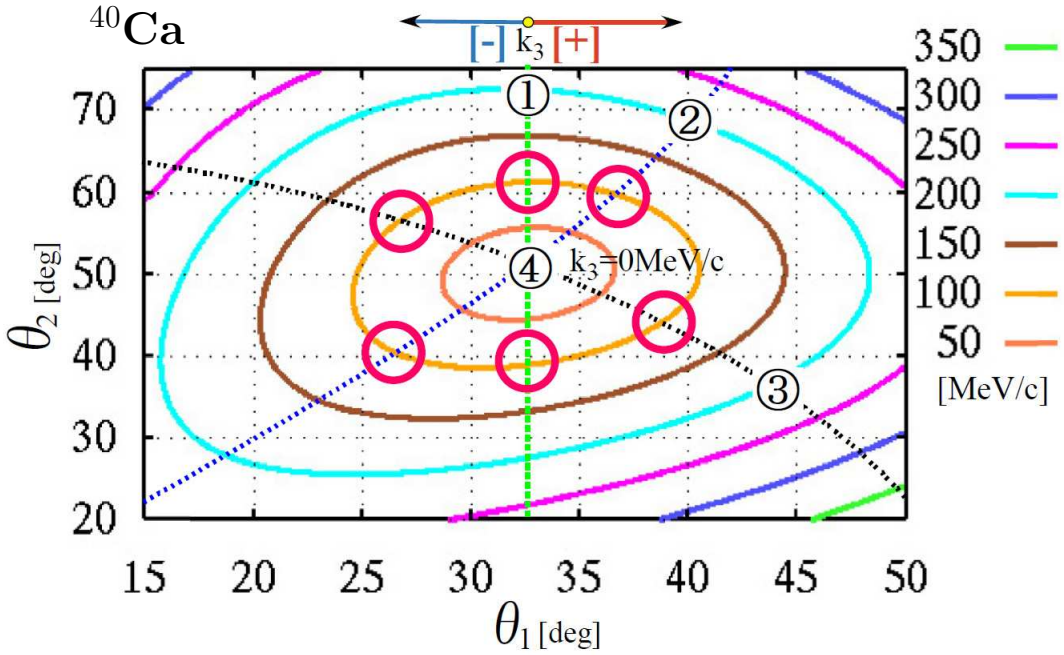

Figure 5.11: The contour map of the recoil momentum. Six open circles at 100MeV/c are the data region used for fitting of $L \neq 0$ states.

For the $L \neq 0$ states, each distribution of cross sections in each kinematic series shows two peaks at near $\pm$100MeV/c. The procedure for these states is as follows:

- As is the case of the L =0 state, the results of DWIA calculations for three kinds of kinematic series ① – ③

- For each region near ±100MeV/c, the experimental cross section data where values are more than 60% of maximum value near ±100MeV/c were used for fitting. Because the effect of corrections for finite acceptances were large near the dip region around the zero recoil point, those data close to the dip region were not used for fitting. In this work, for each region near ±100MeV/c the number of data by used for fitting was 2–5.

- For each of 6 peak region, shown in Fig. 5.12, a S-factor is obtained by using the least square fitting.

- The error bar for the S-factor is determined as the difference between the maximum and the minimum values of 6 S-factors.

For each parameter set of calculations, "GLOBAL" with non-locality,"GLOBAL" without non-locality, "FOLDER" with non-locality or "FOLDER" without non-locality, the S-factors were determined by this procedure for $L \neq 0$ three states.

By using the results of the procedure for the "GLOBAL" with non-locality set, the calculation results multiplied by S-factors for $1d_{3/2}$-knockout and $2s_{1/2}$-knockout from ^{40}Ca, and $1p_{3/2}$-knockout and $1p_{1/2}$-knockout from ^{12}C are shown in Figs. 5.13 – 5.16, respectively.

The values of S-factors extracted from these procedure were described in Table 5.3 and are shown in Fig. 5.17 with other S-factors from $(e, e'p)$ reactions [69, 70, 71, 72, 73, 74, 75]. Figure 5.18 shows normalized factors obtained by dividing the S-factor of this work by those of $(e, e'p)$ reactions These figures show that the S-factors from this work are not so different between the parameter sets of "GLOBAL" and "FOLDER" with or without non-locality corrections and these values are about 70% of the values obtained from $(e, e'p)$ reactions. And the error bars for S-factors determined are ± 15% for maximum. These sizes of errors are comparable to those from $(e, e'p)$ reactions, where

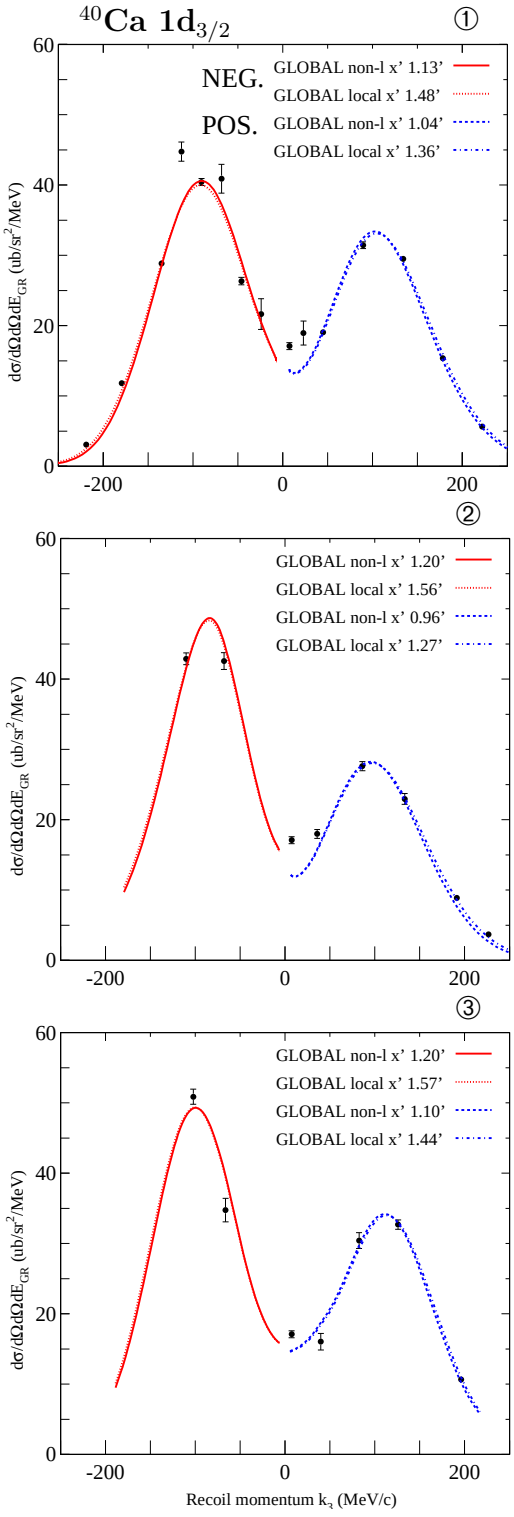

Figure 5.12: The results of fitting for six peaks for $1d_{3/2}$-knockout from ^{40}Ca. Each line is normalized by a least square fitting for calculations.

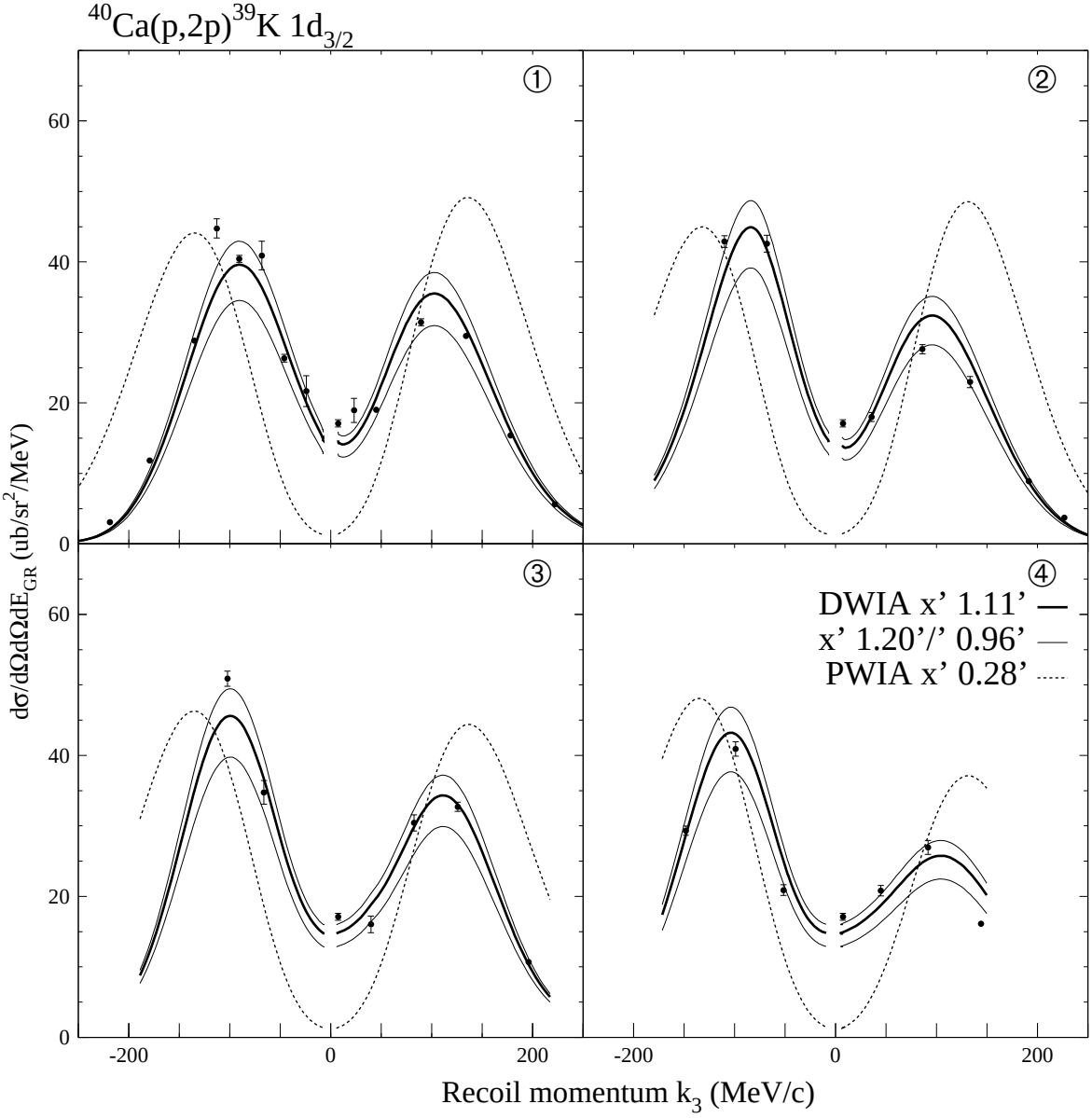

Figure 5.13: The lines are normalized by S-factors for $1d_{3/2}$-knockout state from ^{40}Ca. The bold solid lines are multiplied by the most probable value of S-factor. The thin solid lines shown regions of error bars.

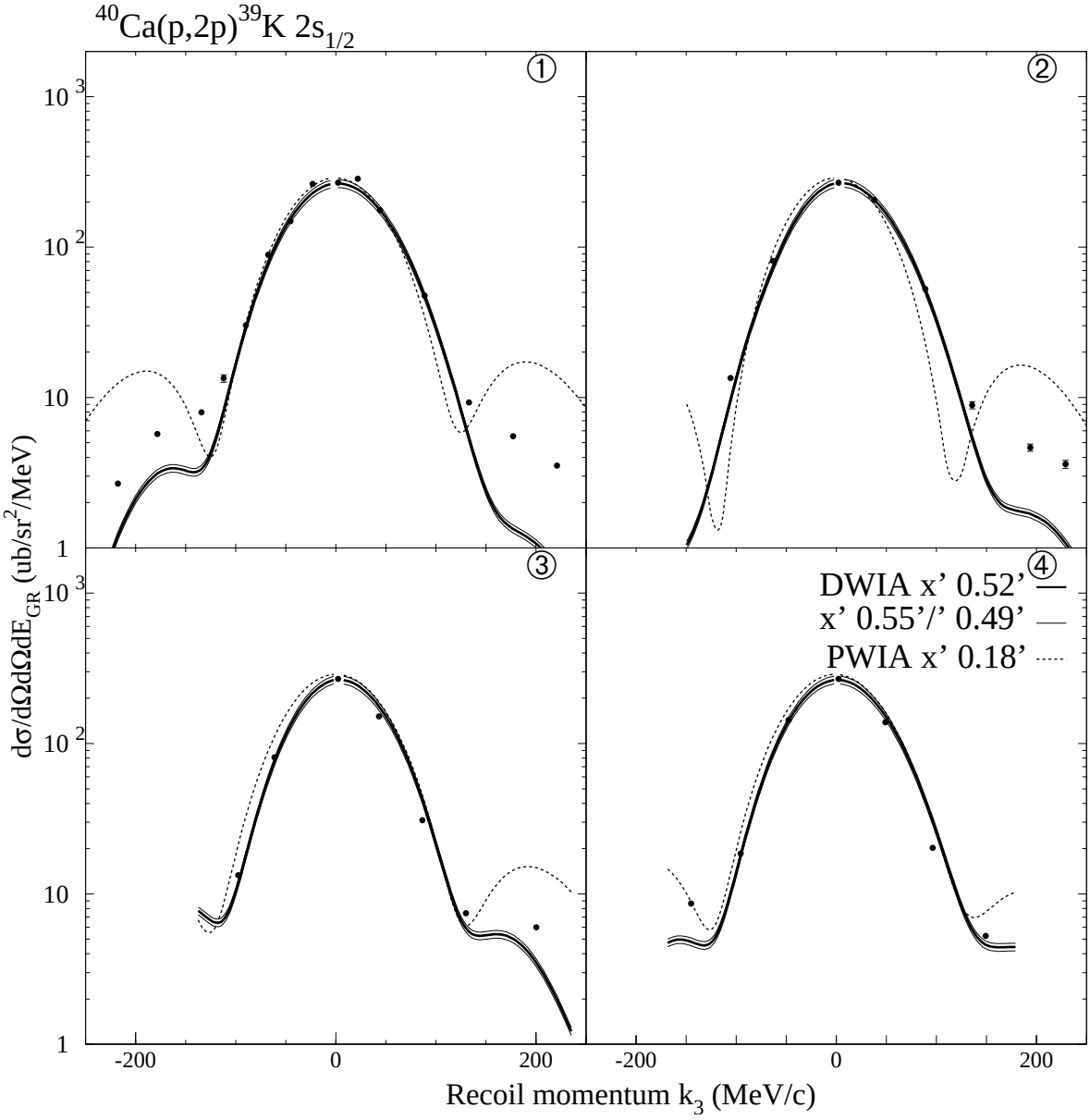

Figure 5.14: The lines are normalized by S-factors for $2s_{1/2}$-knockout state from ^{40}Ca. The lines are same as in Fig. 5.13.

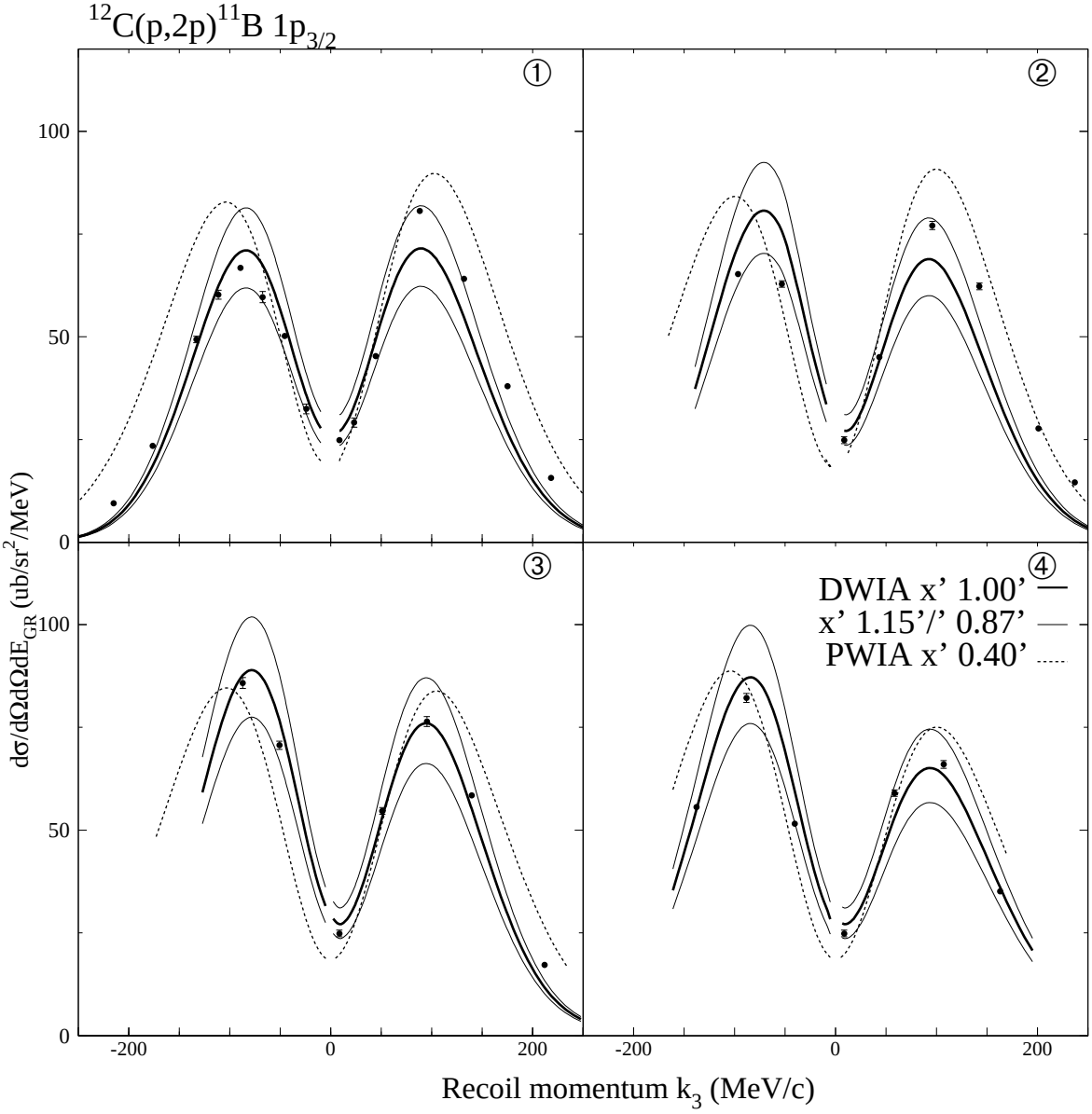

Figure 5.15: The lines are normalized by S-factors for $1p_{3/2}$-knockout state from ^{12}C. The lines are same as in Fig. 5.13.

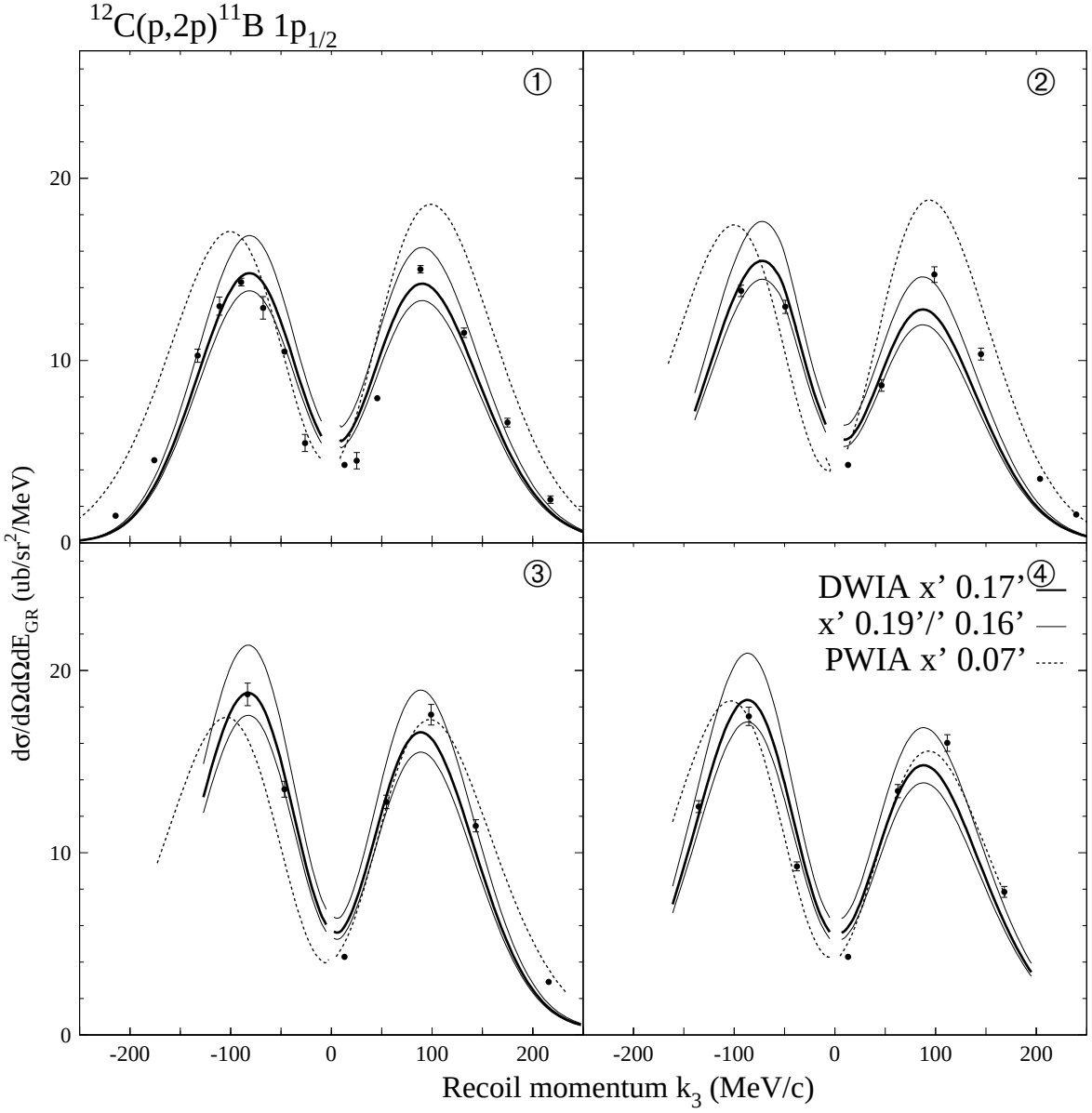

Figure 5.16: The lines are normalized by S-factors for $1p_{1/2}$-knockout state from ^{12}C. The lines are same as in Fig. 5.13.

main parts of errors are caused by fitting ambiguity, as well.

Table 5.3: S-factors derived from present study and other results from $(e, e'p)$ reactions

target state	S-factor	min.-max.	(e,e'p)
Type of DWIA calc.			
^{40}Ca $1d_{3/2}$			2.58(19) [69]
GLOBAL-NL	1.11	0.97 – 1.20	
GLOBAL-LO	1.45	1.36 – 1.57	
FOLDER-NL	1.28	1.08 – 1.44	
FOLDER-LO	1.69	1.43 – 1.90	
^{40}Ca $2s_{1/2}$			1.03(7) [16]
GLOBAL-NL	0.52	0.49 – 0.55	
GLOBAL-LO	0.68	0.64 – 0.72	
FOLDER-NL	0.58	0.53 – 0.62	
FOLDER-LO	0.76	0.71 – 0.82	
^{12}C $1p_{3/2}$			1.72(11) [70]
GLOBAL-NL	1.00	0.87 – 1.15	
GLOBAL-LO	1.21	1.12 – 1.39	
FOLDER-NL	0.97	0.84 – 1.07	
FOLDER-LO	1.15	0.99 – 1.27	
^{12}C $1p_{1/2}$			0.26(2) [70]
GLOBAL-NL	0.17	0.16 – 0.19	
GLOBAL-LO	0.20	0.18 – 0.22	
FOLDER-NL	0.16	0.14 – 0.17	
FOLDER-LO	0.18	0.17 – 0.20	

NL : with non-locality correction

LO : without non-locality correction

5.4 Analyzing Powers for ^{40}Ca and ^{12}C Targets

5.4.1 ^{40}Ca$(\vec{p}, 2p)^{39}$K Reaction

In the Fig. 5.19, the distribution of A_y for $1d_{3/2}$ and $2s_{1/2}$-knockout from ^{40}Ca are shown. This figure shows the results of three sets of DWIA calculations with non-locality corrections, "GOLBAL", "FOLDER" and "TIMORA" called as in Sec. 5.2.3 corresponding to

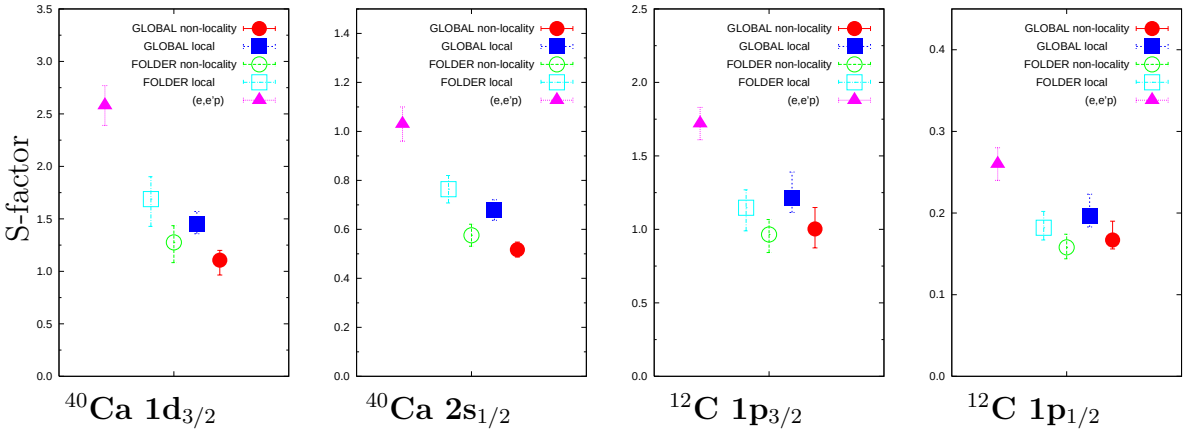

Figure 5.17: S-factors from present study and from $(e, e'p)$ reactions are plotted for each state

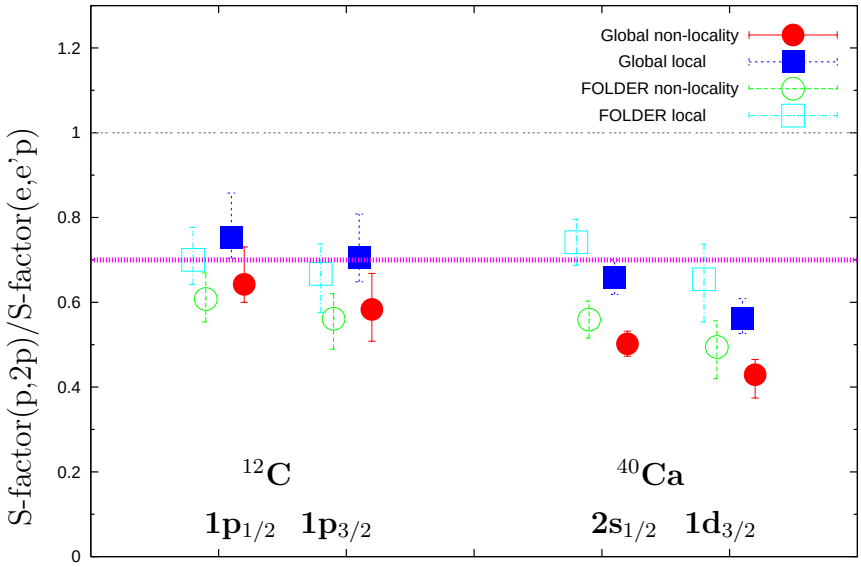

Figure 5.18: Normalized S-factors from present study divided by the results from $(e, e'p)$ reactions

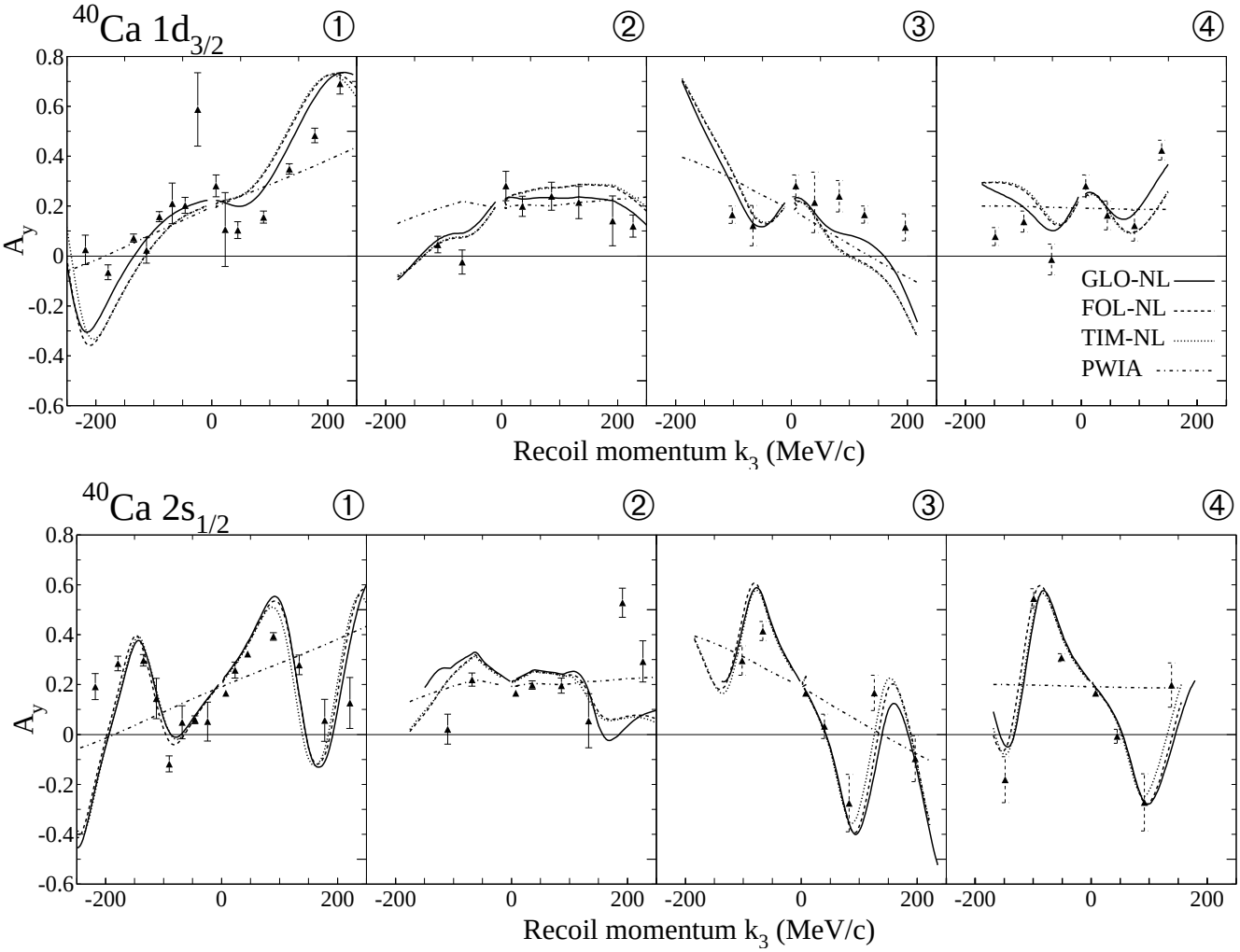

Figure 5.19: The distributions of analyzing powers for ^{40}Ca$(\vec{p}, 2p)$ reactions: The upper panel and bottom panel in this figure correspond to $1d_{3/2}$- and $2s_{1/2}$-knockout reaction, respectively. The four kinds of kinematic conditions are indicated by encircled numbers. See the text for the theoretical lines.

solid lines, dashed lines and dotted lines, respectively. And the results of PWIA calculations are drawn with dashed dotted lines. From these figure, all three DWIA calculations give good prediction of the distributions of the A_y's for whole four kinematic series.

5.4.2 ^{12}C$(\vec{p}, 2p)^{11}$B Reaction

The Fig. 5.20 shows the results of three DWIA and PWIA calculations for $1p_{3/2}$- and $1p_{1/2}$-knockout states from ^{12}C. In this figure, solid lines are the results of "GOLBAL" with non-locality corrections, dashed lines are of "FOLDER" with non-locality correc-

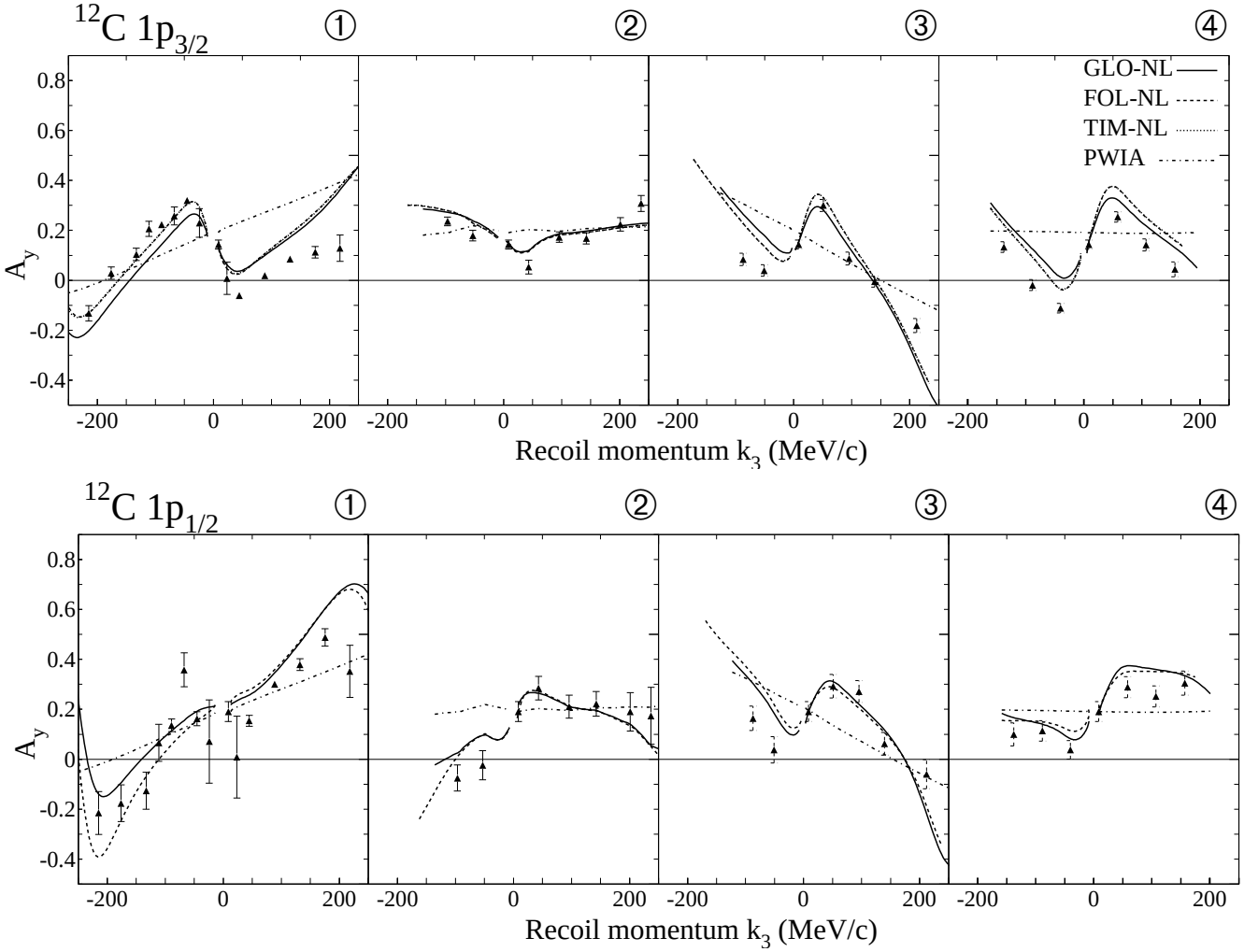

Figure 5.20: The distributions of analyzing powers for ^{12}C$(\vec{p}, 2p)$ reactions: The upper panel and bottom panel in this figure correspond to $1p_{3/2}$- and $1p_{1/2}$-knockout reaction, respectively. The four kinds of kinematic conditions are indicated by encircled numbers. See the text for the theoretical lines.

tions, dotted lines are of "TIMORA" with non-locality corrections and dashed dotted lines are of PWIA calculations. For $1p_{1/2}$-knockout in these figure, there aren't the results of the parameter set of "TIMORA" which are based on the relativistic Hartree model as mentioned above. DWIA calculations of three parameter sets give good prediction for A_y's for both reactions for all four kinematic series.

5.4.3 Confirmation of J-dependence

Two states like $1p_{3/2}$ and $1p_{1/2}$ orbits of ^{12}C are called as J upper ($J_>$) and J-lower ($J_<$) because the angular momentum L's are same, and the total angular momenta are different. As mentioned in Sec. 1.2, the difference of distributions of A_y's, which is known as "j-dependence", was predicted by the DWIA.

In Fig. 5.21, each panel shows the experimental results and DWIA calculation results from the parameter set "GLOBAL" with non-locality corrections for these two states. In the kinematic series ① and ②, clear j-difference of A_y are seen in both of experimental and theoretical results. On the other hand, for the kinematic series ③ and ④, it is difficult to distinguish $1p_{3/2}$- and $1p_{1/2}$-knockout states in both of experimental and theoretical results. But it is emphasized that DWIA calculations reproduce the experimental data.

5.5 ^{6}Li$(\vec{p}, 2p)^5$He Reaction

Figure 5.22 shows the results of (being assumed)$1p_{3/2}$- and $1s_{1/2}$-knockout from $^6\mathrm{Li}(\vec{p}, 2p)^5\mathrm{He}$. For only one series of kinematics ①, the measurement was performed. The solid lines are the results of parameter set "TIMORA" with non-locality correction and dashed lines are that of PWIA calculations.

For A_y, though it seems that the data for both of $1p_{3/2}$ and $1s_{1/2}$ states are reproduced by DWIA calculations, calculations for both states give similar results. For the knock-out from $1s_{1/2}$, a good agreement between the experimental data and the calculation is given. On the other hands, for the $1p_{3/2}$ proton knockout, DWIA calculations cannot reproduce the cross sections at all. DWIA calculations predict a minimum at 0 MeV/c, but the experimental data show a peak there. This discrepancy looks inconsistent with experimental data of $(e,e'p)$ reactions [67, 68].

In the this experiment, the width of the recoil momentum of data point near 0MeV/c was about 35 MeV/c (FWHM). This wide ranges of the recoil momentum easily dull possible precise structure. Therefore , the data with more high resolution in the recoil

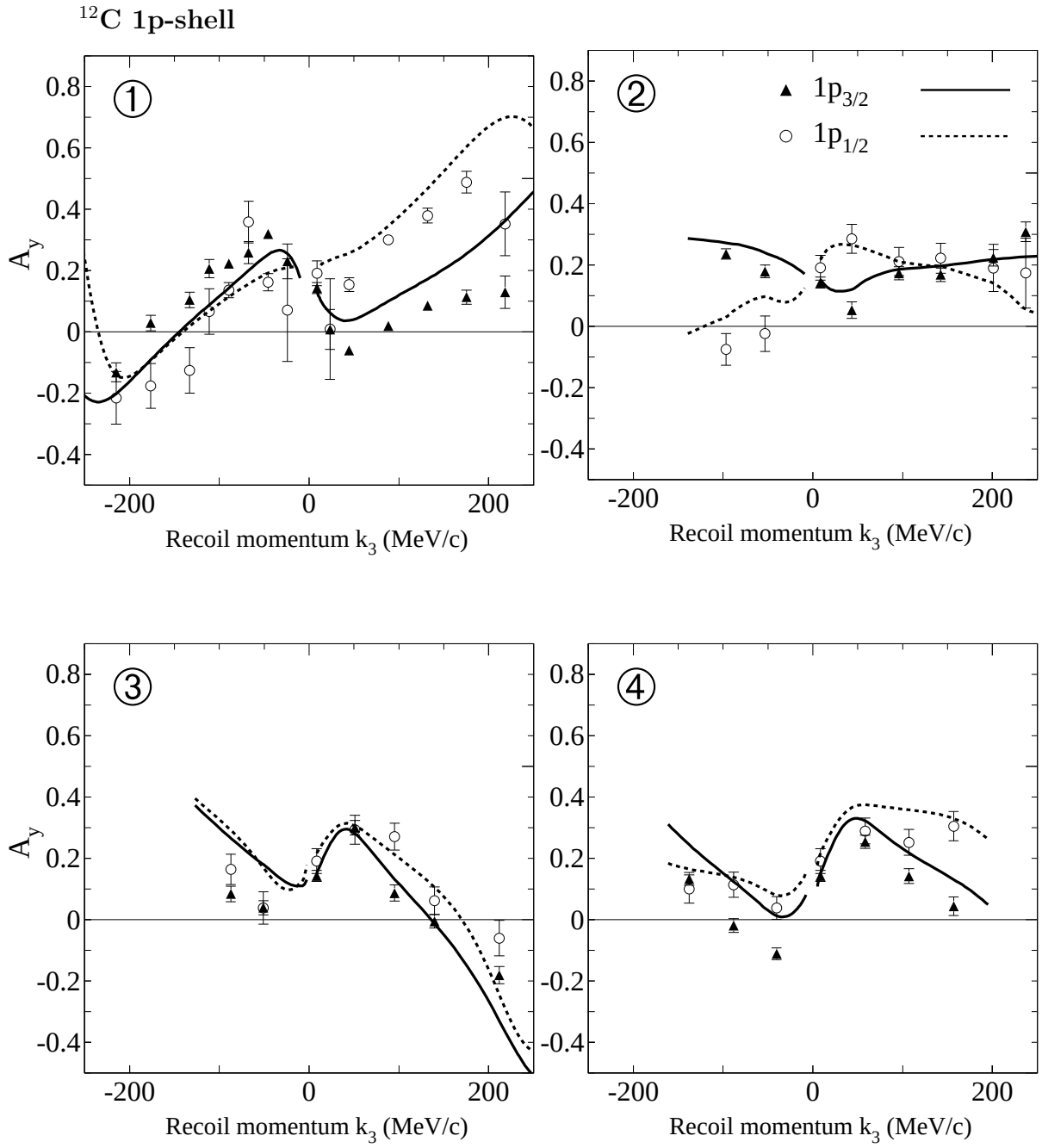

Figure 5.21: j-dependence between $1p_{3/2}$ and $1p_{1/2}$ states from ^{12}C in four kinematic series.

momentum are required to check the consistency with the $(e,e'p)$ result.

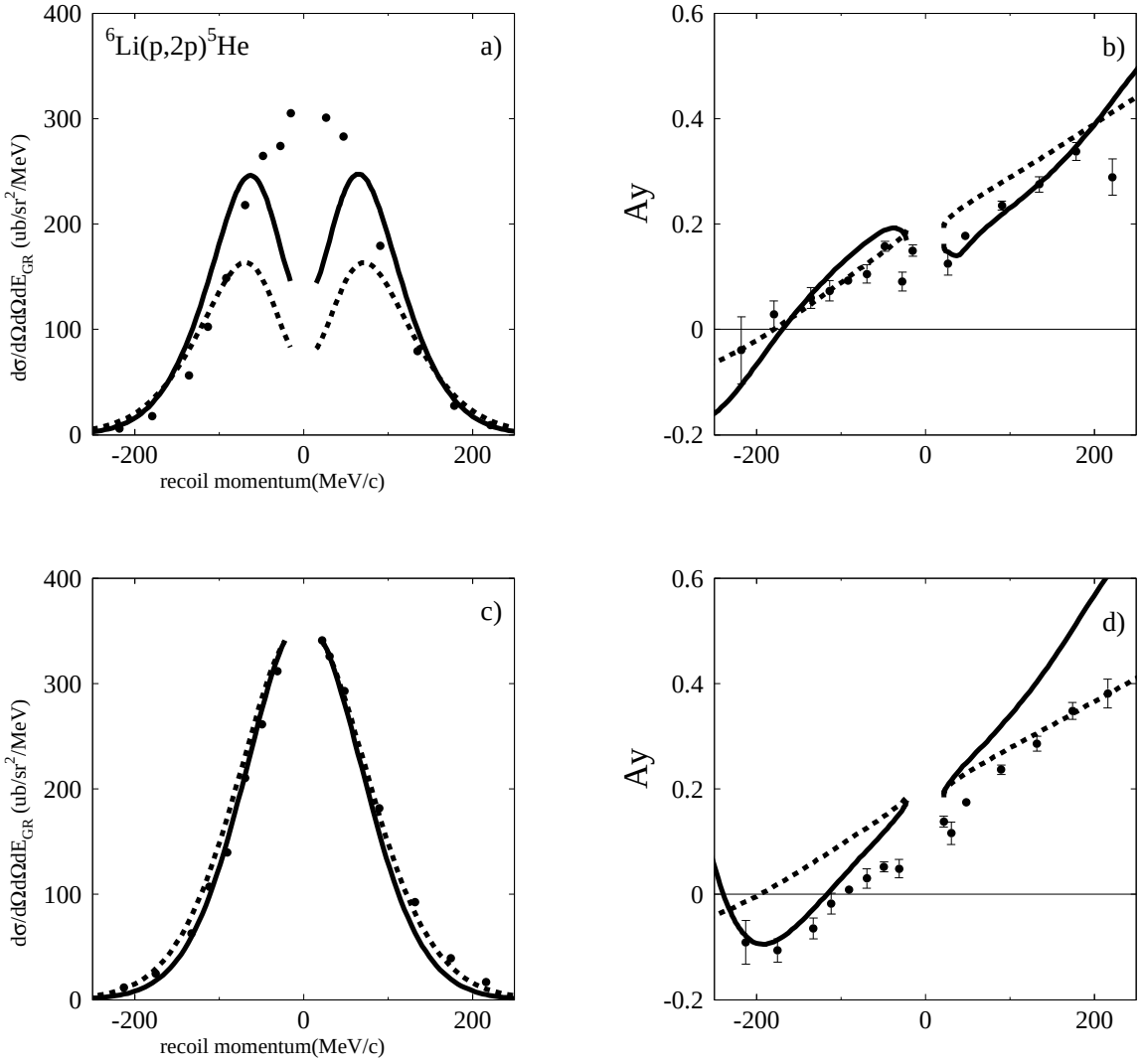

Figure 5.22: The distribution of differential cross sections and A_y's for ^{6}Li$(\vec{p}, 2p)$ reaction : The left panels show cross sections, the right panels show A_y's, the upper panels are for assumed $1p_{3/2}$-knockout reactions and the bottom panels are for $1s_{1/2}$-knockout reactions. The solid lines are the results of parameter set "TIMORA" with non-locality correction and the dashed lines are that of PWIA calculations.

5.6 Summary of this Chapter

In this chapter, the experimental results of $1d_{3/2}$- and $2s_{1/2}$-knockout from ^{40}Ca, $1p_{3/2}$- and $1p_{1/2}$-knockout from ^{12}C and $1p_{3/2}$- and $1s_{1/2}$-knockout, which are tentatively assumed, from ^{6}Li for various kinematic series were compared with DWIA calculations.

For ^{40}Ca and ^{12}C targets, the recoil-momentum distributions of the differential cross sections for all of the four states are reproduced by DWIA calculations fairly well, for all of the four kinematic series. spectroscopic factors (S-factors) for these four states were derived from normalization of the DWIA calculations to the experimental data. The ambiguities in deducing the S-factors were estimated quantitatively as $\pm 6\% \sim \pm 15\%$ error bar from the fitting for various kinematics. These uncertainties are similar size as those of results from $(e, e'p)$ reactions. Although these S-factor values deduced from the present $(p, 2p)$ study are $60-70\%$ of those from $(e, e'p)$ study, the S-factors for different between states of the same target nucleus and even between those for different target nuclei are nearly the same as $(e, e'p)$ results.

For $1d_{3/2}$-knockout from ^{40}Ca, many S-factor values were deduced by several groups calculations at various incident energies [21, 23, 24, 28, 29, 30, 59]. Those S-factor values, including the present result are plotted in a $2J + 1$ unit as a function of the incident energy E_p in Fig. 5.23. These S-factors show a systematic incident-energy dependence. Since most of these values are based on early day's experimental data and, therefore, large ambiguity may be included, but this tendency may suggest that further theoretical progress in theoretical treatment is required in order to deduced reliable S-factor values, quantitatively.

The recoil-momentum distributions of A_y for ^{40}Ca and ^{12}C targets, are reproduced by DWIA calculations fairly well, independently for the kinematical series. For the ^{12}C targets, in particular, significant differences between $1p_{3/2}$ and $1p_{1/2}$ knockout data, namely j-dependence, were observed and reproduced by calculations. This means that by choosing the kinematical condition, such as $30^\circ - 30^\circ$ angle set in Fig. 5.24, this effect can be use to determine the total angular momentum J of deep hole states, reliably.

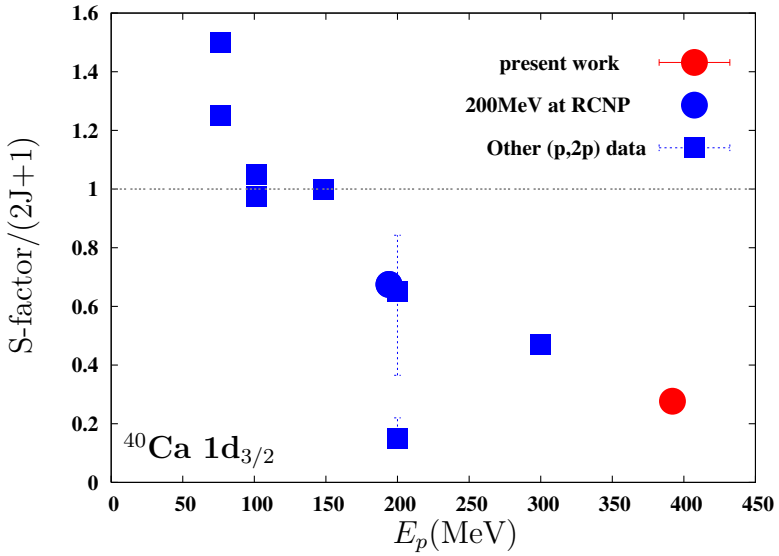

Figure 5.23: The S-factors for $1d_{3/2}$ proton knocked-out from ^{40}Ca are plotted in a $2J+1$ unit as a function of incident energy. Closed circles are result of our group and closed squares are those by other groups.

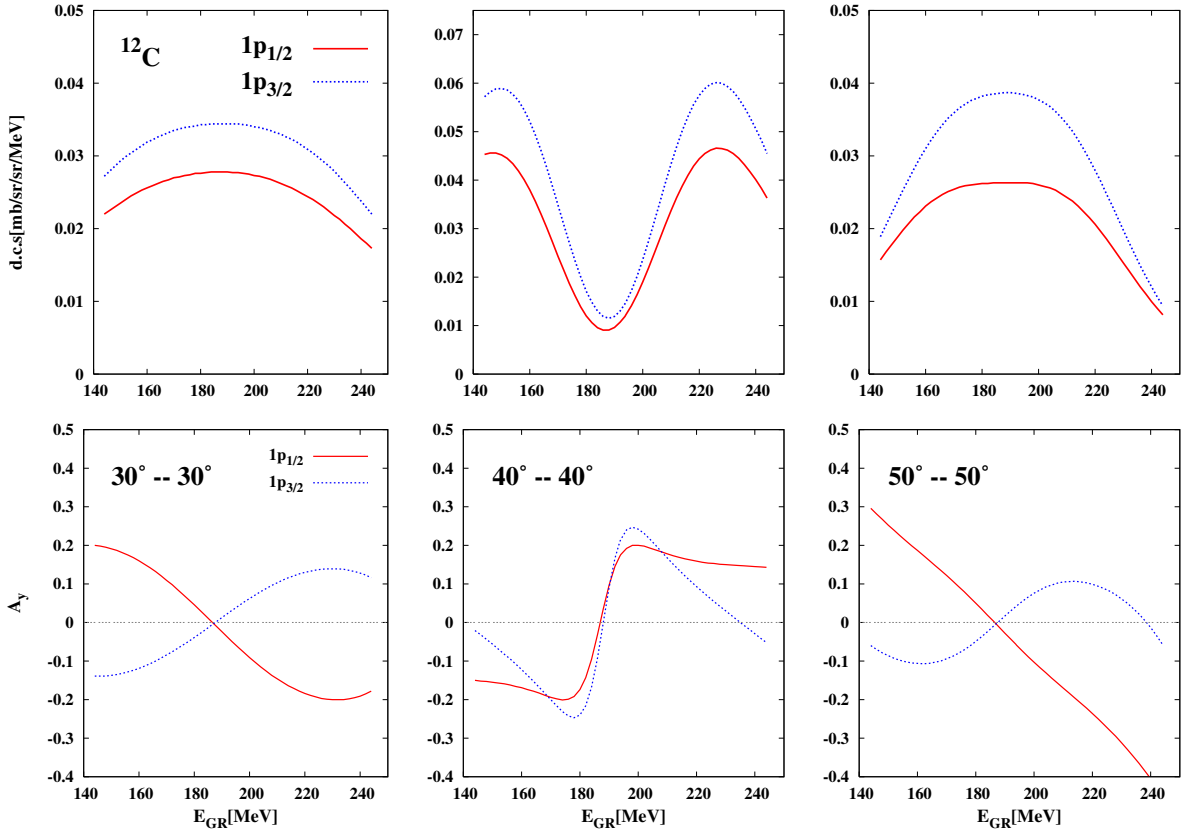

Figure 5.24: The calculation results of j-dependence between $1p_{1/2}$ and $1p_{3/2}$ knockout from ^{12}C for symmetry detection angle sets, (30° - 30°), (40° - 40°) and (50° - 50°).

For ^{6}Li target, the experimental results of the reaction leading to the higher excited state of residual ^{5}He are well reproduced by DWIA calculations assuming $1s_{1/2}$ knockout. But those corresponding to the lower excited state, DWIA calculations cannot reproduce the cross section at all. Then, an additional experiment for this target are performed which are described in the next chapter in detail.

Chapter 6

Precise Measurement for ^{6}Li$(\vec{p}, 2p)$ ^{5}He Reaction

As mentioned in Chap. 5, an experiment with high recoil momentum resolution for the knockout reaction from ^{6}Li was performed to investigate the differential cross section, especially near 0 MeV/c in recoil momentum.

In this chapter, the experimental condition was described first. Next, the experimental result was shown, and the comparisons with theoretical calculations and electron-induced knockout reactions were discussed.

6.1 Experimental Condition

To perform high resolution measurements for recoil momentum, it is necessary that the quantities of $\Delta\Omega_{\rm GR}$, $\Delta\Omega_{\rm LAS}$ and $\Delta E_{\rm GR}$ in the equation (4.1) are small enough not to smear out the changes of cross sections. The energy resolution of the GR is high enough so that we can analyze data by using software. On the other hand, the tracking resolution of elevation angles for both spectrometers are not enough. Therefore, new slits with small acceptance are made and used for both spectrometers.

6.1.1 Solid Angle

As mentioned above, angular acceptances reflect regions of recoil momentum. The opening angles of entrance slits are determined so as to reduce the recoil momentum ranges less than 10 MeV/c. For the LAS, the solid angle of the slit was 0.90 msr where vertical and horizontal acceptances were ±15 mrad. For the GR, the solid angle of the slit was 0.80 msr where the vertical acceptance was ±10 mrad and the horizontal acceptance was ±20 mrad. In addition, we used software gate for the GR for the horizontal acceptance, then, the practical horizontal acceptance was ±5mrad in analysis and the effective solid angle was 0.20 msr.

6.1.2 Kinematics

As shown in Chap. 5, for the experimental results for ^{40}Ca and ^{12}C targets, the DWIA calculations almost reproduce the distributions of differential cross sections as a function of recoil momentum $\boldsymbol{k}_3$ in all kinematical series. Then, it is assumed that the effects of distortions for these conditions are able to be estimated by the DWIA calculations, relatively. For this precise measurement, we chose the kinematic conditions where the angle of the LAS was fixed at 51.62° and various combinations of the angle of the GR and the kinetic energy $E_{\rm GR}$. In Fig. 6.1, a two-dimension map of recoil momentum against $E_{\rm GR}$ and $\theta_{\rm GR}$ for $E_{\rm sep}$= 4.6MeV is shown. The hatched regions shows all of the setting acceptance of this experiment. Figure 6.2, shows actual analyzed regions in the present work for two kinds of knockout energies. As shown in the figures, the recoil momentum ranges from -150 MeV/c to +100 MeV/c including 0 MeV/c point in the case of the lower excited states, and from -200 MeV/c to +100 MeV/c in the case of higher excited states. In the latter case, the minimum recoil momentum is about 22 MeV/c.

6.1.3 Effects of Finite Acceptances

Under above conditions for solid angles $\Delta\Omega_{\rm GR}$, $\Delta\Omega_{\rm LAS}$ and kinetic energy bite $\Delta E_{\rm GR}$, ranges of the recoil momentum $\boldsymbol{k}_3$ were estimated by the Monte-Carlo simulation and

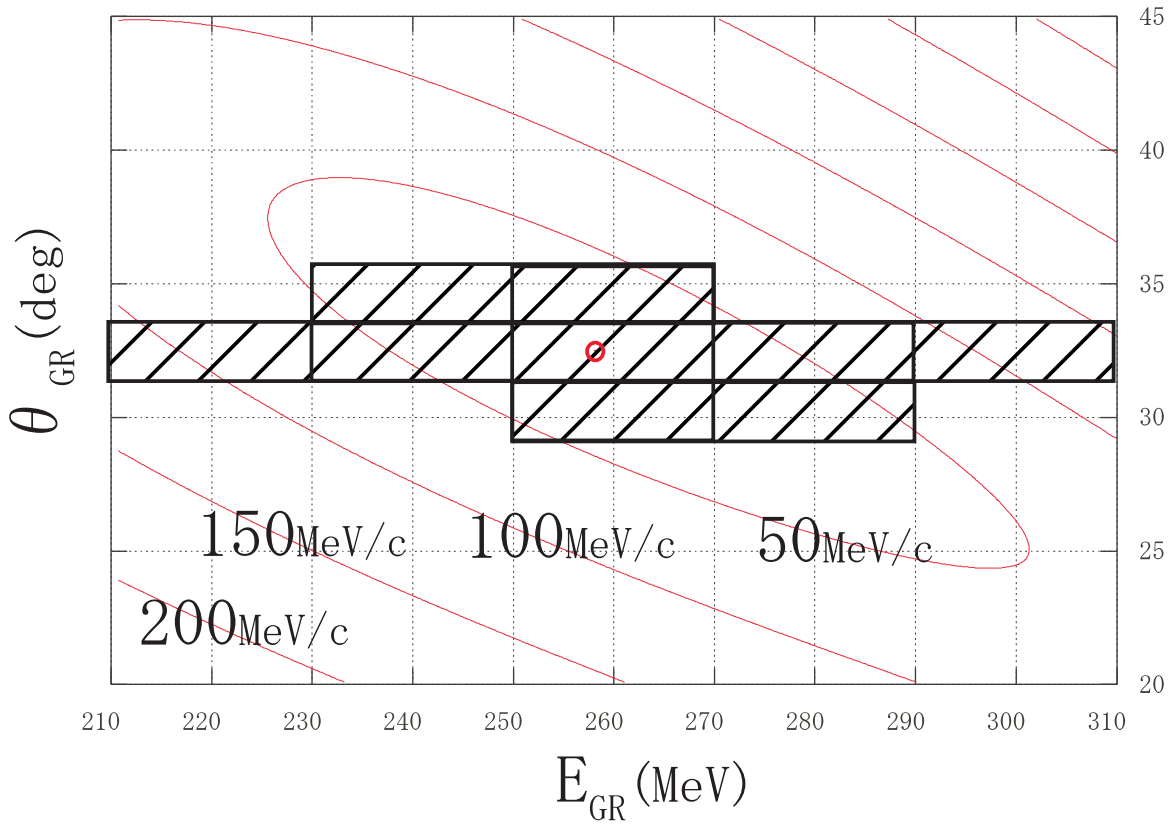

Figure 6.1: The contour map of recoil momentum $\boldsymbol{k}_3$: The horizontal axis is a kinetic energy of the GR and the vertical axis is an angular of the GR. The increment of elevation between two contours is 50 MeV/c. The hatched regions are acceptances of 9 sets detected.

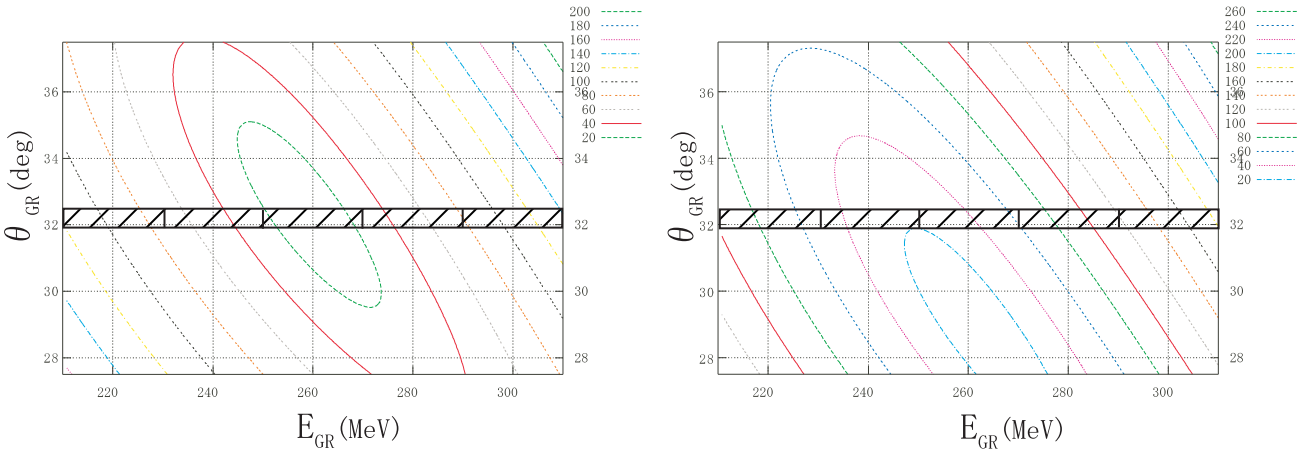

Figure 6.2: The contour maps of recoil momentum $\boldsymbol{k}_3$: The hatched regions were analyzed in detail. The contour map in the left figure is for the lower excitation state and calculated at $E_{\rm sep}$ = 4.6MeV. The one in the right figure is the for upper excitation state and calculated at $E_{\rm sep}$ = 22MeV.

result was about 10MeV/c in FWHM for every data point including the point close to 0MeV/c. For the DWIA calculations of cross sections and analyzing powers A_y's, the effects of finite solid angles and finite kinetic energy were estimated by using the Monte-Carlo method. In Fig. 6.3, that is the case of $1p_{3/2}$ knockout reaction, the dashed line indicates calculations on center values of experimental condition without corrections, the solid line indicates those with corrections of acceptances of this precise experiment and the short dashed line indicates those simulated the previous experiment acceptances. Comparing with three lines, it has been shown that the correction effects for the precise measurement are much clear to the no correction calculations than before.

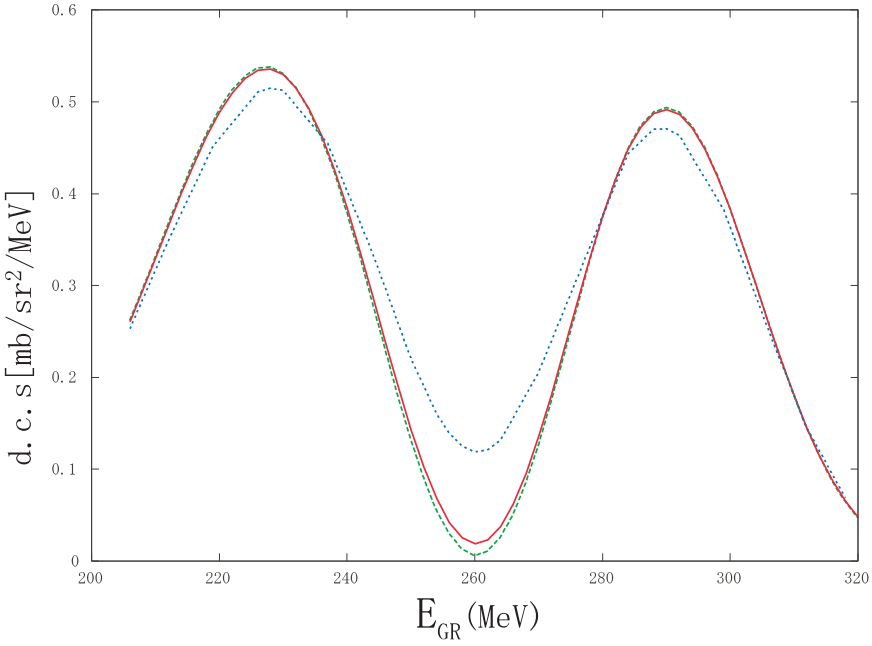

Figure 6.3: Difference of correction effects for finite acceptance: The short dashed line is under conditions for previous experiment described in Chap. 5,4 and the solid line is for this precise experiment. The each value on the long dashed line was calculated for each setting point.

6.1.4 Experiment

The experimental detail is mostly same as those described in Chap. 3. Using the two-arm spectrometers in Fig. 3.5, this measurement was performed in the WS course in Fig. 3.2. The beam current was in the range of 180–300 nA, a typical energy resolution of the

incident proton beam was about 150 MeV in FWHM and a typical beam polarization was about 65%. The thickness of ^{6}Li target was 37.6 mg/cm^2 determined by a weighting method with 5% uncertainty.

6.2 Experimental Result

In Fig. 6.4, a typical separation-energy spectrum for this experiment is shown. The resolution of separation energies was about 350 keV in FWHM. Actually, we took data corresponding to the two dimensional area shown in Fig. 6.1 and obtained cross section data for the left side peak in Fig. 6.4 are plotted in three dimension in Fig. 6.5. The experimental results of cross sections were characterized by a function of recoil momentum $\boldsymbol{k}_3$, again.

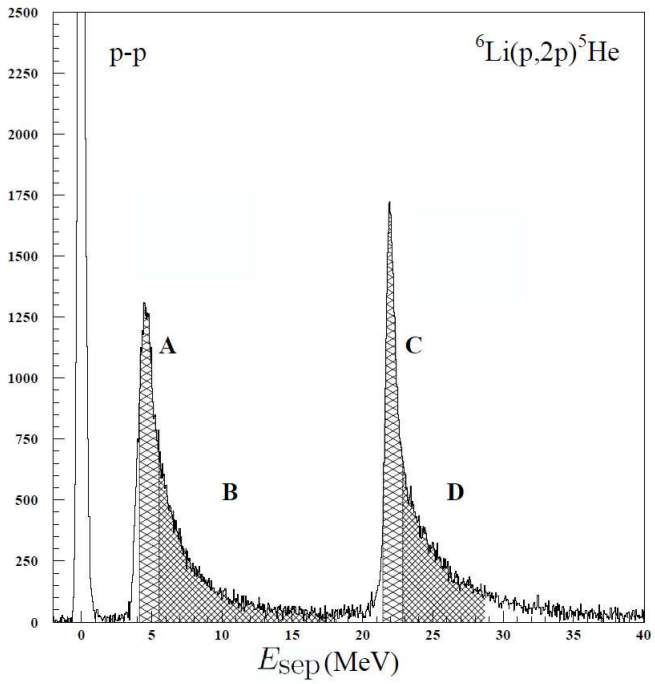

Figure 6.4: The separation energy spectrum for the reaction ^{6}Li(p,2p)^{5}He. The horizontal axis is the separation energy. The most left peak was the spectrum for $p-p$ scattering from contamination in the ^{6}Li target. The shaded areas in the figure are explained in the text.

The dip in each of the plotted data is located along the major diameter of the ellipse-

like equi-momentum lines in Fig. 6.1. Namely, the dip corresponds to the minimum recoil momentum point in each data row, which shows that the cross section reflects momentum dependence of the bound proton wave function.

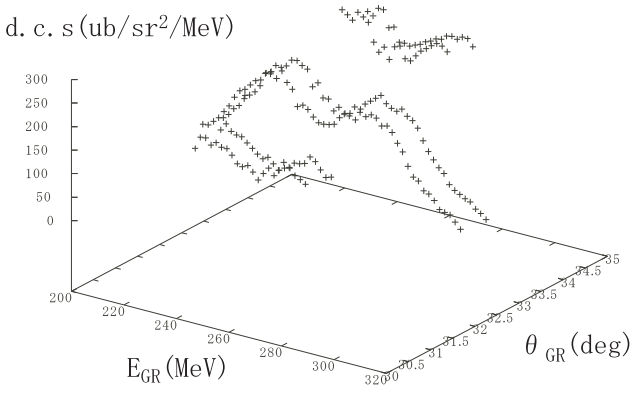

Figure 6.5: Three-dimension plot of differential cross section: The plane axes are the kinetic energy and the angular of the GR. These are result for region "A" of the spectrum in Fig. 6.4.

Since the both peaks obtained in ^{6}Li$(p, 2p)^5$He reaction has broad tails toward higher separation energies, and it is known that the ground state of ^{5}He is a resonance state of a proton and an alpha particle with 0.6 MeV width, we divide each peak into two region, a narrow region in the lower separation energy side and a tail region in the higher excitation side, and analyzed them separately. The actual energy regions are $4.2 < E\text{sep} < 5.6$ MeV, $5.6 < E\text{sep} < 18.2$ MeV, $21.5 < E\text{sep} < 22.9$ MeV, $22.9 < E\text{sep} < 28.7$ MeV, which correspond to the region "A", "B", "C" and "D" of Fig. 6.4,respectively.

The energy distributions of differential cross sections for above four regions are shown in Fig. 6.8, and analyzing power in Fig. 6.9. As mentioned in Sec. 6.2 and shown in Fig. 6.2, the zero recoil point is not included in this setting for the higher excited state. Actually, the minimum recoil-momentum values accessed by this setting depend on the separation energies. On the top of each plot in these figures, the recoil momentum values are given.

It is emphasized here, that a clear dip is found in the cross section plot "A" and no dips are observed in the tail region of the same peak, plot "B".

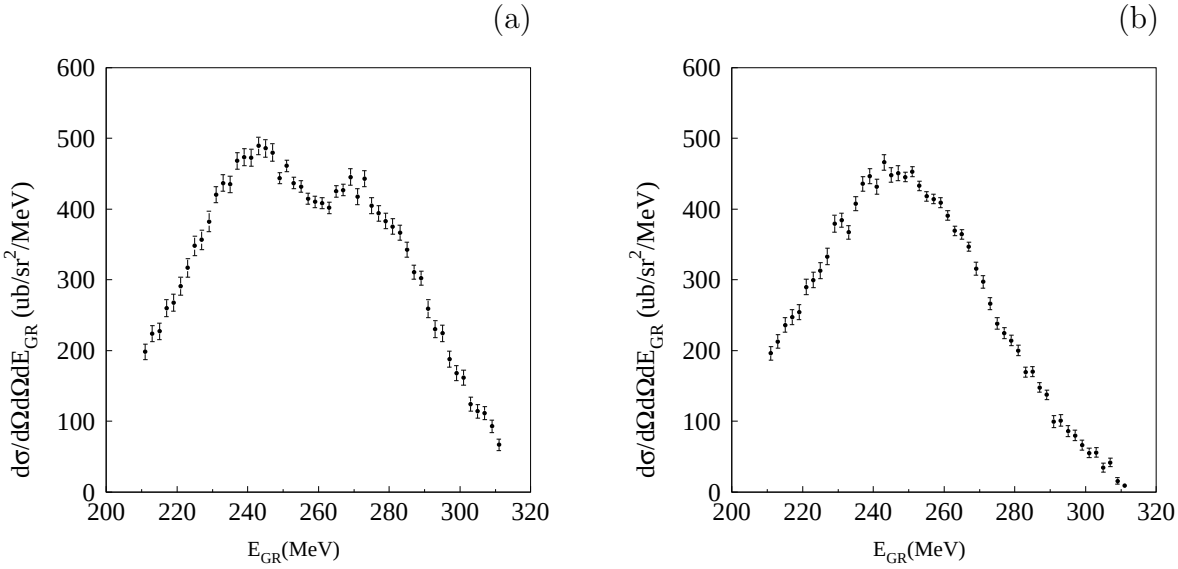

Figure 6.6: The distributions of differential cross sections: (a)Energy distribution of the lower excitation state from ^{6}Li(p,2p) reaction, where the integration range is over from $4.2 < E_{\rm sep} < 18.2$ (MeV). (b)Energy distribution of the upper excitation state from ^{6}Li(p,2p) reaction, where the integration range is over from $21.5 < E_{\rm sep} < 28.7$ (MeV).

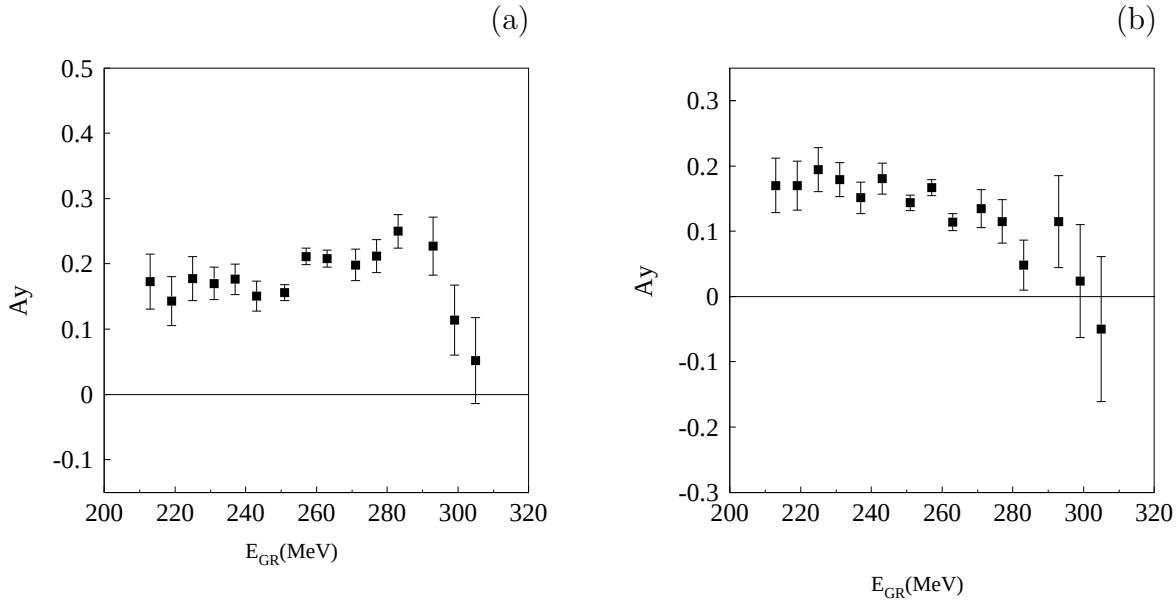

Figure 6.7: The distributions of A_y's: (a)Energy distribution of the lower excitation state from ^{6}Li(p,2p) reaction, where the integration range is over from $4.2 < E_{\rm sep} < 18.2$ MeV. (b)Energy distribution of the upper excitation state from ^{6}Li(p,2p) reaction, where the integration range is over from $21.5 < E_{\rm sep} < 28.7$ MeV.

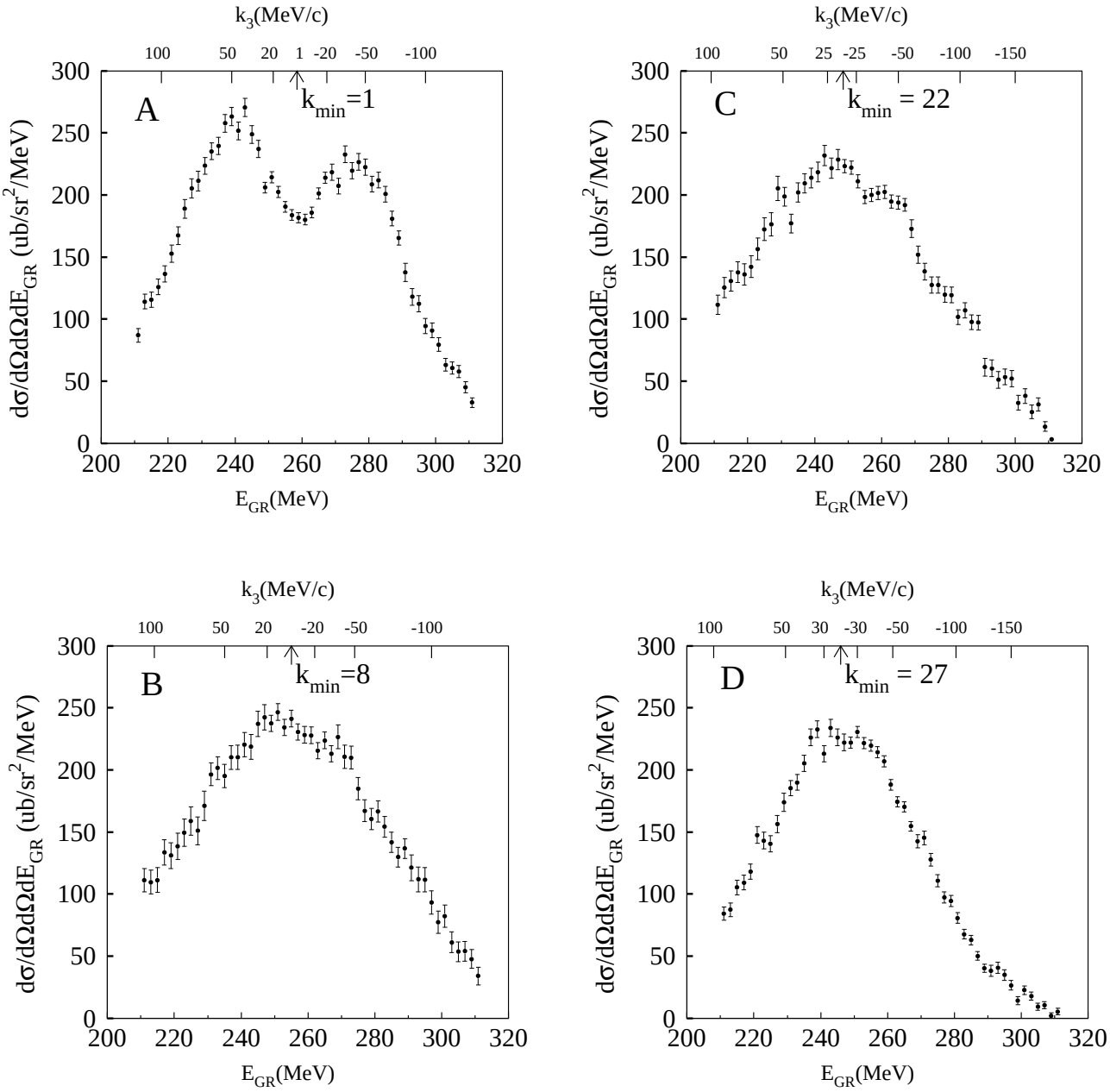

Figure 6.8: The distributions of differential cross sections for the separation energy region dependence: "A", "B", "C" and "D" are integration regions over separation energies in Fig. 6.4. Energy correlations correspond to the recoil momentum dependences like as upper side in each figure, where the minimum momentum values are different from separation energies.

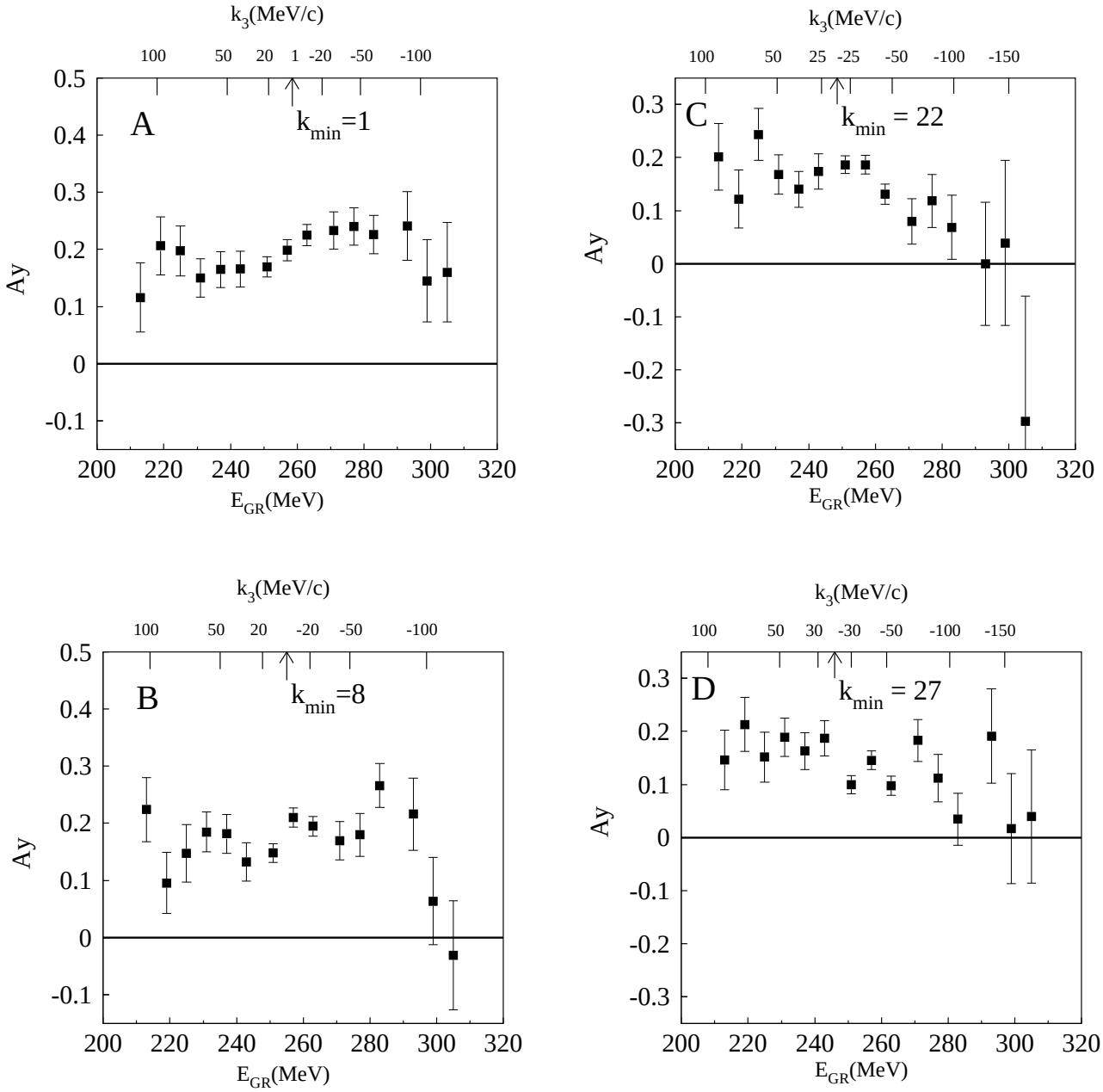

Figure 6.9: The distributions of A_y's for the separation energy region dependence: "A", "B", "C" and "D" are integration regions over separation energies in Fig. 6.4. The recoil momenta corresponded to the kinetic energies are written on the upper sides.

6.2.1 Comparisons with Calculations

The experimental results were compared with the DWIA calculations in the same way as described in Chap. 5. However, because the global optical potential is not safely extended to lower mass region then A=12 and because the Dirac-Hartree bound state wave function is consistent with this optical potential, only the method "TIMORA" based on the relativistic Hartree model was used.

Even though the data are taken by changing the detection energy of the outgoing protons, we use the same optical potential parameters for all of these DWIA calculations. It is confirmed that the use of energy dependent parameters for the optical potential cause no meaningful deviations in the calculations. The non-locality correction is applied for the calculations.

Since a clear dip is found in the region "A", and the cross section at the dip minimum is significantly large, we tried to reproduce this cross section data with incoherent sum of $1s_{1/2}$ knockout and $1p_{3/2}$ knockout. Then, as shown in Fig. 6.10 A, a reasonably good fit was obtained without changing any parameters used in the calculation except two S-factors. For the region "B", which is a tail region belong to the same peak as "A", we also tried to fit the data by using the same kinds of knockout calculations. the result gives a reasonable fit again with a small amount of $1p_{3/2}$ strength. For region "C" and "D", the cross section are simply reproduced by using $1s_{1/2}$ knockout only. It is mentioned here that these DWIA calculations for "C"a and "D"are similar shape of cross section as PWIA calculations as shown in Fig. 6.11. The S-factors used in these calculations are summarized in Table 6.1.

For analyzing power, all the calculation mentioned above reproduce the data to some extent, except for the PWIA calculations.

6.2.2 Comparison with Electron Scattering

Lanen *et al.* reported on their experimental studies for ^{6}Li$(e, e'p)^5$He reaction [76, 77, 78]. They compared the data with a calculation based on the cluster model for the target ^{6}Li

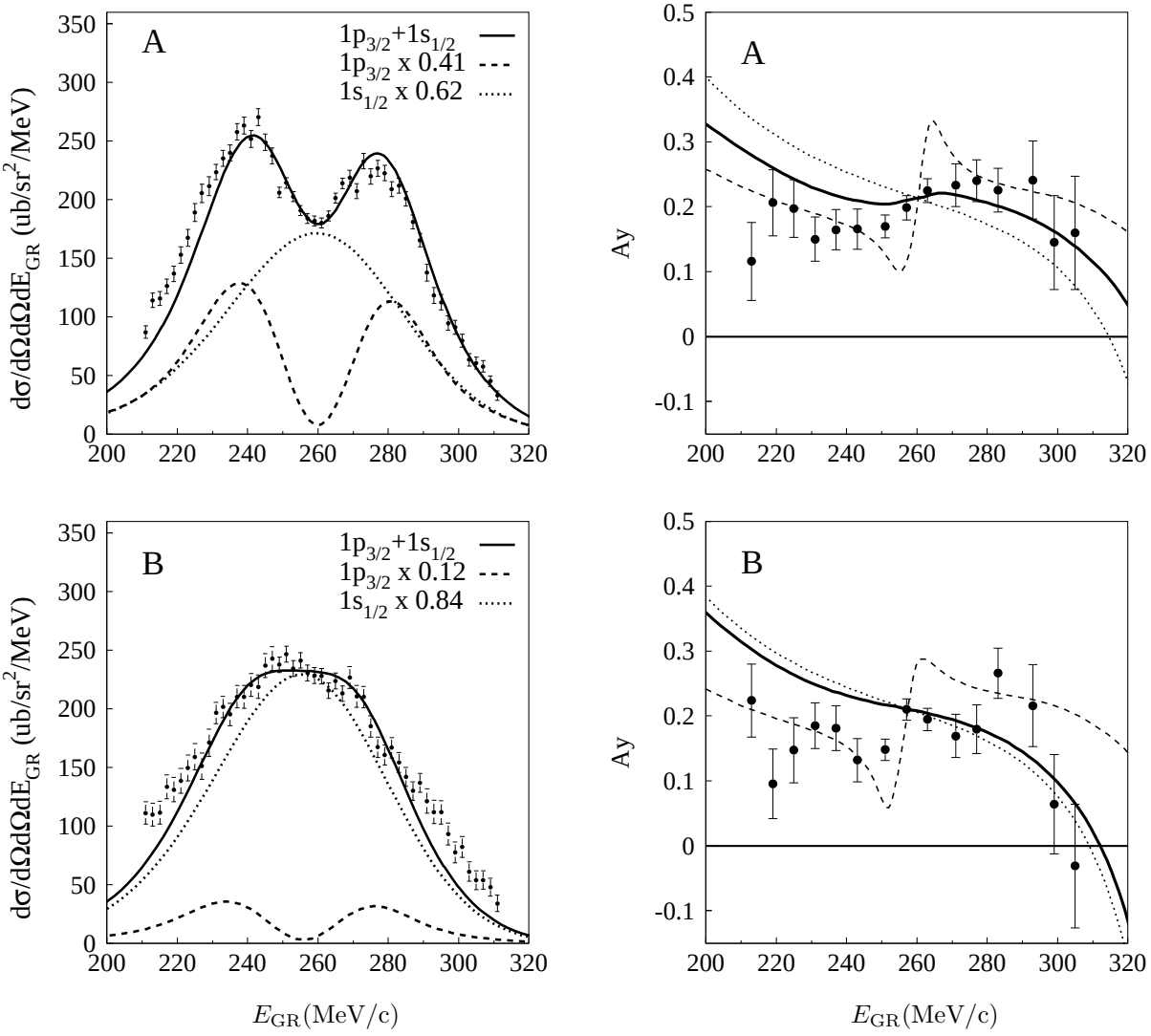

Figure 6.10: The energy distributions of differential cross section and A_y for the lower excitation state from ^{6}Li$(p, 2p)$ reaction. The integration range are "A":$4.2 < E_{\rm sep} < 5.6$ MeV and "B":$5.6 < E_{\rm sep} < 18.2$. The curves are DWIA results for knockout from the orbits indicated in this figure.

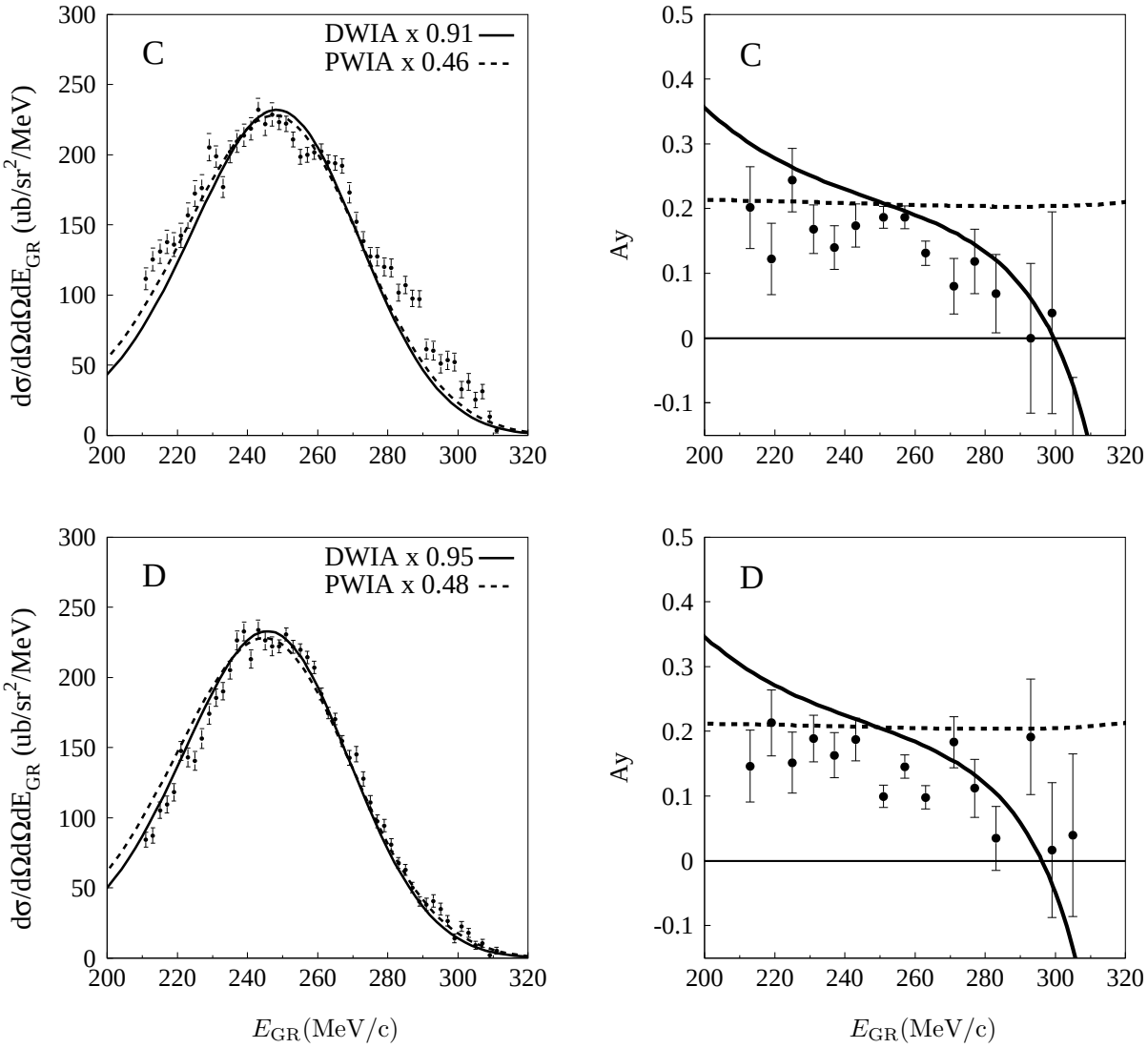

Figure 6.11: The energy distributions of differential cross section and A_y for the lower excitation state from ^{6}Li$(p, 2p)$ reaction. The integration range are "C":$21.5 < E_{\rm sep} < 22.9$ MeV and "D":$22.9 < E_{\rm sep} < 28.7$. The curves are DWIA results for knockout from the orbits indicated in this figure.

Table 6.1: Strength of states by incoherent sums

	state		E_{sep} (MeV)
region	$1p_{3/2}$	$1s_{1/2}$	
lower state region			
A	0.41	0.62	4.2 – 5.6
min.– max.	0.35 – 0.47	0.59 – 0.65	
B	0.12	0.84	5.6 – 18.2
$(\chi^2/N)_{min} \times 2$	0.04 – 0.19	0.79 – 0.90	
(A+B)	(0.53	1.47)	4.2 – 18.2
upper state region			
C		0.91	21.5 – 22.9
$(\chi^2/N)_{min} \times 2$		0.84 – 0.98	
D		0.95	22.9 – 28.7
$(\chi^2/N)_{min} \times 2$		0.90 – 0.99	
(C+D)		(1.86)	21.5 – 28.7
All	0.53	3.32	

nuclei and obtained a good fit as shown in the right panel of Fig. 6.12. The data shown are similar ones as the data "A" of the present $(p, 2p)$ study. Since it is difficult for us to perform similar calculations based on the cluster model [79], we compared our data with their $(e, e'p)$ data directly.

The other result deduced from the comparison of separation energy spectra taken with $(p, 2p)$ reaction and $(e, e'p)$ reaction for ^{12}C target as shown in Fig. 6.13. The $5/2^-$ at an excitation energy of 4.445MeV of the residual ^{11}B nucleus is not a single-hole dominant state, then, the cross sections of quasi-free proton knockout reaction are predicted to be much small. The left panel of the figure is the spectrum of the $(e, e'p)$ reaction and the right panel of the figure is the spectrum of the $(p, 2p)$ reaction. The ratio of the $5/2^-$ peak to other major state peaks are similar between of two reactions.

The comparison is given in the same figure. As is seen, those two data are fairly similar, in dip depth and peal separation, as shown. This similarity imply that the $(p, 2p)$ reactions at this energy provide a good spectroscopic tool, comparable as $(e, e'p)$reactions.

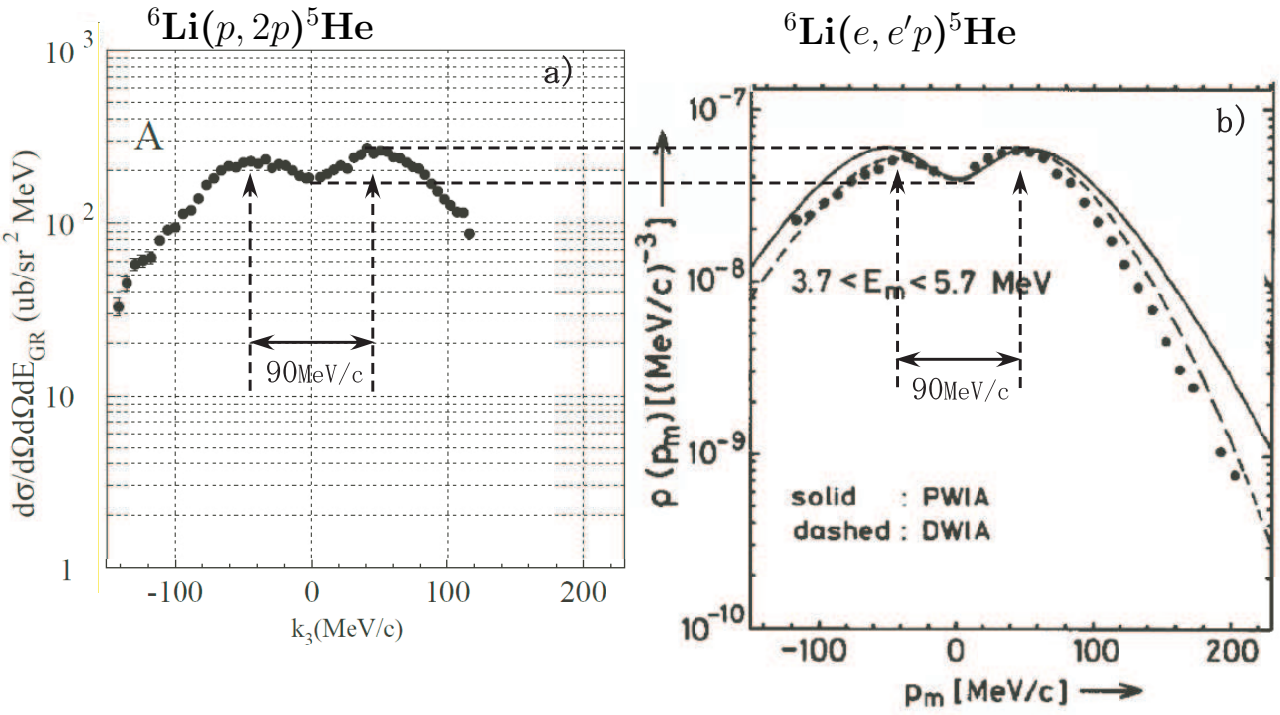

Figure 6.12: The comparison of recoil momentum distributions of the cross section for ^{6}Li$(\vec{p}, 2p)^5$He and ^{6}Li$(e, e'p)^5$He The $(e, e'p)$ plot is taken from Ref.[78]. The integration range of the separation energies are $4.2 < E_{\rm sep} < 5.6$ and $3.7 < E_{\rm sep} < 5.7$ for the $(p, 2p)$ and the $(e, e'p)$, respectively.

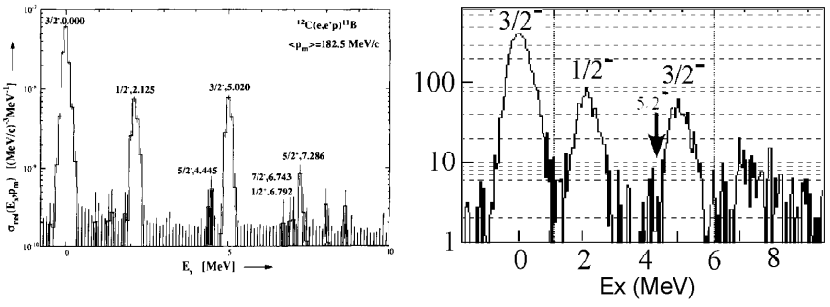

Figure 6.13: The separation energy spectra of the $(e, e'p)$ reaction (right) and the $(p, 2p)$ reaction (right) for ^{12}C target.

Chapter 7

Summary and Conclusion

In the present study, recoil-momentum distributions of the differential cross sections and analyzing powers of $(p, 2p)$ reactions on ^{40}Ca, ^{12}C and ^{6}Li targets leading to low lying discrete states of residual nuclei were measured in various kinematics. The experiment was performed at the Research Center for Nuclear Physics (RCNP) using a 392 MeV polarized proton beam in order to evaluate the experimental result as a spectroscopic probe.

To realize these $(p, 2p)$ measurements, a trigger system was newly constructed. In the system,a Field Programmable Gate Array chips, which has functional gates programmed by a computer software repeatedly, are adopted. In this system, when changing trigger logic, only re-downloading of the suitable file is required without hardware re-wiring. This trigger system is flexible to user needs in various experiments using the magnetic spectrometers, the high resolution spectrometer Grand Raiden (GR) and the Large Acceptance Spectrometer (LAS). After this development, the $(p, 2p)$ measurement, where GR and LAS are used simultaneously, can be performed with high reproducibility and reliability for reconstructing a trigger logic.

For $1d_{3/2}$ and $2s_{1/2}$ hole states of the residual ^{39}K nucleus for the ^{40}Ca target and $1p_{3/2}$ and $1p_{1/2}$ hole states of the ^{11}B nucleus for the ^{12}C target, the recoil momentum distributions of differential cross sections and A_y's are fairly well reproduced by DWIA calculations, where the reaction mechanism is assumed to be single-step. In the case of

the ^{12}C target, $1p_{3/2}$ and $1p_{1/2}$ knockout data show significant difference of A_y, that is a j-dependence, and calculations reproduce the experimental results. Spectroscopic factors (S-factors) for the four states were derived from normalization of the DWIA calculations to experimental data. Ambiguities of S-factors were quantitatively estimated as $\pm 6\%$ $\sim \pm 15\%$ error bar from the fitting for all of kinematical conditions. These uncertainties are comparable to those of results from $(e, e'p)$ reactions. For these calculations, there is a large dependence of absolute estimations on the theoretical models, such as optical potentials and non-locality corrections. The S-factors from one of calculations, where the global Dirac and Schrödinger equivalent optical potential for scattering, the solution of the phase shift analysis by Arndt for the NN t-matrix, the Woods-Saxon well potentials with same parameters of $(e, e'p)$ reactions for the bound state wave function and with non-locality corrections were deduced to be 1.11(14), 0.52(4), 1.00(15) and 0.17(2) for $1d_{3/2}$- and $2s_{1/2}$-knockout states from ^{40}Ca and $1p_{3/2}$- and $1p_{1/2}$-knockout states from ^{12}C, respectively. These S-factor are about $60-70$ % of those deduced using $(e, e'p)$ reactions. It is also found that the S-factors for ^{40}Ca target derived from our and other $(p, 2p)$ experiments show significant dependence on incident proton energies. This suggests that further theoretical improvement, especially on treatment of the distortion effects in the DWIA calculation is required in order to extract absolute values of the S-factor from $(p, 2p)$ reactions with reliability.

For the ^{6}Li target, a precise experiment was performed. The differential cross section and A_y leading to the higher excited state of residual ^{5}He were reproduced by the DWIA calculation assuming $1s_{1/2}$ knockout. On the other, for those leading to the lower excited state, there is a discrepancy between experimental distribution of differential cross section and theoretical predictions assuming a simple $1p_{1/2}$ knockout. In a detail analysis by dividing an E_{sep} spectrum into small regions, a recoil momentum $\boldsymbol{k}_3$ dependence of the cross section shows a dip at around $\boldsymbol{k}_3 = 0$ MeV/c region where a software cut is given to limit the separation energy close to the cross section peak with 1.4 MeV width. But the minimum cross section value at the $\boldsymbol{k}_3 \sim 0$ MeV/c dip was not close to zero. The cross section gives peaks at about ± 45 MeV/c of the recoil momentum and the ratio of

the peak values to the minimum was about 3:2. These features are quite similar as a result of ^{6}Li$(e, e'p)^5$He reaction, which is reproduced by calculations assuming a cluster structure in target nucleus.

Acknowledgements

During long time after my undergraduate student days, I have received many helps and encouragements from many people. First of all, I would like to express my sincere gratitude to my supervisor, Prof. Tetsuo Noro. Since the beginning of my research career, he has continuously encouraged, advised, and supported me at every stage of this work: planning of and carrying out the experiment, and analysis. I have learned from him the knowledge of the nuclear physics, skillful and thoughtful experimental technique and attitudes to solve scientific problems.

I am grateful to Prof. Kichiji Hatanaka, who gave me opportunities to study experimental physics and supported me in the many aspects during my course of study. In the experiments of this work, he had tunned parameters of the proton beam for peak performance by his sophisticated technique.

I am gratefully acknowledge Prof. Yasuhiro Sakemi, who is not only my collaborator but also now my leader of the Detector Group of Cyclotron and Radioisotope Center (CYRIC), Tohoku University. He has continuously encouraged me to complete the doctoral dissertation and generously allowed me to do this work.

I deeply appreciate Prof. Atsushi Tamii, who provided me with valuable instructions, advises, suggestions and generous cooperation. Especially for the development of the newly Trigger System, he gave me helpful advice about electronics, circuit logic, and the data acquisition system. I specially thank Prof. Hidetoshi Akimune for appropriate advises to this development, too.

I am grateful to Prof. Harutaka Sakaguchi and Prof. Masaru Yosoi. They have instructed me experiments on nuclear physics from the basics since I was an undergraduate student.

I express many thanks to the late Dr. Masanori Kawabata, Mr. Takahide Baba, and Ms. Emi Obayashi for works for $(p, 2p)$ measurements in the early stages. Dr. M. Kawabata instructed me $(p, 2p)$ experiments, especially about electronics and analysis. Mr. T. Baba gave me valuable advises, especially for FPGA techniques. Ms. E. Obayashi supported this experimental study and helped a lot of parts in the experiment.

I would like to express my gratitude to Prof. Tomotsugu Wakasa, for precious advice and helpful discussions about experimental techniques and data analysis since I was in doctor course. He provided good control system of the experimental equipment, too.

I gratefully acknowledge to Prof. Keisuke Tamura and Prof. G. C. Hillhouse, who provided me with valuable instructions, advises and suggestions from the theoretical

point of view.

I am grateful to the scientific and technical staff at RCNP for their help and advice. My special thanks are due to Especially, the accelerator group members provided the high quality beam. I would like to express my gratitude again to Mr. Keiichi Nagayama and Mr. Michio Uraki who spent a long time helping me in the technical and engineering aspects.

I would like to thank all other members of the RCNP-R14/R56 experiments; Mr. S. Asaji, Dr. H. Fujimura, Dr. K. Fujita, Mr. Y. Hagiwara, Dr. T. Ishikawa, Dr. M. Itoh, Dr. T. Ishida, Dr. T. Kawabata, Dr. Y. Maeda, the late Dr. N. Matsuoka, Prof. H. Sakaguchi, Prof. Y. Sakemi, Dr. Y. Shimizu, Dr. Y. Shimbara, Dr. H. Takeda, Ms. T. Taki, Prof. K. Tamura, Dr. Y. Tameshige, Prof. A. Tamii, Dr. S. Terashima, Dr. M. Uchida, Dr. M. Yoshimura, Mr. T. Yonemura, Prof. M. Yosoi, Dr. Y. Yasuda, and Prof. T. Wakasa. The success of the experiments is due to the contributions and collaborations of all members.

I thank also Prof. H. Akimune, Dr. K. Takahisa, Dr. I. Daito, and Dr. J. Kamiya for helpful cooperation in the another work of $(p, 2p)$ experiment (RCNP-E98). I would also like to thank Prof. M. Nomachi, Dr. Y. Sugaya and Dr. K. Yasuda. They and above all collaborators joined many other experiments together with me and I enjoyed working together.

I spent more than eight years as a member of the experimental nuclear physics group of the RCNP, Osaka University. It has been a great pleasure to spend much time with graduate students studying in RCNP. They are the good researcher, helpful adviser and nice friends at the same time. Nothing is so precious as the period I spent with them.

I am grateful to all members of the Detector Group of CYRIC for a lot of helps and discussions. I specially thank Dr. M. Itoh, who helped me a great deal in my working.

I am much obliged to Dr. Y. Yamada, Dr. M. Dozono, Mr. H. Takeda, Mr. Y. Nagasue, Mr. H. Tanabe, Mr. T. Imamura, Mr. S. Kuroita and Mr. .Y.Matsuda for your help and kindness, especially, when I stayed in Fukuoka.

Many figures in the present work for the experimental equipment are based on those illustrated by Prof. M. Yosoi, Prof. H. Akimune, Prof. A. Tamii, Prof. T. Kawabata and Dr. M. Uchida. I thank them again for their beautiful illustrations.

I am deeply grateful to the late Katsunori Nishioka and Takeshi Koyanagi for your friendship for over twenty years. I shall never forget your kindness as long as I live.

Finally, I would like to express my great thanks to my parents and brother for their patience and continuous supports during all my life.

Appendix A

Data Tables

For ^{40}Ca and ^{12}C targets, the experimental data are refered in Obayashi's master thesis [56]. For ^{6}Li targets, for the experiments in Chap. 5 and Chap. 6, all of the data were analyzed in the present work and are listed in the tables A.1– A.6.

Table A.1: Differential cross sections and analyzing power of the lower excited state for ^{6}Li$(p, 2p)^{5}$He reactions

	θ_{LAS} (deg)	$\boldsymbol{k}_3$ (MeV/c)	$\frac{\mathrm{d}\sigma}{\mathrm{d}\Omega_1\mathrm{d}\Omega_2\mathrm{dE_{GR}}} \pm \Delta$ (μb/sr^2 MeV)		A_y	$\pm\Delta Ay$
	kinematics series-①					
1	25.5	-218.4	5.92	0.18	-0.040	0.063
2	30.0	-179.6	17.68	0.21	0.028	0.026
3	35.0	-135.8	56.29	0.52	0.060	0.020
4	37.5	-113.8	102.45	0.90	0.073	0.019
5	40.0	-91.7	148.68	0.47	0.092	0.007
6	42.5	-69.7	218.04	1.78	0.105	0.017
7	45.0	-48.0	264.61	1.20	0.158	0.010
8	47.5	-27.5	273.85	2.27	0.090	0.018
9	50.0	-15.0	305.21	1.61	0.149	0.011
10	52.5	26.7	301.01	2.97	0.124	0.021
11	55.0	47.0	282.91	0.96	0.178	0.007
12	60.0	90.7	179.38	0.75	0.235	0.009
13	65.0	134.8	79.56	0.56	0.275	0.014
14	70.0	178.6	27.83	0.23	0.338	0.017
15	75.0	221.7	9.30	0.16	0.289	0.035

For all kinematics with E_{GR}=250MeV, θ_{GR}=32.5°

Table A.2: Differential cross sections and analyzing power of the upper excited state for ^{6}Li$(p, 2p)^5$He reactions

	θ_{LAS} (deg)	$\boldsymbol{k}_3$ (MeV/c)	$\frac{\mathrm{d}\sigma}{\mathrm{d}\Omega_1 \mathrm{d}\Omega_2 \mathrm{dE}_{\mathrm{GR}}} \pm \Delta$ (μb/sr^2 MeV)		A_y	$\pm\Delta Ay$
	kinematics series-①					
1	25.5	-218.4	11.42	0.22	-0.091	0.042
2	30.0	-179.6	24.78	0.26	-0.106	0.022
3	35.0	-135.8	62.84	0.58	-0.064	0.020
4	37.5	-113.8	107.46	0.97	-0.017	0.020
5	40.0	-91.7	139.78	0.45	0.009	0.007
6	42.5	-69.7	210.62	1.82	0.030	0.019
7	45.0	-48.0	261.07	1.17	0.052	0.009
8	47.5	-27.5	311.79	2.49	0.049	0.017
9	50.0	-15.0	341.02	1.72	0.138	0.010
10	52.5	26.7	325.93	3.21	0.116	0.021
11	55.0	47.0	292.89	1.00	0.175	0.007
12	60.0	90.7	181.66	0.77	0.236	0.009
13	65.0	134.8	92.45	0.64	0.286	0.014
14	70.0	178.6	39.37	0.30	0.348	0.016
15	75.0	221.7	16.76	0.22	0.381	0.027

For all kinematics with E_{GR}=250MeV, θ_{GR}=32.5°

Table A.3: Differential cross sections for lower excited region of ^{6}Li$(p,2p)^{5}$He

		$4.2 < E_{sep} < 5.6$ MeV region “A”			$5.6 < E_{sep} < 18.2$ MeV region “B”			$4.2 < E_{sep} < 18.2$ MeV region “A+B”		
	E_{GR} (MeV)	$\boldsymbol{k}_3$ (MeV/c)	$\frac{\mathrm{d}\sigma}{\mathrm{d}\Omega_1\mathrm{d}\Omega_2\mathrm{dE_{GR}}}$ (μb/sr^2/MeV)	$\pm\ \Delta$	$\boldsymbol{k}_3$ (MeV/c)	$\frac{\mathrm{d}\sigma}{\mathrm{d}\Omega_1\mathrm{d}\Omega_2\mathrm{dE_{GR}}}$ (μb/sr^2/MeV)	$\pm\ \Delta$	$\boldsymbol{k}_3$ (MeV/c)	$\frac{\mathrm{d}\sigma}{\mathrm{d}\Omega_1\mathrm{d}\Omega_2\mathrm{dE_{GR}}}$ (μb/sr^2/MeV)	$\pm\ \Delta$
l-1	211.0	116.3	86.92	5.37	108.1	111.10	9.47	108.1	198.00	10.88
l-2	213.0	111.6	114.10	5.95	103.4	109.60	9.62	103.4	223.60	11.31
l-3	215.0	107.0	115.70	6.03	98.7	111.30	9.85	98.7	227.00	11.55
l-4	217.0	102.3	126.00	6.30	94.0	133.50	10.20	94.0	259.60	11.99
l-5	219.0	97.7	136.60	6.52	89.2	131.00	10.30	89.2	267.70	12.19
l-6	221.0	93.0	152.70	6.89	84.5	138.40	10.67	84.5	291.00	12.70
l-7	223.0	88.3	167.30	7.15	79.8	149.50	10.96	79.8	316.80	13.09
l-8	225.0	83.6	188.90	7.56	75.0	158.90	11.29	75.0	347.80	13.59
l-9	227.0	78.9	205.30	7.89	70.2	151.00	11.31	70.2	356.30	13.79
l-10	229.0	74.2	211.40	7.98	65.5	171.00	11.75	65.5	382.40	14.21
l-11	231.0	69.4	223.50	6.64	60.7	196.50	9.15	60.7	420.00	11.31
l-12	233.0	64.7	235.20	6.77	55.9	201.50	9.28	55.9	436.70	11.49
l-13	235.0	59.9	239.70	6.85	51.1	195.10	9.34	51.1	434.70	11.58
l-14	237.0	55.1	257.80	7.09	46.2	210.20	9.58	46.2	468.00	11.92
l-15	239.0	50.3	263.20	7.18	41.4	210.20	9.67	41.4	473.40	12.05
l-16	241.0	45.5	251.70	7.04	36.6	220.50	9.77	36.6	472.20	12.05
l-17	243.0	40.7	270.50	7.26	31.8	218.70	9.93	31.8	489.20	12.30
l-18	245.0	35.8	248.80	7.02	27.0	237.00	10.13	27.0	485.80	12.33
l-19	247.0	31.0	237.20	6.90	22.3	242.60	10.18	22.3	479.80	12.29
l-20	249.0	26.1	206.00	4.41	17.6	237.50	6.67	17.6	443.50	7.99
l-21	251.0	21.2	214.30	4.47	13.2	246.70	6.74	13.2	461.00	8.09
l-22	253.0	16.3	202.50	4.37	9.5	234.30	6.69	9.5	436.80	7.99
l-23	255.0	11.3	190.60	4.28	7.4	241.30	6.75	7.4	431.80	7.99
l-24	257.0	6.4	183.90	4.23	-8.4	230.60	6.68	-8.4	414.60	7.91
l-25	259.0	1.8	181.70	4.21	-11.8	228.30	6.67	-11.8	410.00	7.89
l-26	261.0	-3.9	180.20	4.20	-16.1	227.80	6.68	-16.1	408.00	7.89
l-27	263.0	-8.9	185.90	4.26	-20.9	215.60	6.62	-20.9	401.50	7.87
l-28	265.0	-13.9	201.20	4.39	-25.8	223.80	6.70	-25.8	425.00	8.01
l-29	267.0	-19.0	213.80	4.50	-30.9	213.10	6.59	-30.9	426.90	7.98
l-30	269.0	-24.1	218.50	6.51	-36.0	226.70	9.43	-36.0	445.20	11.46
l-31	271.0	-29.3	207.20	6.38	-41.2	210.50	9.32	-41.2	417.70	11.29
l-32	273.0	-34.4	232.80	6.74	-46.5	210.00	9.27	-46.5	442.80	11.46
l-33	275.0	-39.7	219.70	6.55	-51.8	185.00	9.00	-51.8	404.70	11.13
l-34	277.0	-44.9	226.70	6.62	-57.1	167.20	8.78	-57.1	393.90	10.99
l-35	279.0	-50.2	222.60	6.57	-62.6	160.50	8.62	-62.6	383.10	10.83
l-36	281.0	-55.6	208.70	6.36	-68.0	166.70	8.59	-68.0	375.30	10.69
l-37	283.0	-60.9	212.00	6.41	-73.5	154.20	8.38	-73.5	366.20	10.55
l-38	285.0	-66.3	200.70	6.26	-79.1	141.80	8.17	-79.1	342.50	10.29
l-39	287.0	-71.8	181.00	5.97	-84.7	129.80	7.99	-84.7	310.80	9.97
l-40	289.0	-77.3	165.40	5.71	-90.4	136.80	7.92	-90.4	302.20	9.77
l-41	291.0	-82.9	137.60	7.22	-96.1	121.20	10.35	-96.1	258.90	12.62
l-42	293.0	-88.5	118.00	6.71	-101.9	111.90	10.01	-101.9	229.80	12.05
l-43	295.0	-94.1	112.40	6.56	-107.8	111.60	9.82	-107.8	224.10	11.81
l-44	297.0	-99.8	94.48	6.08	-113.7	93.12	9.38	-113.7	187.60	11.18
l-45	299.0	-105.6	90.83	5.95	-119.7	77.26	8.94	-119.7	168.10	10.74
l-46	301.0	-111.4	79.45	5.58	-125.8	82.22	8.97	-125.8	161.70	10.56
l-47	303.0	-117.3	63.23	5.18	-131.9	61.09	8.42	-131.9	124.30	9.89
l-48	305.0	-123.3	60.57	5.00	-138.1	53.53	8.07	-138.1	114.10	9.49
l-49	307.0	-129.3	57.70	4.88	-144.5	53.89	7.93	-144.5	111.60	9.31
l-50	309.0	-135.4	45.13	4.52	-150.9	47.63	7.58	-150.9	92.76	8.83
l-51	311.0	-141.6	32.76	3.90	-157.4	33.96	7.15	-157.4	66.72	8.15

For all kinematics with θ_{GR}=32.21° , θ_{LAS}=51.62°

Table A.4: Differential cross sections for upper excited region of ^{6}Li$(p,2p)^5$He

	$21.5 < E_{sep} < 22.9$ MeV region "C"			$22.9 < E_{sep} < 28.7$ MeV region "D"			$21.5 < E_{sep} < 28.7$ MeV region "C+D"		
	E_{GR} (MeV)	$\boldsymbol{k}_3$ (MeV/c)	$\frac{\mathrm{d}\sigma}{\mathrm{d}\Omega_1\mathrm{d}\Omega_2\mathrm{dE_{GR}}} \pm \Delta$ (μb/sr^2/MeV)	$\boldsymbol{k}_3$ (MeV/c)	$\frac{\mathrm{d}\sigma}{\mathrm{d}\Omega_1\mathrm{d}\Omega_2\mathrm{dE_{GR}}} \pm \Delta$ (μb/sr^2/MeV)		$\boldsymbol{k}_3$ (MeV/c)	$\frac{\mathrm{d}\sigma}{\mathrm{d}\Omega_1\mathrm{d}\Omega_2\mathrm{dE_{GR}}} \pm \Delta$ (μb/sr^2/MeV)	
u-1	211.0	95.4	111.60	7.85	91.4	84.28	5.32	91.4	195.90	9.48
u-2	213.0	90.7	125.40	8.05	86.8	87.30	5.46	86.8	212.70	9.73
u-3	215.0	86.0	130.80	8.26	82.1	105.30	5.88	82.1	236.10	10.13
u-4	217.0	81.3	137.80	8.41	77.5	109.30	6.04	77.5	247.00	10.36
u-5	219.0	76.6	136.00	8.53	72.9	118.10	6.19	72.9	254.00	10.54
u-6	221.0	72.0	142.30	8.68	68.4	147.50	6.76	68.4	289.80	11.00
u-7	223.0	67.3	156.60	8.89	63.9	143.00	6.71	63.9	299.60	11.14
u-8	225.0	62.7	172.40	9.26	59.4	140.50	6.72	59.4	312.90	11.44
u-9	227.0	58.1	176.30	9.39	55.1	156.40	6.98	55.1	332.70	11.70
u-10	229.0	53.6	205.30	9.84	50.8	173.90	7.37	50.8	379.20	12.29
u-11	231.0	49.1	198.70	7.64	46.7	185.50	6.06	46.7	384.20	9.76
u-12	233.0	44.7	177.00	7.47	42.7	190.00	6.19	42.7	367.00	9.70
u-13	235.0	40.4	201.90	7.75	39.0	205.30	6.38	39.0	407.30	10.04
u-14	237.0	36.3	209.40	7.82	35.6	226.30	6.63	35.6	435.70	10.25
u-15	239.0	32.5	213.80	7.93	32.6	232.70	6.76	32.6	446.50	10.42
u-16	241.0	29.0	218.50	8.00	30.3	213.00	6.49	30.3	431.50	10.30
u-17	243.0	26.0	231.90	8.17	28.6	233.90	6.78	28.6	465.80	10.62
u-18	245.0	23.8	221.70	8.16	27.9	226.30	6.70	27.9	448.10	10.56
u-19	247.0	22.5	228.60	8.23	-28.1	222.20	6.65	-28.1	450.80	10.58
u-20	249.0	-22.4	223.20	5.41	-29.3	222.10	4.51	-29.3	445.30	7.05
u-21	251.0	-23.5	222.00	5.43	-31.3	230.60	4.60	-31.3	452.60	7.11
u-22	253.0	-25.6	210.90	5.33	-34.1	221.70	4.52	-34.1	432.60	6.99
u-23	255.0	-28.6	198.40	5.26	-37.4	219.50	4.50	-37.4	417.80	6.92
u-24	257.0	-32.1	199.90	5.26	-41.2	214.30	4.45	-41.2	414.20	6.89
u-25	259.0	-36.2	201.80	5.27	-45.4	207.00	4.39	-45.4	408.80	6.86
u-26	261.0	-40.5	202.50	5.26	-49.8	188.10	4.22	-49.8	390.60	6.74
u-27	263.0	-45.1	194.70	5.22	-54.4	174.50	4.08	-54.4	369.20	6.62
u-28	265.0	-50.0	194.00	5.22	-59.3	170.20	4.04	-59.3	364.10	6.60
u-29	267.0	-54.9	192.00	5.18	-64.3	154.60	3.87	-64.3	346.60	6.47
u-30	269.0	-60.0	172.90	7.20	-69.4	142.60	5.43	-69.4	315.50	9.02
u-31	271.0	-65.2	152.00	6.95	-74.7	145.20	5.45	-74.7	297.20	8.83
u-32	273.0	-70.5	138.40	6.70	-80.0	127.70	5.17	-80.0	266.00	8.46
u-33	275.0	-75.9	127.30	6.51	-85.5	110.80	4.91	-85.5	238.20	8.15
u-34	277.0	-81.4	127.30	6.56	-91.0	97.24	4.60	-91.0	224.50	8.01
u-35	279.0	-87.0	119.90	6.30	-96.7	94.35	4.53	-96.7	214.20	7.76
u-36	281.0	-92.6	119.40	6.36	-102.4	80.62	4.26	-102.4	200.00	7.65
u-37	283.0	-98.4	101.60	6.04	-108.3	67.69	3.99	-108.3	169.30	7.24
u-38	285.0	-104.2	107.10	6.05	-114.2	62.86	3.85	-114.2	169.90	7.17
u-39	287.0	-110.1	97.49	5.88	-120.2	50.18	3.59	-120.2	147.70	6.89
u-40	289.0	-116.1	97.13	5.84	-126.3	40.20	3.31	-126.3	137.30	6.71
u-41	291.0	-122.1	61.25	7.00	-132.5	38.14	4.43	-132.5	99.38	8.29
u-42	293.0	-128.3	60.31	6.80	-138.8	40.64	4.40	-138.8	100.90	8.10
u-43	295.0	-134.5	51.02	6.55	-145.2	34.80	4.25	-145.2	85.82	7.81
u-44	297.0	-140.9	53.42	6.49	-151.8	26.50	3.76	-151.8	79.92	7.50
u-45	299.0	-147.3	52.01	6.35	-158.4	13.98	3.24	-158.4	65.99	7.12
u-46	301.0	-153.9	32.61	5.89	-165.2	22.48	3.57	-165.2	55.09	6.89
u-47	303.0	-160.5	37.98	5.91	-172.1	17.89	3.29	-172.1	55.87	6.77
u-48	305.0	-167.3	25.25	5.44	-179.2	9.08	2.91	-179.2	34.33	6.16
u-49	307.0	-174.2	31.20	5.17	-186.4	10.49	2.85	-186.4	41.68	5.90
u-50	309.0	-181.3	13.46	3.76	-193.8	2.04	2.37	-193.8	15.49	4.45
u-51	311.0	-188.5	3.29	1.80	-201.3	5.32	2.48	-201.3	8.61	3.06

For all kinematics with θ_{GR}=32.21° , θ_{LAS}=51.62°

Table A.5: Analyzing power for lower excited region of ^{6}Li$(p, 2p)^5$He

		$4.2 < E_{sep} < 5.6$ MeV region "A"			$5.6 < E_{sep} < 18.2$ MeV region "B"			$4.2 < E_{sep} < 18.2$ MeV region "A+B"		
	E_{GR}	$\boldsymbol{k}_3$	$A_y \pm \Delta A_y$		$\boldsymbol{k}_3$	$A_y \pm \Delta A_y$		$\boldsymbol{k}_3$	$A_y \pm \Delta A_y$	
	(MeV)	(MeV/c)			(MeV/c)			(MeV/c)		
la-1	213.0	111.6	0.116	0.060	103.4	0.224	0.056	103.4	0.173	0.042
la-2	219.0	97.7	0.206	0.051	89.2	0.095	0.053	89.2	0.143	0.038
la-3	225.0	83.6	0.197	0.044	75.0	0.147	0.050	75.0	0.177	0.034
la-4	231.0	69.4	0.150	0.034	60.7	0.185	0.035	60.7	0.170	0.025
la-5	237.0	55.1	0.165	0.031	46.2	0.181	0.034	46.2	0.176	0.024
la-6	243.0	40.7	0.166	0.031	31.8	0.132	0.034	31.8	0.151	0.023
la-7	251.0	21.2	0.170	0.018	13.2	0.148	0.016	13.2	0.156	0.012
la-8	257.0	6.4	0.199	0.019	-8.4	0.210	0.017	-8.4	0.211	0.013
la-9	263.0	-8.9	0.225	0.018	-20.9	0.195	0.017	-20.9	0.208	0.013
la-10	271.0	-29.3	0.233	0.033	-41.2	0.169	0.034	-41.2	0.198	0.024
la-11	277.0	-44.9	0.240	0.032	-57.1	0.180	0.037	-57.1	0.212	0.025
la-12	283.0	-60.9	0.226	0.034	-73.5	0.266	0.039	-73.5	0.250	0.026
la-13	293.0	-88.5	0.241	0.060	-101.9	0.216	0.063	-101.9	0.227	0.044
la-14	299.0	-105.6	0.145	0.072	-119.7	0.064	0.076	-119.7	0.114	0.053
la-15	305.0	-123.3	0.160	0.087	-138.1	-0.031	0.095	-138.1	0.052	0.066

For all kinematics with θ_{GR}=32.21° , θ_{LAS}=51.62°

Table A.6: Analyzing power for upper excited region of ^{6}Li$(p, 2p)^5$He

		$21.5 < E_{sep} < 22.9$ MeV region "C"			$22.9 < E_{sep} < 28.7$ MeV region "D"			$21.5 < E_{sep} < 28.7$ MeV region "C+D"		
	E_{GR}	$\boldsymbol{k}_3$	$A_y \pm \Delta A_y$		$\boldsymbol{k}_3$	$A_y \pm \Delta A_y$		$\boldsymbol{k}_3$	$A_y \pm \Delta A_y$	
	(MeV)	(MeV/c)			(MeV/c)			(MeV/c)		
ua-1	213.0	90.7	0.202	0.063	86.8	0.146	0.056	86.8	0.170	0.042
ua-2	219.0	76.6	0.122	0.055	72.9	0.213	0.051	72.9	0.170	0.037
ua-3	225.0	62.7	0.244	0.049	59.4	0.152	0.047	59.4	0.194	0.034
ua-4	231.0	49.1	0.168	0.037	46.7	0.189	0.036	46.7	0.179	0.026
ua-5	237.0	36.3	0.140	0.034	35.6	0.163	0.035	35.6	0.151	0.024
ua-6	243.0	26.0	0.174	0.033	28.6	0.187	0.033	28.6	0.181	0.024
ua-7	251.0	-23.5	0.186	0.017	-31.3	0.100	0.017	-31.3	0.144	0.012
ua-8	257.0	-32.1	0.187	0.017	-41.2	0.146	0.018	-41.2	0.167	0.012
ua-9	263.0	-45.1	0.131	0.019	-54.4	0.098	0.018	-54.4	0.114	0.013
ua-10	271.0	-65.2	0.080	0.043	-74.7	0.183	0.040	-74.7	0.134	0.029
ua-11	277.0	-81.4	0.118	0.050	-91.0	0.112	0.045	-91.0	0.115	0.033
ua-12	283.0	-98.4	0.069	0.060	-108.3	0.035	0.049	-108.3	0.048	0.038
ua-13	293.0	-128.3	-0.000	0.116	-138.8	0.191	0.089	-138.8	0.115	0.071
ua-14	299.0	-147.3	0.039	0.156	-158.4	0.017	0.104	-158.4	0.024	0.086
ua-15	305.0	-167.3	-0.297	0.236	-179.2	0.040	0.126	-179.2	-0.050	0.111

For all kinematics with θ_{GR}=32.21° , θ_{LAS}=51.62°

Appendix B

The Trigger System by Using FPGA Chips

B.1 Utilization of FPGA for Trigger System

In this section, the development work for employing a FPGA in a trigger system is described. FPGA's are used for logic circuits synchronously to the clock. But the synchronized logic circuits causes timing jitter of signals relative to actual event times. Then we have to devise some methods for applying FPGA to a trigger system. When a very high quality FPGA chip is with very high frequency clock is available, the time jitters may be negligible. But it is impractical to use such chips. We treat the signals whose leading edge is important for timing information with care particularly.

Our design concept of the system is as follows:

1. To be made for general purpose experiments, not for a specific experiment, because troubles in changing experiments decrease if it is not necessary to reconstruct hardware modules and rewire connections.

2. To have a hierarchical structure and modularize parts of circuits. Each module has additional outputs to be able to check and pursue meaningful signals.

3. To divide functionally parts into two groups. One group has outputs of parts to be needed distinct response time and the other has outputs not to be needed high resolution of time.

4. To make additional CAMAC functions convenient to use. If there are these utilities, it can be easy to change trigger conditions and outputs for scaler inputs or diagnostic outputs.

About No.1 $\sim$ 4, details are mentioned subsections. In terms of No.2, designing and programing FPGA circuits in this work, a CAD (computer-aided design) tool is used for because circuit schematics are entered into CAD to be able to imagine to arrange functional NIM modules inside a FPGA.

B.1.1 General Purpose Use

In general, one FPGA chip is used for a specific purpose and the down-load program on the chip is developed by trial and error to reach a optimized or updated program for the purpose. But we use a FPGA chip not only for one experiment but also for all experiments using spectrometers with or without other detectors. For those general purpose, the system was designed with flexibility in consideration of not only the combination of existing detectors but also combination of existing ones and future additional ones. Core parts of the system consist with three LeCroy 2366(LC 2366) ULMs, where each ULM has one FPGA chip and each ULM has each role assigned. As a result, there is a room in capacity for future additional logic. The connection between LC 2366 ULMs and other electronics was done so that even if the combination of detectors is changed it is really not necessary to rewire for electronics of both spectrometers and there are only several connections with other detectors.

B.1.2 Modularization

The program of circuits was modularized and made a nested construction. In addition, the trigger circuits designed on CAD consisted of hierarchical modules and modules on the top floor are functionally like to NIM electronics. So these CAD circuits are relatively easy to understand for people who have experienced construction with NIM electronics.

The modules those were developed and examined at once were cataloged into the program library. Using modules from the library is very useful to develop the new

other circuits and to decrease time of the development. There are a few hundred useful modules in the library, where some modules have very simple logic and others have very complicated logic.

B.1.3 Timing Adjustment

When a FPGA chip is introduced into a trigger system, it is essential to design circuits how to keep time information during propagating signals. In above section 2.2.1, there are disadvantages for time information mentioned. We must treat signals concerning timing carefully and, fortunately, there are several such signals and several derivative signals. Only common gate or common start signals for ADC and TDC modules especially have to be treated with care for timing because these signals influence the ADC and TDC data. Such a signal is called "Gate signal" in this section.

The procedure of generating "Gate signal" is as follows.

1. Before the signals for the trigger condition are inputted into FPGA modules, they are delayed and the timing are adjusted accordingly,
2. The logic circuit met the condition is made from only AND, OR ,INVERSE and these combinations. The output signal of this logic is called "A".
3. This signal "A" is shaped into the wide signal "B". This signal "B" is generated by a flip-flop but the leading edge of the flip-flop is changed by the leading edge of the signal "A".
4. If it is necessary to delay the signal "B", once "B" is send outside of the FPGA module and the signal "C" which is delayed signal generated by "B" is inputted into the FPGA module, again.

The signal "B" is enough wide to be used for other circuits and to eliminate the bug caused by a sharp hazard signal. The matter of timing information is resolved by using the leading edge of origin for the change of status and the edge is not synchronized with a clock signal. The tailing edge of the signal "B" and other signals those don't need distinct timing are synchronized with clock signals.

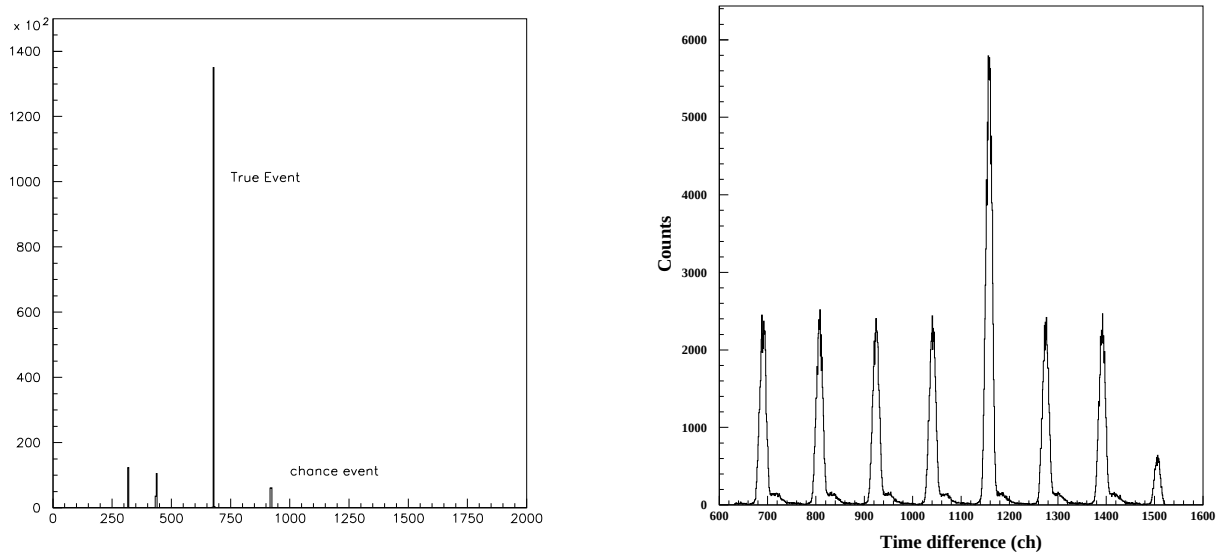

Figure B.1: Time difference of True-Chance by synchronous system(left side) and asynchronous current system(right side) to the clock.

Fig.B.1 shows that one of the result of timing adjustment. The left figure in Fig.B.1 shows the time difference of coincidence events in the past system using RF signal for the FPGA synchronized clock signal and the right figure shows that in the current system. The left figure shows simple true-chance structure, however the right shows more fine structure which has chance bumps caused by not only protons but also deuteron. The current system can easily stand comparison with the system consisted of normal NIM or CAMAC modules.

B.1.4 Application Functions for Setting Conditions

For a LC 2366 ULM, CAMAC functions can be designed and defined into FPGA chip by users. The circuits of this system are dwsigned so that some conditions, those are the coincidence gate, sampling ratios and a set of coincidence signals, are able to be changed by CAMAC functions in every designed circuits. There is an advantage that even if the trigger condition is different the same designed circuit down-loaded on a FPGA chip can be used during the same experiment without minor fine-tuning. And some outputs for scaler and diagnostic are changed by CAMAC function. For these applications, the trigger system can deal with various type experiments including minor changes.

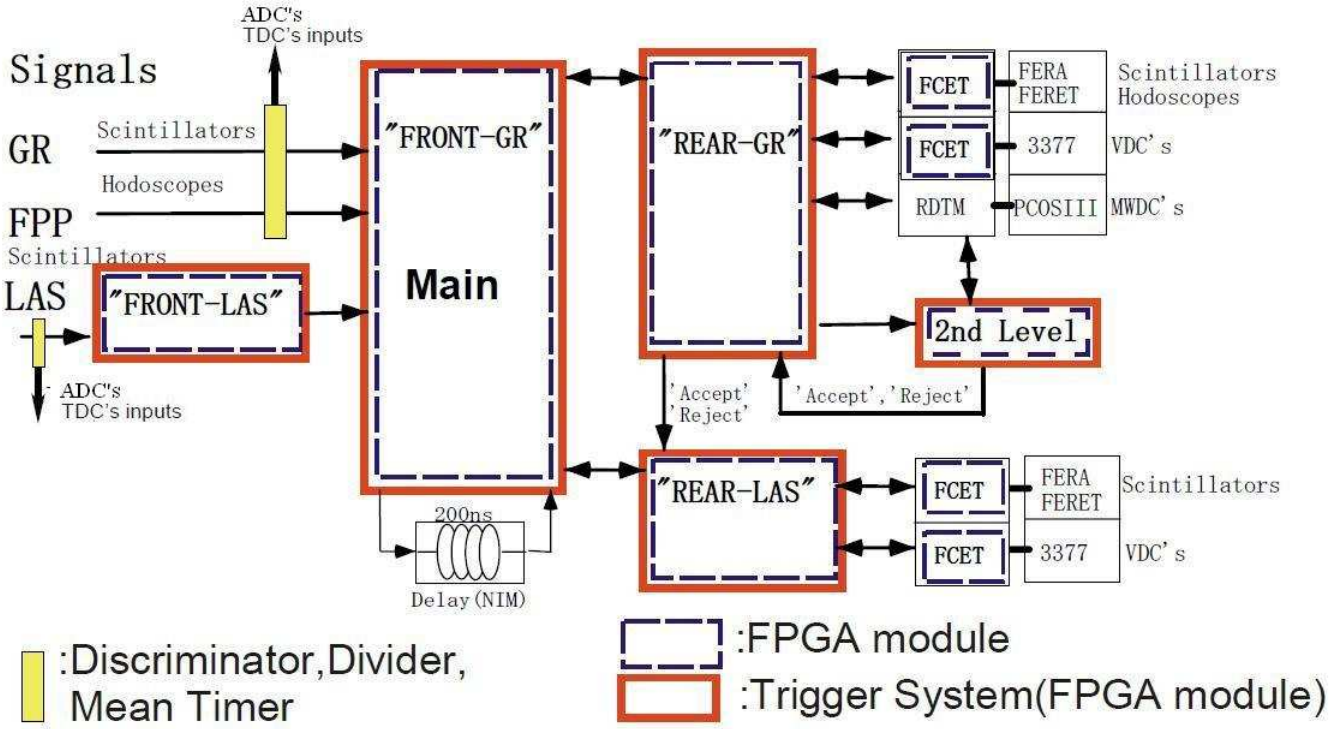

Figure B.2: Schematic configuration of "Main trigger System".

B.2 Layout of the Trigger System

The figure B.2 shows schematic layout of the trigger system, regarding hardware. In general, the trigger system is closely concerned with the data acquisition(DAQ) system. In the DAQ and the Trigger system, CAMAC functions are only used to make electric modules setup. During data taking, CAMAC functions are eliminated by using module series which are available readout system of Front end ECL BUS. This module series, which are FERA compatible series, are operated by the trigger system. This is also one reason that trigger logic is bigger and more complicated. But by using modules installed FPGA chips, we can easily treat these module series.

In this trigger system, we can use the spectrometer Grand Raiden (GR) with the Large Acceptance Spectrometer (LAS) [37, 38] and other detector sets, which are the Focal Plane Polarimeter (FPP) [39, 40], SSD's, NaI's, Liquid scintillators [41, 42] and so on. The details of the detectors on the $(p, 2p)$ experiments are described in the chapter 3.5.3.

The core of the trigger system called as “Main Trigger System” are three LC 2366 ULMs called as “Front-GR”, “Rear GR” and Rear LAS” divided functionally. The “Front-GR” has circuits where the trigger condition is defined, event selection is made and outputs for event information is generated. The “Rear GR” mainly works to access module set of FERA compatible series for the GR data include Focal Plane Polarimeter. The “Rear LAS”mainly works to access module set of FERA compatible series for LAS and additional detectors like SSD’s for target decay events.

Actually, more LC 2366 ULMs are used in the system. The circuit module defined the condition for LAS events is a LC 2366 ULM setting at near LAS(which is described as “Front-LAS” in Fig.B.2), so that we can change the condition by CAMAC functions. And each set of FERA compatible series has a LC 2366 ULM as a event tagger module. When the Focal Plane Polarimeter on the GR is used, we also need to use 2nd level trigger module which is a LC 2366 ULM.

Appendix C

Trigger System for Beam Line Polarimeters

Beam polarization is measured by using left-right or up-down asymmetry of the proton-proton scattering at the target positions for two Beam Line Polarimeters (BLP's), each consists of four pairs of scintillators. Trigger logic for each channel is shown in Fig. C.1. It is characteristic of the BLP trigger system that it has as many as 16 channels of this simple logic. In this system we use the RF signal of the cyclotron as a system clock of the Field Programmable Gate Array(FPGA) after doubling the frequency. in the FPGA. The delay in fig. 1, which is about 60 nsec delay for the beam energy E_p =392MeV, is replaced by a shift register controlled by this clock in the FPGA. The advantage of this usage is that the delay time is always the beam repetition time and no adjustment is required when the beam energy is changed. Instead, the time relation between the clock signal and input signals is tuned to avoid miscounting caused by bad timing.

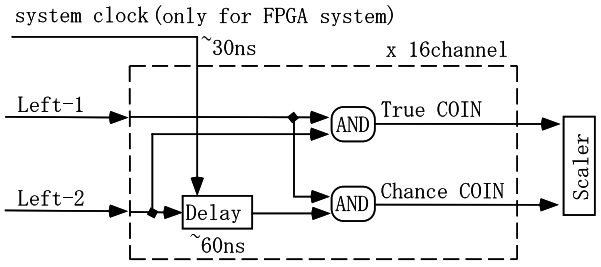

Figure C.1: Trigger logic for the BLP. Proton-proton scattering events are counted by the kinematical coincidence method. The delayed coincidence is used to estimate the accidental coincidence rate.

We used both the old and new systems at the same time and confirmed the equivalency of data of ADC and TDC, scaler values and polarization observables. After this confirmation, only the new system has been used and worked with stability.

Bibliography

[1] O. Chamberlain and E. Segrè, Phys. Rev. **87**, 81 (1952).

[2] J.B. Cladis, W.N. Hess, and B.J. Moyer, Phys. Rev. **87**, 425 (1952).

[3] J.M. Wilcox and B.J. Moyer, Phys. Rev. **99**, 875 (1955)

[4] H. Tyrèn, P. Hillman and Th.A.J. Maris, Nucl. Phys. **A7**, 10 (1958).

[5] T. Berggren, G. E. Brown and G. Jacob, Phys. Lett. **1**, 88 (1962).

[6] T. Berggren and H. Tyren, Annu. Rev. Nucl. Sci. **16**, 153 (1966).

[7] H. Tyrén, S. Kullander, O. Sundberg, R. Ramachandran, and P. Isacsson, Nucl. Phys. **79**, 321 (1966).

[8] A. N. James, P. T. Andrews, P. Kirkby, and B.G. Lowe, Nucl. Phys. **138**, 145 (1969).

[9] G. Landaud, J. Yonnet, S. Kullander, F. Lemeilleuur, P.U. Renberg, B. Fagerström, A. Yohansson, and G. Tibell, Nucl. Phys. **173**, 337 (1971).

[10] S. Kullander, F. Lemeilleuur, P.U. Renberg, G. Landaud, J. Yonnet, B. Fagerström, A. Johansson, and G. Tibell, Nucl. Phys. **173**, 357 (1971).

[11] G. Jacob and Th.A.J. Maris, Rev. Mod. Phys. **45**, 6 (1973), and references therein.

[12] P. Kitching, W.J. McDonald, Th.A.J. Maris, and C.A.Z. Vasconcellos, in *Advances in Nuclear Physics*, edited by J.W. Negele and E. Vogt (Plenum Press, New York, 1985), Vol. 15, p. 43, and references therein.

[13] S. Fullani and J. Mougey, in *Advances in Nuclear Physics*, edited by J.W. Negele and E. Vogt (Plenum Press, New York, 1984), Vol. 14, p. 1, and references therein.

[14] J. Kelly, in *Advances in Nuclear Physics*, edited by J.W. Negele and E. Vogt (Plenum Press, New York, 1996), Vol. 23, p. 75, and references therein.

[15] A.E.L. Dieperink and P.K.A. de Witt Huberts, Annu. Rev. Nucl. Part. Sci. **40**, 239 (1990).

[16] G. J. Kramer, H. P. Blok and L. Lapikás, *Nucl. Phys.* **A679**, (2001) 267.

[17] D. W. Devins, D. L. Friesel, W. P. Jones, A. C. Attard, I. D. Svalbe, V. C. Officer, R. S. Henderson, B. M. Spicer and G. G. Shute, Austral. J. Phys. **32**, 323 (1979).

[18] A. A. Cowley, J. V. Pilcher, J. J. Lawrie, and D. M. Whittal, Phys. Rev. C **40**, 1950 (1989).

[19] P. Kitching, C. A. Miller, D. A. Hutchen, W. J. McDonald and A. W. STETZ, Nucl. Phys. **A340**,423 (1980).

[20] W.J. McDonald, R. N. McDonald, W.C. Olsen, R. Dymarz, F. Khanna, L. Antonuk, J. M. Cameron, P. Kitching, G.C. Neilson, D.M. Sheppard, D.H. Hutcheon, C.A. Miller, and J. Kallne, Nucl. Phys. **A456**, 577 (1986).

[21] C. Samanta, N.S.Chant, P.G.Roos,A.Nadasen, J.Wesick nd A.A.Cowley, Phys. Rev. C **34**, 1610 (1986).

[22] A. A. Cowley, J. J. Lawrie, G. C. Hillhouse, D. M. Whittal, S. V. Förtsch, J. V. Pilcher, F. D. Smit, and P. G. Roos, Phys Rev. C **44**, 329 (1991).

[23] P. G. Roos, N. S. Chant, A.Nadasen, J.Wesick D. W. Devins, D. L. Friesel, W. P. Jones, A. C. Attard, R. S. Henderson, I. D. Svalbe, B. M. Spicer, V. C. Officer and G. G. Shute, Phys. Rev. Lett. **40**, 1439 (1978).

[24] L. Antonuk, P. Kitching, C. A. Miller, D. A. Hutchen, W. J. McDonald G.C. Neilson and W.C. Olsen, Nucl. Phys. **A370**, 389 (1981).

[25] P. Kitching, P.W. Green, C. A. Miller, D. A. Hutchen, A.N. James, W. J. McDonald, K. Michaelian, G.C. Neilson, W.C. Olsen, D.M. Sheppard, J. Soukup, and I. J. van Heerden, Proceedings: AIP Conf. Proc. **97**, 232 (1983).

[26] A. A. Cowley, G. J. .Arendes, J. A. Stander, W. A. Richter, Phys. Lett. **359B**, 300 (1995).

[27] R. Neveling, A. A. Cowley, G. F. Steyn, S. V. Förtsch, G. C. Hillhouse, J. Mano, and S. M. Wyngaardt, Phys. Rev. C **66**, 034602 (2002).

[28] Y. Kudo and K. Miyazaki, Phys. Rev. C **34**, 1192 (1986).

[29] N. Kanayama, Y. Kudo, H. Tsunoda and T. Wakasugi, Prog.Theor.Phys.(Kyoto) 83, 540 (1990).

[30] J. Mano and Y. Kudo, Prog.Theor.Phys.(Kyoto) 100, 91 (1998).

[31] G. Jacob, Th. A. J. Maris, C. Schneider and M. R. Teodoro, Phys. Let. **45B**, 181 (1973).

[32] P. Kitching, C. A. Miller, D. A. Hutchen, A. N. James, W. J. McDonald, J. M. Cameron, W.C. Olsen and G. Roy, Phys. Rev. Lett. **37**, 1600 (1976).

[33] C. A. Miller , Nucl. Phys. **A353**, 157c (1981).

[34] O. V. Maxwell and E. D. Cooper, Nucl. Phys. **A574**, 819 (1994).

[35] K. Hatanaka, M. Kawabata, N. Matsuoka, Y. Mizuno, S. Morinobu, M. Nakamura, T. Noro, A. Okihana, K. Sagara, K. Takahisa, H. Takeda, K. Tamura, M. Tanaka, S. Toyama, H. Yamazaki, and Y. Yuasa, Phys. Rev. Lett. **78**, 1014 (1997).

[36] T. Noro, T. Baba, K. Hatanaka, M. Ito, M. Kawabata, N. Matsuoka, Y. Mizuno, S. Morinobu, M. Nakamura, A. Okihana, K. Sagara, H. Sakaguchi, K. Takahisa, H. Takeda, A. Tamii, K. Tamura, M. Tanaka, S. Toyama, H. Yamazaki, Y. Yuasa, H. Yoshida, and M. Yosoi, Nucl. Phys. **A629**, 324c (1998).

[37] T. Noro, T. Yonemura, S. Asaji, N. S. Chant, K. Fujita, Y. Hagihara, K. Hatanaka, G. C. Hillhouse, T. Ishida, M. Itoh, S. Kishi, M. Nakamura, Y. Nagasue, H. Sakaguchi, Y. Sakemi, Y. Shimizu, H. Takeda, Y. Tamesige, S. Terashima, M. Uchida, T. Wakasa, Y. Yasuda, H.P. Yoshida, and M. Yosoi
Phys. Rev. C **72**, 014602–1-5 (2005).

[38] T. Noro, M. Kawabata, G. C. Hillhouse, S. Akimune, H. Akiyoshi, I. Daito, K. Hatanaka, M. Itoh, Y. Maeda, N. Matsuoka, S. Morinobu, M. Nakamura, A. Okihana, H. Sagara, H. Sakaguchi, K. Takahisa, H. Takeda, A. Tamii, K. Tamura, H. Toyokawa, H. Yamazaki, H.P. Yoshida, M. Yosoi
Phys. Rev. C **77**, 044604–1-9 (2008).

[39] A. Tamii, H. Akimune, I. Daito, Y. Fujita, M. Fujiwara, K. Hatanaka, K. Hosono, F. Ihara, T. Inomata, T. Ishikawa, M. Itoh, M. Kawabata, T. Kawabata, M. Nakamura, T. Noro, E. Obayashi, H. Sakaguchi, H. Takeda, T. Taki, H. Toyokawa, H. P. Yoshida, M. Yoshimura, M. Yosoi
Phys. Lett. **459B**, 61–66 (1999).;
A. Tamii,PhD thesis, Kyoto University, 1996.

[40] T. Kawabata, T. Ishikawa, M. Itoh, M. Nakamura, H. Sakaguchi, H. Takeda, T. Taki, M. Uchida, Y. Yasuda, M. Yosoi, H. Akimune, K. Yamasaki, G. P.A. Berg, H. Fujimura, K. Hara, K. Hatanaka, J. Kamiya, T. Noro, E. Obayashi, T. Wakasa, H.P. Yoshida, B. A. Brown, H. Fujita, Y. Fujita, Y. Shimbara, H. Ueno, M. Fujiwara, K. Hosono, A. Tamii, H. Toyokawa
Phys. Rev. C **65**, 064316–1-12 (2002);
T. Kawabata,PhD thesis, Kyoto University, 1996.

[41] M. Yosoi, H. Akimune, I. Daito, H. Ejiri, H. Fujimura, M. Fujiwara, T. Ishikawa, M. Itoh, T. Kawabata, M. Nakamura, T. Noro, E. Obayashi, H. Sakaguchi, H. Takeda, T. Taki, A. Tamii, H. Toyokawa, N. Tsukahara, M. Uchida, T. Yamada, H.P. Yoshida
Phys. Lett. **551B**, 255–261 (2003).

[42] M. Yosoi, H. Akimune, I. Daito, H. Ejiri, H. Fujimura, M. Fujiwara, K. Fushimi, K. Hara, K. Y. Hara, H. Hashimoto, T. Ishikawa, M. Itoh, Y. Itow, S. Kishi, T. Kawabata, K. Kawase, M. Kinoshita, K. Kobayashi, M. Nakamura, K. Nakanishi, Y. Nakatsugawa, S. Nakayama, T. Noro, E. Obayashi, S. Okumura, H. Sakaguchi, Y. Sakemi, M. Shiozawa, H. Takeda, T. Taki, A. Tamii, M. Tanaka, S. Terashima, H. Toyokawa, N. Tsukahara, M. Uchida, T. Yamada, T. Yamagata, Y. Yasuda,

H.P. Yoshida, R. G. T. Zegers, J. Zenihiro
Nucl. Phys. **A738**, 451–454 (2004).

[43] M. Kawabata, PhD thesis, University of Osaka, 1997.

[44] K. Hatanaka, K. Takahisa, H. Tamura, M. Sato, and I. Miura, Nucl. Instrum. Methods Phys. Res. A **384**, 575 (1997).

[45] I. Miura, T. Yamazaki, A. Shimizu, K. Hosono, T. Itahashi, T. Saito, A. Ando, K. Tamura, K. Hatanaka, M. Kibayashi, M. Uraki, H .Ogata, M. Kondo, and H. Ikegami, in *Proceedings of the 13th International Conference on Cyclotrons and their Applications, Vancouver, 1992*, edited by G. Dutte and M. K. Craddock (World Scientific, Singapore, 1993), p. 3

[46] M. Yosoi, private communications.

[47] M. Fujiwara, A. Nakanishi, Y. Fujita, N. Matsuoka, T. Noro, S. Morinobu, and H. Ikegami, RCNP annual report, 1989, p. 201.

[48] M. Fujiwara, H. Akimune, I. Daito, H. Fujimura, Y. Fujita, K. Hatanaka, H. Ikegami, I. Katayama, K. Nagayama, N. Matsuoka, S. Morinobu, T. Noro, M. Yoshimura, H. Sakaguchi, Y. Sakemi, A. Tamii, and M. Yosoi, Nucl. Instrum. Methods Phys. Res. A **422**, 484 (1999).

[49] N. Matsuoka, T. Noro, K. Sagara, S. Morinobu, A. Okihana, and K. Hatanaka, RCNP annual report, 1991, p. 186; 1990, p. 235.

[50] N. Matsuoka *et al.*, RCNP Annual Report 1992, p. 174.

[51] T. Noro, M. Fujiwara, O. Kamigaito, S. Hirata, Y. Fujita, A. Yamagoshi, T. Takahashi, H. Akimune, Y. Sakemi, M. Yosoi, H. Sakaguchi, and J. Tanaka, RCNP annual report, 1991, p. 177.

[52] A. Tamii, H. Sakaguchi, H. Takeda, M. Yosoi, H. Akimune, M. Fujiwara, H. Ogata, M. Tanaka, and H. Togawa, IEEE Trans. Nucl. Sci. **43**, 2488 (1996).

[53] A. Tamii, M. Itoh, T. Kawabata, H. Sakaguchi, H. Takeda, T. Taki, H. Torii, M. Yosoi, H. Akimune, T. Baba, M. Fujiwara, M. Kawabata, T. Noro, and H. Yoshida, in *Proceedings of the 2nd International Data Acquisition Workshop on Networked Data Acquisition System, Osaka, Japan, 1996*, edited by M. Nomachi and S. Ajimura (World Scientific, Singapore 1997), p. 238.

[54] T. Kawabata, H. Sakaguchi, A. Tamii, H. Takeda, T. Taki, and H. Yoshida, RCNP annual report, 1996, p. 161.

[55] G. Jacob and Th.A.J. Maris, Rev. Mod. Phys. **38**, 121 (1966).

[56] E. Obayashi, M.Sc. thesis, Osaka University, 1999 (unpublished).

[57] N.S. Chant and P.G. Roos, Phys. Rev. C **15**, 57 (1977).

[58] N.S. Chant and P.G. Roos, Phys. Rev. C **27**, 1060 (1983);
program code THREEDEE.

[59] Y. Ikebata, Phys. Rev. C **52**, 890 (1995).

[60] E.D. Cooper, S. Hama, B.C. Clark, and R.L. Mercer, Phys. Rev. C **47**, 297 (1993).

[61] C. J. Horowitz, D. P. Murdock, and B. D. Serot, *in Computational Nuclear Physics 1*, edited by K. Langanke, J. A. Maruhn, and S. E. Koonin (Springer-Verlag,Now York, 1993), p. 129.

[62] H. de Vries, C.W. de Jager, and C. de Vries, Atomic Data and Nuclear Data Tables. **36**, 495 (1987).

[63] C.J. Horowitz, D.P. Murdock, and B.D. Sero, in *Computational Nuclear Physics*, edited by K. Langanke, J.A. Marhun, and S.E. Koonin (Springer-Verlag, Berlin Heidelberg, 1991) Vol. 1, p. 129.

[64] R.A. Arndt, C.H. Oh, I.I. Strakovsky, R.L. Workman, and F. Dohrmann, Phys. Rev. C **56**, 3005 (1997); solution of SAID program (http://gwdac.phys.gwu.edu).

[65] F.Perey and B.Bunk, Nucl. Phys. **32**, 353 (1962).

[66] P. Doll, G. J. Wagner and K. T. Knöpfle, Nucl. Phys. **A263**, 210 (1976)

[67] Yu. P. Antoufiev *et al.*, Phys. Lett. **42B** 347 (1972)

[68] K. Nakamura *et al.*, Nucl. Phys. **A296** 431 (1978)

[69] G. J. Kramer et al., Phys. Lett. **B227** (1989) 199.

[70] G. van der Steenhoven, H.P. Blok, E. Jans, M. de Jong, L. Lapikás, E.N.M. Quint, and P.K.A. de Witt Huberts, Nucl. Phys. **A480** (1988) 547.

[71] J. Mougey, M. Bernheim, A. Bussière, A. Gillebert, Phuan Xuan Ho, M. Priou, D. Royer, I. Sick, and G.J. Wagner, Nucl. Phys. **A262**, 461 (1976).

[72] J. M. Udias, P. Sarriguren, E. Moya de Guerra, E. Garrido and J. A. Caballero, Phys. Rev. C **48**, 2731 (1993).

[73] V. Van der Sluys, K. Heyde, J. Ryckebusch and M. Waroquier, Phys. Rev. C **55**, 1982 (1997).

[74] K. I. Blomqvist, Z.Phys. **A351**, 353 (1995).

[75] L. Lapikás, G. van der Steenhoven, L. Frankfurt, M. Strikman and M. Zhalov, Phys. Rev. C **61**, 064325 (2000).

[76] J. B. J. M. Lenen *et al.*, Phys. Rev. Lett. **62** 2925 (1989)

[77] J. B. J. M. Lenen *et al.*, Phys. Rev. Lett. **63** 2793 (1989)

[78] R. G. Lovas, A. T. Kruppa and J. B. J. M. Lenen, Nucl. Phys. **A516** 325 (1990)

[79] S. Saito, J. Hiura and H. Tanaka, Prog.Theor.Phys.(Kyoto) 39, 635 (1968).

[80] T. Kobayashi, K. Ozeki, K. Watanabe, Y. Matsuda, Y. Seki, T. Shinohara, T. Miki, Y. Naoi, H. Otsu, S. Ishimoto, S. Suzuki, Y. Takahashi, E. Takada, Nucl. Phys. A **805**, 431c (2008).

List of Figures

List of Tables